T-4280

THE EFFECTS OF CHANGING MELT PARAMETERS ON ASPECTS OF SOLIDIFICATION STRUCTURE DURING EXPERIMENTAL ELECTROSLAG REMELTING

by

Steven L. Breitenbach

A thesis submitted to the Faculty and the Board of Trustees of the Colorado School of Mines in partial fulfillment of the requirements for degree of Master of Science (Metallurgical and Materials Engineering).

Golden, Colorado

Date 9/2/92

Signed: Steven L. Breitenbach

Steven L. Breitenbach

Approved: Glen Edwards

Dr. Glen Edwards
Thesis Advisor

Golden, Colorado

Date 9/2/92

J. Moore

Dr. John Moore
Professor and Head,
Department of
Metallurgical Enginnering

ABSTRACT

Aspects of solidification which include pool size and shape, local solidification time, and macrosegregation are important means by which to characterize the solidification process during melting. In electroslag remelting (ESR), the relationships between these parameters and process inputs is poorly understood. This study investigated the effect of melting current (3-7kA), slag cap thickness (75mm-150mm), and immersion depth (10mm-50mm) on aspects of solidification in Alloy 625. The study was conducted using 200mm diameter electrodes, a 250mm diameter mold, 60-20-20 slag, and a moving mold operation. Electrode to pool gap distance (cap thickness minus immersion depth) was the most significant indicator of pool size. Analysis was conducted on longitudinal sections that were removed from steady state sections of each ingot. Local solidification times were calculated at center, mid-radius, and edge positions. Process efficiency increased with input power and was relatively unaffected by the other inputs. The pool symmetry was relatively unchanged by increases in power. The ingot local solidification times were not directly effected by variations in the melting parameters.

TABLE OF CONTENTS

LIST OF FIGURES

LIST OF TABLES

ACKNOWLEDGMENTS

I would like to express my appreciation to the following organizations and people for their support during this study:

The Special Metals Processing Consortium and Dr. Frank Zanner for funding the my graduate program and allowing me to conduct the research at Sandia National Laboratory.

Dr. Glen Edwards for taking time to review and comment on the structure of the thesis.

Dr. Robert Frost for getting me started in the graduate program and offering technical guidance and advice.

Jim Heilman at Carpenter Technology for his technical advice and continued support.

Special thanks go to Dr. Brian Damkroger for being a good boss and a good friend throughout my graduate experience.

Finally, I would like to thank my fiancee, Tani, for her love and support and especially for her patience while I was completing this work.

1.0 INTRODUCTION

Electroslag remelting, ESR, is a process whereby metal or alloy is remelted through the resistance heating of a molten slag (a schematic drawing of the ESR process is depicted in Figure 1). The process is best utilized as a secondary or tertiary melting step. ESR processing may be preceded by an air melt process, or a VIM (Vacuum Induction Melting) process to produce the electrode needed for remelting. The air melt process includes an electric arc furnace melt followed by an AOD (Argon Oxygen Decarburization) process. Generally, tool steels and stainless steel used in oil industry components are melted using an Electric Arc/AOD/ESR melt sequence. The VIM/ESR melt sequence is used for alloys required for high temperature structural members, high temperature fasteners, chemical plant hardware, and gas turbine engine ducting. Finally, either the Arc/AOD/ESR or the VIM/ESR melt sequence may be followed with a vacuum arc remelting (VAR) step. This final processing step is required for nickel alloys used in high temperature rotating parts such as turbine disks for jet engines.

ESR processing is beneficial as a melting practice for

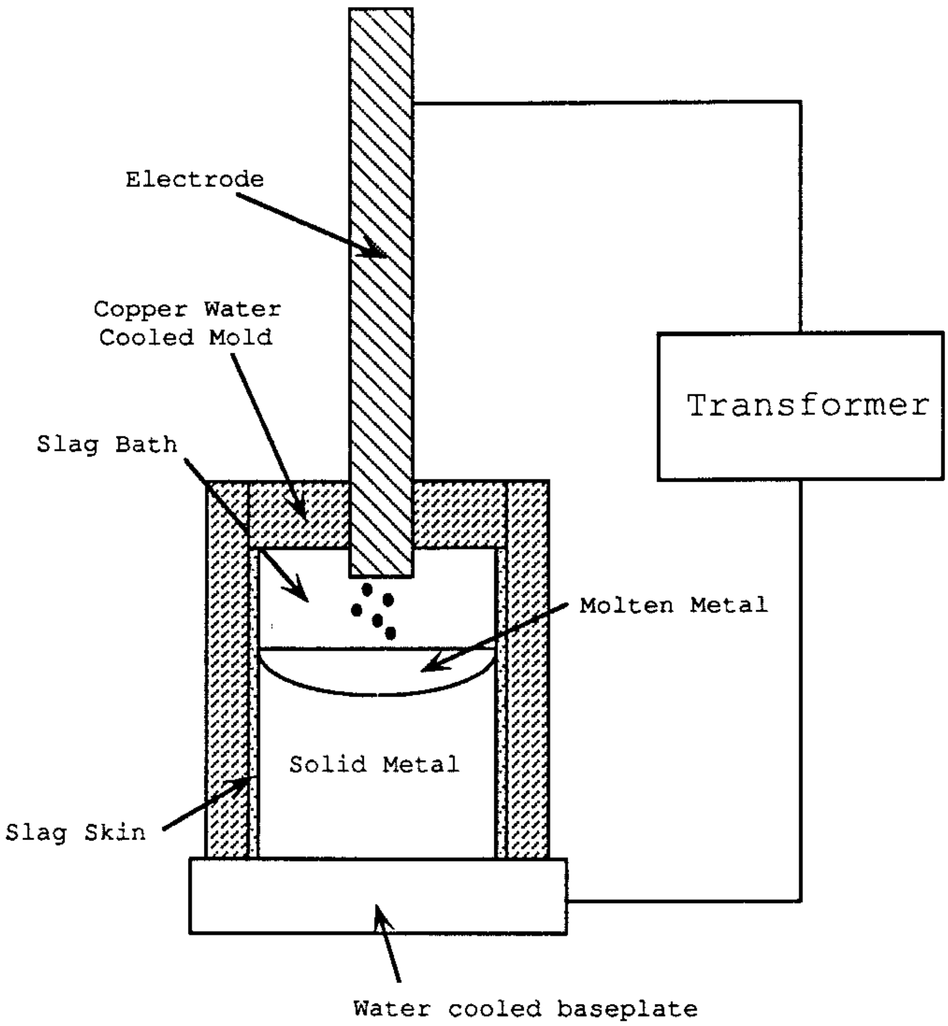

Figure 1. A Schematic Illustration of the ESR Process.

several reasons. The process has the ability to produce a sound ingot with the absence of centerline solidification defects such as piping and porosity[1] and the ability to reduce the amount of undesirable elements (i.e. sulfur and oxygen) through slag refining[1]. Sulphur removal may be chemical or electrolytic in nature (electrolytic reactions occur when the ESR furnace is operated in DC mode). Chemical removal of sulphur may occur at the gas-slag reaction site, $[S^{2-}] + 3/2\{O_2\} = \{SO_2\} + (O^{2-})$, or at the slag-metal reaction site, $[S] + (O^{2-}) = (S^{2-}) + [O]$[2]. In addition to the chemical removal of sulfur, key alloying elements like titanium and aluminum may be lost if elemental oxidation occurs in the slag: $(2x/y)M_{(s,l,g)} + O_{2(g)} = (2/y)M_xO_{y(s,l,g)}$, according to Hoyle[2]. Finally, electroslag remelting has the ability to produce an ingot with a more homogeneous chemical composition[1].

The purpose of the research was to characterize the solidification structures that were developed in a laboratory scale (254-mm-diam.) ESR ingot. The program involved varying specific melting parameters using a Yates 3 parameter, 2 level factorial experiment. This two-level design is considered useful for exploratory investigations where not very much is known about the process. This Yates factorial experiment[3] accomplishes two goals: 1) determination of the main effects of variables, and 2) determination of interaction effects between variables. An assumption that the ESR input parameters have interactive effects mandates the use of a Yates two level factorial experiment. The Yates experiment design was chosen because it provided a systematic means to evaluate the interactiveness of electroslag remelting parameters. The input parameters associated with an electroslag remelting process include current, voltage, slag cap thickness, immersion depth, and slag composition. For this experimentation the following ESR parameters were chosen: 1) melting current, 2) slag cap thickness during melting, and 3) immersion depth of the electrode in the slag. A schematic drawing of this factorially designed experiment is shown in Figure 2. In this experiment, the two level factorial design was altered to include a point that represented mid-range values of the parameters evaluated. Although, through the use of statistics the main effects and interactive effects of parameters can be determined with this factorially designed experiment, the data was not analyzed using statistics. Trends and parameter interaction were determined through direct analysis of the data.

For this experiment, the slag cap thickness and immersion depth were evaluated over a range that guaranteed

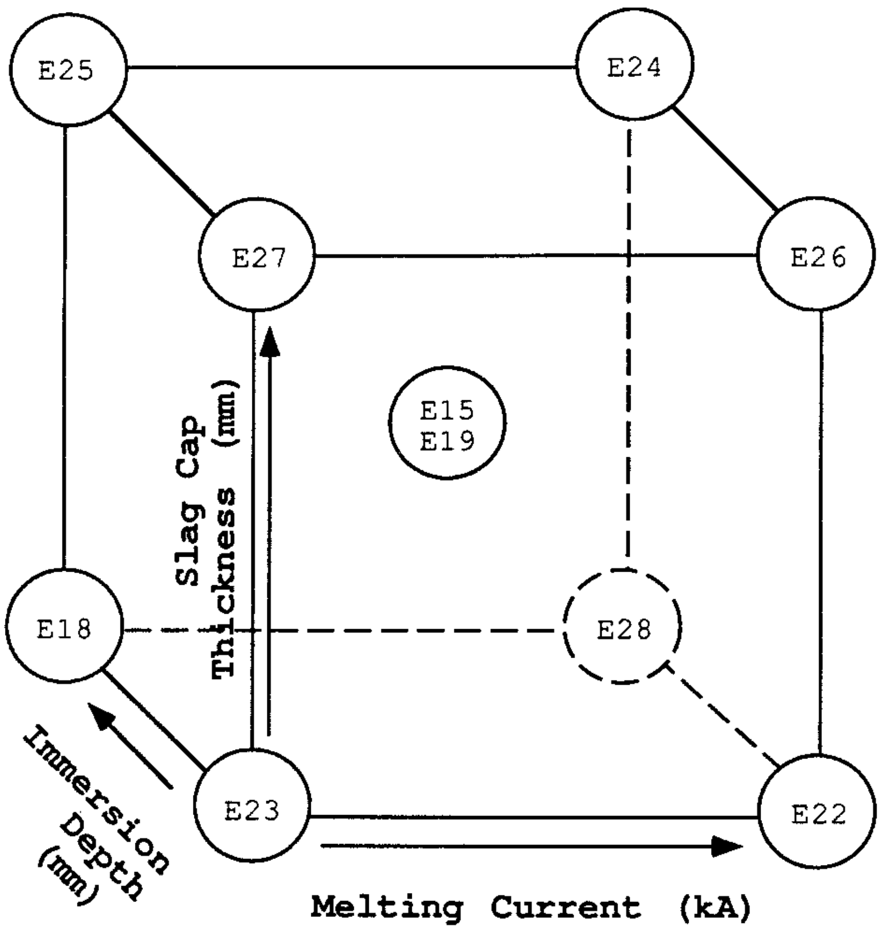

Figure 2. Schematic drawing of the Yates 2 level 3 parameter factorial experiment.

the experiment would run outside normal industrial electroslag remelting conditions. The range over which the current varied was determined by what the experimental furnace at Sandia could output. The Yates factorial experiment provides a means of generating data which can only be interpolated within the bounds set by the 3 parameter, 2 level cube. The data cannot be extrapolated.

The slag cap thickness is an important parameter during ESR processing. The amount of heat generated through the resistive heating of slag controls the melting of the electrode. The immersion depth of the electrode in the slag is governed by the voltage of the system. The furnace outputs a current, a value of voltage or voltage swing is dialed into the controller and the furnace finds the proper electrode depth in the slag which satisfies the voltage or voltage swing set point.

Simplistically, the relation between immersion depth and voltage can be explained if it is assumed that the slag acts as a pure resistor(1). Assuming a pure resistor, then the resistance of the slag is a function of the slag resistivity, the cross sectional area of the slag bath, and the length of slag between the electrode and pool. Therefore at constant current, decreasing the immersion depth will lengthen the resistor, increase the resistance value, and increase the voltage. Conversely, increasing the immersion will shorten the length of the resistor, decrease the resistance value and decrease the voltage.

The aspects of solidification structures characterized included molten pool shape (depth and volume measurements), dendrite arm spacing, and the extent of macrosegregation. In addition to solidification aspects, the slag skin thickness and surface quality of the ingot were evaluated.

The relationship between solidification structure and the level of each process parameter was evaluated and compared to existing data (where available). The relative importance of process variables and their operational level with respect to controlling the various aspects of solidification structure was evaluated.

2.0 LITERATURE REVIEW

2.1 BACKGROUND ON ALLOY 625

Alloy 625 is a nickel-iron based superalloy. The nominal composition of Alloy 625[4] is given in Table I along with the composition of the material used in this study. Unlike most nickel-based superalloys, Alloy 625 is solid solution strengthened by adding niobium and molybdenum rather than precipitation hardened with the formation of either gamma prime [$Ni_3(Al,Ti)$] or gamma double prime [$Ni_3(Nb)$] phases.

The precipitation of gamma prime in Alloy 625 is precluded by the alloys low aluminum and titanium contents (0.2 wt pct. Ti and 0.2 wt pct. Al nominally). For gamma prime precipitation (Ni_3Al) from aluminum, an aluminum content between 1.5 and 8 wt pct. is required[5].

The precipitation of gamma double prime (Ni_3Nb) in Alloy 625 is precluded by a combination of the alloys low niobium and low iron contents (3.6 wt pct. Nb, 2.5 wt pct. Fe nominally). Quist and Taggert[6] showed that gamma double prime will not form in binary nickel-niobium with as high as 12 at pct. niobium unless some iron is present.

Alloy 625 does not form a large number of secondary

Table I

Nominal composition (in wt pct.) of alloy 625[4] along with the three heats used in the experiment.

625	C	Mn	Fe	S	Si	Ni	Cr	Al	Ti	Mo	P	Cb+Ta
Heat (1)	0.03	0.12	4.27	.001	0.13	60.31	21.6	0.36	0.20	9.52	0.08	3.46
Heat (2)	0.03	0.11	4.18	.001	0.09	60.95	21.8	0.26	0.26	9.02	.005	3.41
Heat (3)	0.04	0.06	4.03	.001	.11	61.1	21.6	.030	0.27	8.99	.006	3.48
Nom. max.	0.1	.25	5.0	.005	.50	Bal.	23	0.40	0.40	10.0	.015	4.15

phases during solidification; hence, characterizing the secondary phases becomes a relatively simple task. Alloy 625 has the ability to form the following secondary phases in its primary gamma matrix: MC(NbC) carbide and Laves phase[7]. The time temperature transformation (TTT) diagram for Alloy 625[8] (shown in Figure 3) indicates that other carbides may form but only at cooling rates much slower than what is typically experienced during ESR processing.

Work performed by Cieslak[7] indicated that the solidification process of Alloy 625 is dependent upon the amount of carbon and silicon present in the alloy. Cieslak studied eight different Alloy 625 compositions (Table II), all within the required specification. The first four had low niobium contents (~0.01wt%). These alloys solidified as single phase gamma. The last four alloys had high niobium (~3.6wt%) contents, which resulted in the precipitation of one or more secondary phases during solidification. The levels of minor elements carbon and silicon were varied in the high niobium alloys: 1)high silicon (~0.4wt pct.), high carbon (~0.037wt pct.); 2)high silicon, low carbon (~0.001wt pct.); 3)high carbon, low silicon (~0.01wt pct.); and 4)low silicon, low carbon. By comparing the phases present in the four specified alloy compositions and examining the differential thermal analysis results, Cieslak concluded

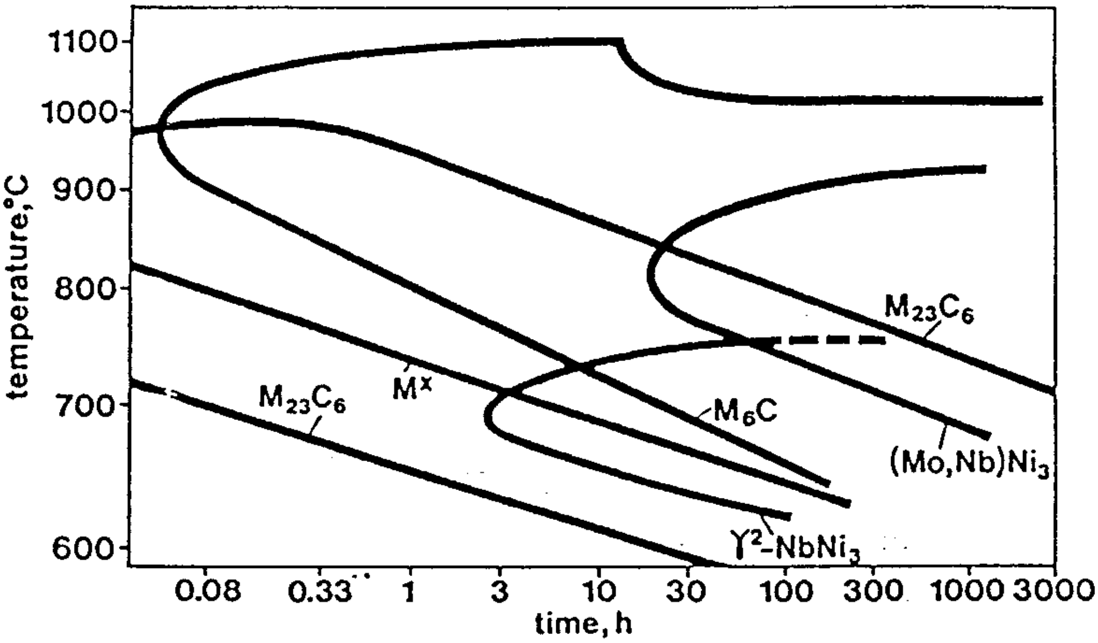

Figure 3. The TTT diagram for Alloy 625[8].

Table II

The compositions (in wt pct.) of alloy 625 evaluated by Cieslak[7].

Element	1	2	3	4	5	6	7	8
C	0.006	0.031	0.006	0.036	0.009	0.038	0.008	0.035
Mn	0.02	0.02	0.02	0.03	0.03	0.03	0.03	0.03
P	0.005	0.005	0.005	0.005	0.006	0.006	0.006	0.006
S	0.002	0.002	0.002	0.003	0.003	0.003	0.004	0.003
Si	0.03	0.03	0.35	0.39	0.03	0.03	0.38	0.46
Cr	22.10	21.95	21.63	21.57	21.81	21.83	21.65	21.68
Mo	9.54	9.61	9.6	9.63	9.81	9.81	9.68	9.67
Ti	0.06	0.06	0.06	0.06	0.06	0.06	0.06	0.06
Nb	0.01	0.01	0.02	0.02	3.61	3.6	3.57	3.53
Fe	2.56	2.55	2.18	2.59	2.3	2.31	2.26	2.29
Ni	bal.	bal.	bal.	bal.	bal.	bal.	bal.	bal.

that silicon promoted the formation of either single phase Laves or eutectic Laves phase. These conclusions were supported by Wlodek[9]. Cieslak also concluded that carbon retarded the formation of Laves phase by tying up the carbide-forming elements (niobium for example).

The Alloy 625 used in this investigation contained approximately 0.09wt pct. silicon and 0.03wt pct. carbon (Table I). Comparison of this composition with those of Cieslak, shows that the material used here was close to the high carbon (0.037)-low silicon (0.01) alloy. It was expected that since the cooling rate of the ESR ingots was not the same as the cooling rate during the DTA experiments, the same solidification structure would not be observed.

2.2 POOL PROFILE

The molten pool profile is an important parameter with respect to final ingot structure. A high melt rate, which will form a deep metal pool, is more beneficial from an economic standpoint. From a metallurgical standpoint, a low melt rate and a shallow metal pool is more beneficial[1]. The degree of dendrite structure variation from center to edge decreases when the pool profile is flatter. With a shallow pool profile the associated vertical freezing results in more uniform dendrite arm spacing from the center to the edge of the ingot. The more uniform spacing would result in less variation in microsegregation between the center and edge of the ingot[1].

2.2.1 Comparison with Parameters

Medovar[10] predicted how the following ESR melting parameters would affect pool depth and pool volume: electrode to pool gap, voltage, and slag bath depth.

Medovar assumed that the voltage, composition of slag, electrode cross section, and slag cap thickness were constant; and postulated that increasing the rate of delivery of the electrode decreased the length of the electrode/ingot gap, and resulted in a deeper pool depth and larger pool volume. He explained this phenomena by thinking about how decreasing gap distance would affect current and resistance. Medovar felt that decreasing the gap distance would cause the electrical resistance between the ingot and electrode to decrease. This reduction in resistance would cause an increase in current, so as to maintain a constant voltage. The combination of increased current and the movement of the heating source downward as the rate of delivery of the electrode was increased, would cause the volume and depth of the molten pool to increase.

In changing the voltage of the system while keeping the electrode rate of delivery constant, Medovar[10] felt that an increase in voltage would lead to a decrease in pool depth while the pool volume remained constant. An increase in voltage would correspond to an increase in the gap between the electrode and ingot. Increasing the gap would expand the zone of heat evolution to the water-cooled copper crucible, and move the heat source upward and away from the molten metal pool, thereby creating a shallower pool profile.

Finally, Medovar[10] predicted that increasing the slag bath depth at constant values of gap distance, voltage, and current would result in a decrease in pool depth. He hypothesized that increasing the slag bath depth caused an increase in the immersion depth of the electrode in the slag. Increased immersion (although the gap had not changed) caused the heating source to reside deeper in the slag. The greater the depth of the slag bath, the more heat was consumed in maintaining the slag in a fused and superheated state. Thus, less heat remained for maintaining the metal in a molten state, and the pool depth decreased.

2.2.2 Thermal Modelling

Several investigations[11,12,13] have dealt with the prediction of pool profiles via thermal modelling. One of the key aspects of modelling the consumable electrode processes is the description of the boundary conditions at the top, bottom, side, and middle of the solidifying ingot. For example, one model expressed the top boundary as a time independent temperature distribution[11]. The side boundary condition incorporates what factors need to be accounted for in determining the heat transfer coefficient. For example, the side heat transfer coefficient of one model included the thermal conductivity of the mold, the slag skin, the air gap, and the water that cools the mold[12]. To a large extent, the validity of the boundary conditions determines the accuracy of the resulting model.

Three studies that specifically addressed the modelling of cylindrical ESR ingots were developed by Ballantyne and Mitchell[11], Carvajal and Geiger[12], and Paton[13]. All three models predicted both the liquidus and solidus profiles.

2.2.3 Characterization of Models

Mitchell and Ballantyne[11] developed a thermal model using finite difference equations. The inputs of the model include the material thermophysical properties, radius of the ingot, heat transfer coefficients (side and base), production of ingot rise velocity, and the height of ingot.

Boundary conditions were specified at the top, bottom, centerline, and side of the ingot. The top boundary was expressed as a time independent temperature distribution. The side boundary was derived by calculating a heat transfer coefficient that encompassed all factors on the side of system (i.e. mold, cooling water, slag skin, and air gap). It also assumed that conduction and radiation were the primary mechanisms that contributed to the heat transfer at the side of the ingot. The formation of the air gap between the ingot and mold, acted as the primary resistance to heat transfer at the side of the solidifying ingot. The bottom boundary was expressed as a heat transfer coefficient and a surrounding temperature. At the centerline of the ingot, it was assumed that no heat transfer took place across this boundary. Finally, at the solid/liquid interface, the release of latent heat was described by artificially increasing the specific heat within the liquidus/solidus temperature range. The model assumed axial symmetry during solidification.

The model quantifies the liquidus temperature as a function of the distance from the centerline of the ingot and calculated results of the model favorably compared with pool profiles developed in industrial ingots. The model also accurately determined the effects of varying ingot diameters and varying melt rates on the pool profiles.

General trends predicted by the model include: 1) molten pool depth linearly increases as the ingot diameter increases, 2) pool depth linearly increases with increasing melt rate, and 3) a quasi steady state pool depth is achieved when the ingot height increases to approximately 1-1.5 ingot diameters from the bottom of the ingot.

Carvajal and Geiger[12] developed a thermal model using a finite difference solution method. The model requires the following inputs: the thermophysical properties of the alloy, diameter of the ingot, thermal conductivity of the mold, thermal conductivity of the slag skin, thermal conductivity of the air gap, air gap thickness, mold thickness, and initial length of the ingot.

The side boundary condition was a statement of Fouriers Law for heat conduction (utilizing the temperature of the cooling water) in the radial direction. The bottom boundary condition was the same as the side, except that, Fouriers Law was referenced in the axial direction. They assumed for the top boundary condition that a parabolic temperature distribution, for heat generated uniformly inside a cylinder could be applied.

Output of the model included a solidus and liquidus profile. The output from the model was not compared with any actual data from industrial ingots. From their model, they concluded that quasi steady state melting was achieved one ingot diameter from the bottom.

Paton[13] developed a model using the divided step method of solving multidimensional problems. The inputs of the model included: radius of the ingot, thermophysical properties of the material, and the slag skin thickness. The model determines such solidification characteristics of the metal as the advance rate of the solidification front and the temperature gradient ahead of the solidification front. The model also predicts the formation of columnar or equiaxed ingot structure. The models predicted pool profiles compared well with experimental data from 18 ton electroslag remelted ingots.

The thermal models presented differ in the assumptions made regarding heat transfer across the air gap. It has been determined that variations in heat transfer affect both pool shape and size, therefore the formation of an air gap and the degree at which it affects the transfer of heat is an important consideration. The air gap forms as the cooling metal contracts away from the mold wall. Ballantyne and Mitchell proposed that both radiation and conduction were the primary mechanisms of heat transfer at the side boundary. They also determined that the air gap acted as the primary resistance to heat transfer at the side of the ingot. Carvajal and Geiger insisted that radiation and convection across the air gap was negligible and that heat was transferred by conduction only. Paton, on the otherhand, did not take the air gap into account.

All models indicated a point where quasi-steady state was achieved. None of the models predicted points, where quasi-steady state was achieved, were compared with industrial ingots to specifically determine where quasi-steady state melting started. Industry approximates quasi steady state melting begins after 2 ingot diameters of metal is melted.

The purpose of characterizing pool profiles was to determine which parameters (melting current, immersion depth, or slag cap thickness) significantly affected pool profiles. The experimental ingots were melted under the assumption that 1 to 2 ingot diameters of material must be melted before achieving steady state. This condition represented both industry opinion and experimental observation.

2.3 DENDRITE SPACING AND LOCAL SOLIDIFICATION TIME

In the literature, primary and secondary dendrite arm spacings have been correlated directly to the temperature distribution present in a cylindrical ingot. Mellberg[14], Holzgruber[15], Kroneis[16], and Eckstein[17] all compared electroslag remelted ingot dendrite arm spacings with the spacings in directionally solidified laboratory ingots for the purpose of characterizing ingot temperature gradients. Comparison with directionally solidified ingots is one approach towards correlating dendrite arm spacing with an ingot thermal regime.

A similar approach was taken by Ballantyne[18], except he computed local solidification times for an ingot, based on his model[11], and predicted the dendrite arm spacing by comparing the computed LST values with published solidification structure data. He concluded that the predicted structure compared favorably with the structure observed in Udimet-700.

Mitchell and Ballantyne extended the work of Ballantyne on U-700 to a study of ESR processed M2 steel and Alloy 718[19]. In this study, Mitchell and Ballantyne first compared their computed LST values and predicted structures with the LST values measured from dendrite arm spacings and computed in the literature[20,14]. The relationship established by Mitchell and Ballantyne between LST and DAS for M2 steel was the same as the relationship established by Barkalow[20] and Mellberg[14].

Mitchell and Ballantyne[19] also analyzed the effect of

LST on the precipitation of secondary phases during the solidification of M2 steel and Alloy 718. They found that LST had a marked effect on the second phase precipitation during ESR processing of M2 steel and Alloy 718. MC and M_2C carbides formed near the edge of the M2 steel ingot, a region associated with low LST values. Toward the center of the ingot, where the LST values were higher, M_6C carbides began to precipitate. A minimum LST value was established below which the formation of M_6C would not occur. In Alloy 718, LST was found to affect the formation of Laves phase, with the amount of Laves phase formed decreasing as LST decreased. Although a minimum LST value below which the formation of Laves could be avoided was not determined, a LST value was found below which the Laves formation would be minimized.

In another study, Mitchell and Ballantyne[21] attempted to define a LST/DAS/melt rate relationship for Alloy 718. They compared trends established in laboratory directional solidification experiments with observations made on industrial scale ingots. The work established that, for laboratory ingots, regular relationships existed between LST and the following microstructural characteristics: dendrite arm spacing, carbide distribution, and carbide size. In comparing the laboratory scale with industrial scale, it was determined that only the measured carbide size was accurate in predicting the solidification conditions and the LST values of the industrial ingot.

The model developed by Mitchell and Ballantyne[11] for predicting thermal profiles and local solidification times, as discussed earlier, was used to correlate melt rates to cooling rates for consumable electrode remelting practices. For vacuum arc remelted (VAR) ingots, their model predicted an increase in cooling rate with increasing melt rate as shown in Figure 4. The increased cooling rate would subsequently cause the formation of a finer secondary dendrite arm spacing. In general a decreased melt rate is associated with a decrease in current, therefore the data from Mitchell and Ballantyne indicated that decreasing current resulted in decreased cooling rate. This phenomena of decreasing melting current resulting in a coarsening of the ingot structure was also noticed by Shved[22].

It is accepted that the dendrite arm spacing varies with local solidification time or inversely with cooling rate[23-25]. For directional solidification experiments using static castings, the thermal gradient and the rate of advance of the solidification front are tied closely together[11]. Therefore in static castings, a low thermal gradient implies a low advance rate of the solidification

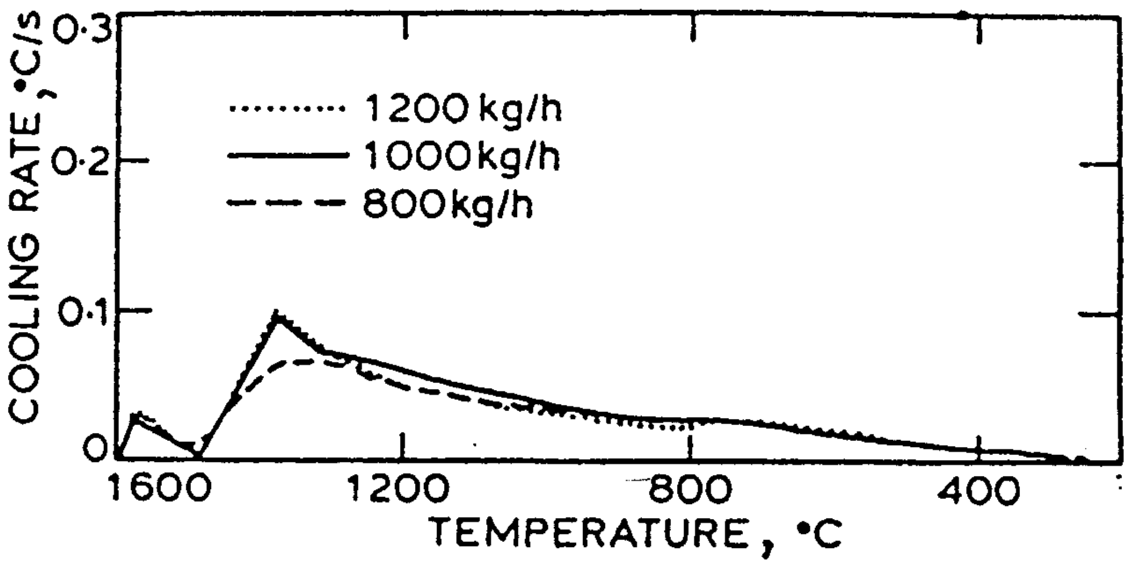

Figure 4. The relation between melt rate and cooling rate, as predicted by the model developed by Mitchell and Ballantyne[11].

front and a low cooling rate[26]. This phenomena does not apply to the consumable electrode remelting processes[22]. Mitchell and Ballantyne indicated that consumable remelting processes permit a degree of independent control over the two factors, solidification front advance rate and thermal gradient. Both factors can control the cooling rate hence, a slow advance rate of the solidification front does not necessarily imply a low thermal gradient and vice versa.

2.4 MACROSEGREGATION

Macrosegregation is an important parameter in characterizing the chemical homogeneity of a solidified ingot. Ingot macrosegregation develops in the form of channel segregates, segregation along the centerline of the ingot, and segregation to the edge of an ingot[27].

The study by Cieslak [7] determined that niobium and molybdenum exhibited the greatest tendency to segregate to the interdendritic regions. The solute in the liquid-solid zone would then be able to settle due to density driven flow of the interdendritic liquid[27].

The effect of process parameters on macrosegregation in electroslag remelted Alloy 718 was studied by Evans and Kruzynski[28]. They varied, with the goal of minimizing or eliminating centerline segregation, the following melt parameters: melt rate, slag chemistry, slag volume, and electrode immersion depth. All ingots were examined in the as-forged condition. They studied eight ingots with a common designated billet conversion practice: homogenization at 2150 degrees for 48 to 60 hours and press-forged to a 216-mm-diam. billet using a straight draw fine grain practice. Half of a ninth ingot was converted to billet using the same practice employed to convert the previous eight ingots. The other half of the ninth ingot was converted to billet by a "double upset" "double homogenization" practice where the ingot was homogenized, upset and drawn back, rehomogenized, upset again, and finally drawn to final hot size.

Their results indicated that varying degrees of macrosegregation occurred in all experimental melts that utilized the constant billet conversion practice. Evans and Kruzynski found that the degree of center segregation was more significant during the higher melt rates (~0.061-kg/sec) than the lower melt rates (~0.055-kg/sec). The best segregation results were obtained in the ingots that had low melt rates, good surface quality and a 152-mm slag cap. No center segregation was found in the ingot converted to billet by the "double upset" "double homogenization" practice.

Flemings[28] considered the effect of heat flow and macroscopic mass flow (in the form of diffusion, liquid convection and the flow of equiaxed structure suspended in a partially solidified liquid) on various types of macro-segregation in large static mold ingots. Accordingly he concluded that heat flow can affect segregation. During industrial melting, Flemings observed the phenomena of metal freezing off on a hot top prior to solidification of the ingot itself. When the hot top cools at a faster rate than the ingot, a negative temperature gradient develops. Flemings contended that the development of a negative temperature gradient is a plausible explanation for the presence of segregation near the top of a solidifying ingot.

With respect to the effect of mass flow on segregation, Flemings[28] presented a solidification model which assumed an ideal columnar solidification structure (where the dendrites stay intact - no movement of solid) to explain segregation in large ingots. He determined that since solute enrichment occurs behind the dendrite tips instead of in front; macrosegregation can result from the sweeping of solute from behind the dendrite tips. This sweeping will occur provided the liquid motion due to convection is vigorous enough to penetrate into the liquid solid zone. Another type of mass flow, which affects macrosegregation as indicated by Flemings, can occur when equiaxed grain solidification is prevalent. The equiaxed grains in the warmer part of the liquid solid zone can settle. This settling, or density driven movement of equiaxed crystals, can result in solute movement to the bottom of the molten pool.

Kou, Pourier, and Flemings[29] described how the concavity of a pool profile can affect macrosegregation. They devised a computer model for predicting macrosegregation in rotated electroslag or vacuum arc remelted ingots. The model simulates rotation of the ingot itself during solidification. Figure 5 compares the model's predicted mushy zone geometry (liquidus isotherm and solidus isotherm) for a static ingot with the liquid-solid zone geometry associated with hypothetical ingots rotated at 45 rpm, and 76 rpm. The results indicated the ingot rotated at 76 rpm experienced the least amount of macrosegregation. These macrosegregation results compared favorably with macrosegregation data obtained from several experimental melts. At low solidification rates (10^{-2} mm/s) and high local solidification time, applied rotation was found to decrease macrosegregation. Overall the results showed that rotation of the ingot during solidification resulted in an alteration of the pool profile, and density-driven

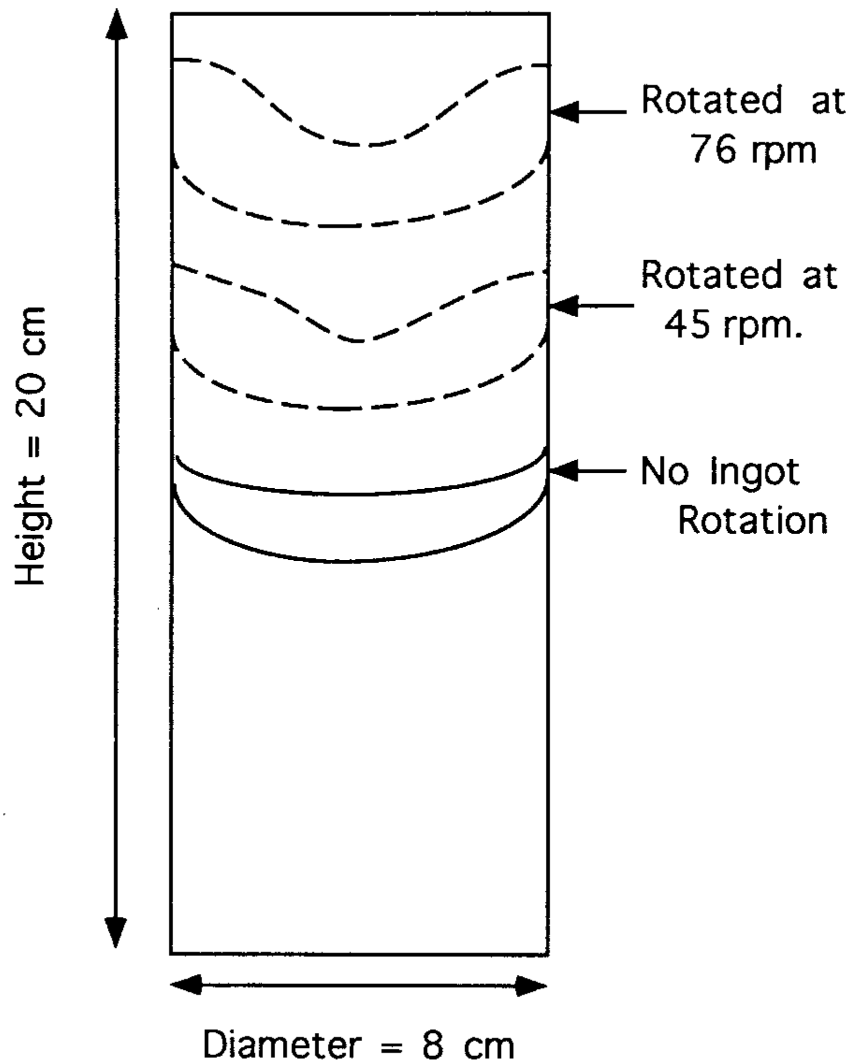

Figure 5. The pool profile variation observed by Kou and Flemings[29] during melting in which the ingot was rotated a different speeds.

segregation was reduced.

The study by Evans and Kruzynski[28] varied melt rate a maximum of 14pct., and slag volume a maximum of 50pct. (The extent of variation in immersion depth was not specified). The present investigation varied the melt rate by 500 pct., the slag cap thickness by 100 pct., and the immersion depth by 600 pct. Macrosegregation analysis of the melts in this study were performed directly on the ESR material.

2.5 INCLUSIONS

One of the reasons ESR processing is utilized extends from its ability to reduce the non-metallic inclusion content of the ingot. In general, ESR has three potential sources from which oxide inclusions form in the ingot: electrode inclusions, oxygen and deoxidant in solution in the electrode, and slag metal reactions inherent to the system. Several theories exist concerning the mechanism by which inclusions enter or form during ESR processing.

The inclusion mechanism was studied by Kay and Pomfret[30] in experiments wherein silicon and aluminum deoxidized iron electrodes were rapidly withdrawn from the slag. Their results showed a significant decrease in inclusion size with increasing proximity to the electrode tip, suggesting that inclusion dissolution was taking place at the electrode tip. The dissolution of inclusions was then followed by the transfer of oxygen and deoxidant to the slag and reprecipitation of the solute material during solidification.

Mitchell[31] performed mechanistic inclusion experiments with oxygen-containing iron or a composite of iron-OFHC copper electrodes. The data showed that 2-μm inclusions were maintained in the thin (~50-μm) liquid metal layer at the end of the electrode. In addition, large inclusions (4-6 microns) were concentrated at the surface of the electrode. Mitchell supports that the large inclusions at the surface were the result of some type of physical washing process, the actual mechanism was not specified. The inclusion distribution present in the electrode tip region indicated that some inclusion solution was occurring but the extent was considered negligible compared with the concentration of large inclusions that moved to the edge. The work by Mitchell concluded that almost all inclusions present in the final ingot were nucleated and grown in the liquid-solid zone.

Alloy 718 typically contains five types of inclusions present: Al_2O_3, TiN, MgO, MnS, and some carbonitrides. The chemistry of Alloy 625 will not allow the precipitation of Al_2O_3 or MgO due to the lack of aluminum and magnesium in the electrode unless the inclusion comes from the alumina bearing slag.

No work has been done to date characterizing the inclusion formation in Alloy 625. However, comparison with Alloy 718 suggests the formation of TiN, MnS, and possibly Al_2O_3.

2.6 LIQUID METAL FLOW IN THE INGOT POOL

Variation in motion of the liquid pool can cause variations in the final ingot. According to Mitchell and Ballantyne[32], liquid metal flow in the ingot pool can have two effects on the liquid/solid region. First, convective motion affects local segregation, and second, metal movement affects the local thermal fields. Both affects will cause microstructural and macrostructural changes characteristic of the momentum field in the ingot. The structural modifications from metal movement during electroslag remelting are much more complex and less well defined than that which occurs during vacuum arc remelting (VAR).

It has been accepted that motion in the liquid pool can result from two different phenomena. Motion can result from convective heat flow or flow caused by thermal gradients in the liquid pool, and from electromagnetic forces which result from the passage of current through the molten pool during DC mode electroslag remelting and vacuum arc remelting[32].

Work by Hoyle[33] involved a base plate oscillating in two directions at right angles. The operation was performed to bring all portions of the slag bath under the stationary electrode in sequence. It was found that the increased amount of liquid and slag movement provided a cooler bath and flatter pool profile (smaller temperature gradient from the mold to the center of the ingot). Hoyle found vertical rather than radial freezing took place in long electrodes with smaller cross sections. The vertical freezing in conjunction with increased liquid metal motion decreased the amount of macrosegregation.

Mitchell, Jackson, and Ballantyne[32] correlated the potential effects of liquid movement on macrosegregation for a small ESR furnace. They determined that the controlling feature in the macrosegregation behavior was the structure of the interface; whether it was cellular, plane front, or dendritic. In their case they assumed plane front solidification hence, there were no evidence of composition gradients and no solute was able to build up ahead of the solidification front. From this observation, they concluded there was no intrinsic reason for longitudinal segregation in electroslag remelted ingots, since the liquid is constantly able to sweep any accumulated solute. However since the solidification interface during these experimental melts was not plane front but dendritic, it is uncertain to what extent liquid movement affected segregation.

The present study qualitatively noted the variation in movements of the molten pool. No mechanical movement of the base plate, electrode, or mold occurred other than the movement that resulted from normal operation of a collar mold process.

2.6 SLAG SKIN

Mitchell and Etienne[34] researched the effect of slag skin on the surface quality of an ESR ingot. They determined that good surface quality is achieved at high power input when a finite depth of molten metal is in contact with the slag skin, which causes partial dissolution of the slag skin. Figure 6 presents a schematic representation of how the slag skin is affected by the molten metal/slag skin interface. They determined that at low power input, circulating liquid metal had insufficient thermal capacity to partially remelt the solid slag skin forming on the wall of the crucible. The inability to remelt the slag skin resulted in a lapped ingot surface with portions of slag skin becoming embedded in the solidified

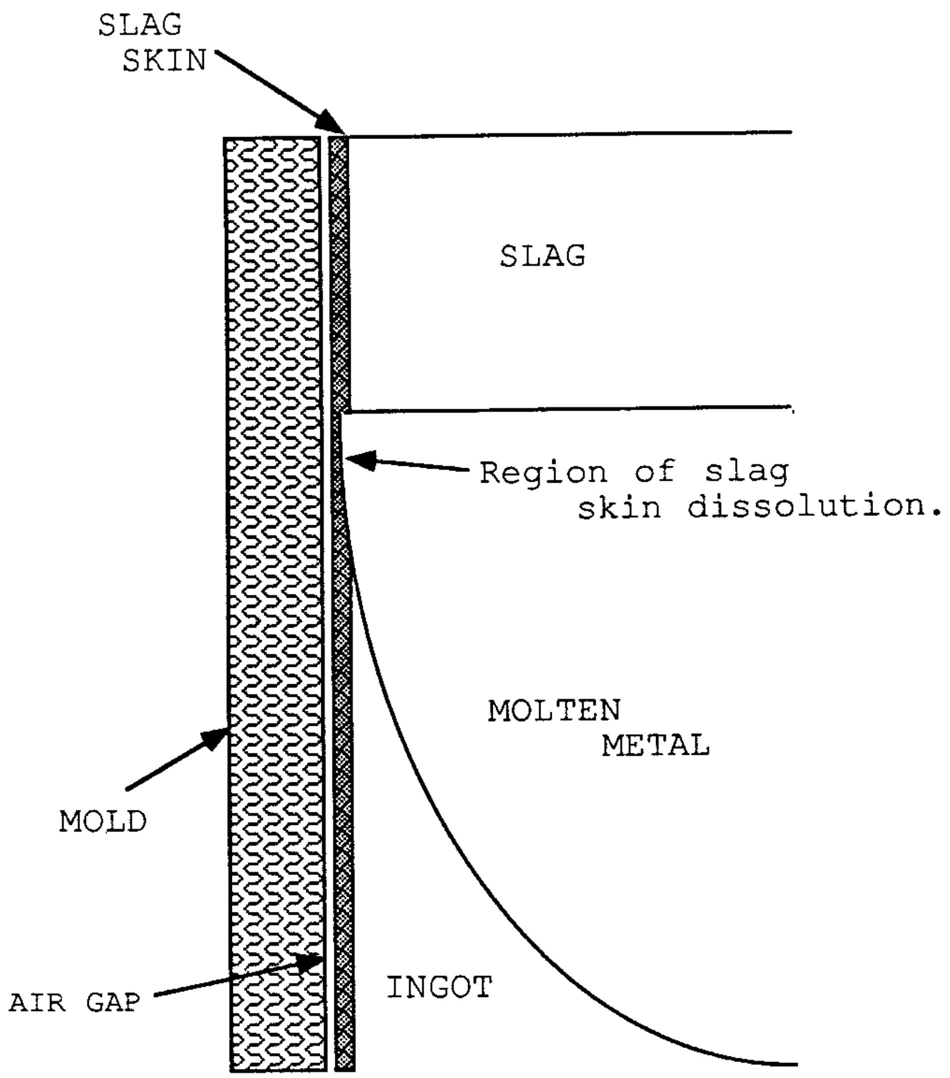

Figure 6. The condition at the slag/metal interface which dictates the formation and quality of the slag skin.

ingot. These defects resulted in poor ingot surface quality.

Further studies by Mitchell and Bell[35] discussed the effect of the Al_2O_3 content in the slag on the surface quality of an ESR ingot. As noted previously, Mitchell and Etienne[34] determined that good surface quality was attained when a finite depth of liquid metal was in contact with a slag skin. This condition is obtained when the slag skin has a melting point higher than that of the metal. Ideally the slag should have a liquidus temperature at least 100°C above that of the metal. Mitchell and Bell showed that this condition is achieved for pure iron electrodes when the weight percent Al_2O_3 in the slag exceeds the eutectic weight percent of Al_2O_3 as designated by the Al_2O_3-CaF_2 binary phase diagram (shown in Figure 7). The Al_2O_3 addition provides a slag composition with a higher melting point and a higher resistivity than the metal, so that enough heat is generated to sustain the condition of liquid metal against slag skin.

The slag skin thickness was qualitatively evaluated over the coarse of this experiment. During the scope of the experimentation, the effects of melt current, running slag depth, and immersion depth of the electrode on the slag skin thickness were determined.

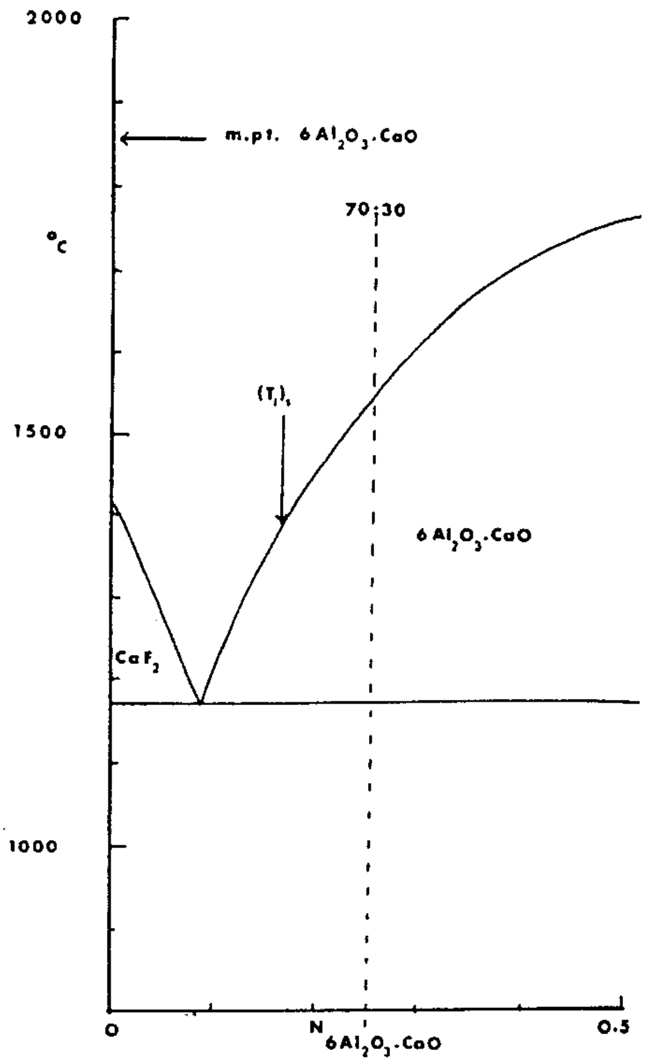

Figure 7. The Al_2O_3-CaF_2 Binary Phase diagram

3.0 EXPERIMENTAL PROCEDURE

3.1 FURNACE

The experimental melting used the Leybold-Heraeus Hanau F250/1G withdrawal mold ESR furnace at Sandia National Laboratories. A schematic of the withdrawal mold process is shown in Figure 8. These experiments used a 254-mm-diam. by 508-mm-long crucible. The furnace may be operated in either AC or DC mode, with the AC mode used throughout the experiment. Similarly, the mold may be either insulated or at ground potential. The mold was grounded for these experiments. In this mode, the current follows a path through the electrode and into the slag, and returns either through the ingot and base plate, or through the mold. The furnace was run in constant current mode, with voltage used as the control parameter for electrode location. Immersion checks were conducted by withdrawing the electrode from the slag (during the melt) and examining the voltage trace to determine the point where the electrode broke the slag surface. This trace was then compared to the (simultaneously digitized) electrode position trace to determine the electrode movement associated with electrode withdrawal. This value was then compared with the value

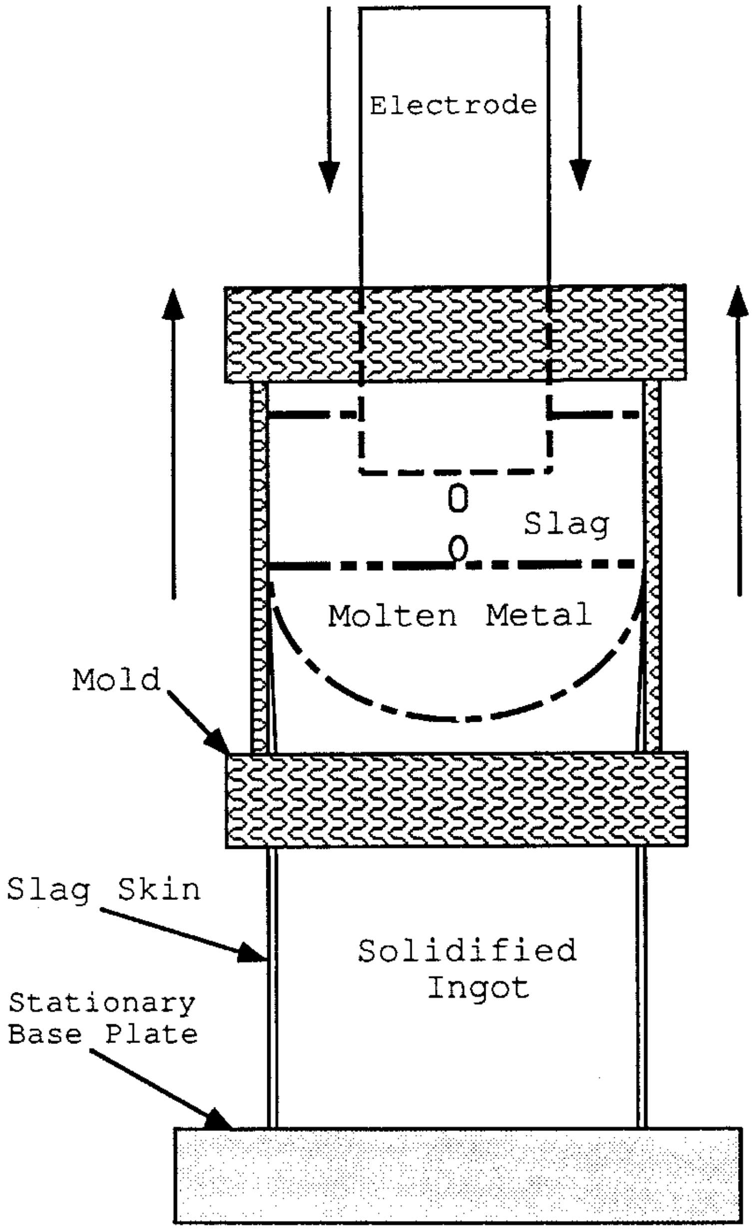

Figure 8. Schematic of withdrawal mold operation.

associated with the immersed electrode. The immersion check process is shown schematically in Figure 9; an example of a voltage and position plot is shown in Figure 10. All digitization was done using a MacIntosh Computer, National Instruments NB-A2000 data acquisition board, and an SMPC proprietary program package based on National Instruments LabView™ software.

3.2 STARTING MATERIAL

The material used for the experiments was Alloy 625. The electrode material was supplied by INCO Alloys of Huntington, VA. in the form of forged 203-mm-diam. (approximately 1.5-m-long). The electrodes came from three heats; the compositions of the heats are presented in Table I. The final remelted ingots were approximately 254-mm-diam. by 508-mm-long.

The slag composition used during remelting was a 60 CaF_2/20 CaO/20 Al_2O_3 mixture (all compositions are in weight percent). Two batches of slag were utilized during the experimentation. The two slag compositions are presented in Table III.

3.3 INGOT PREPARATION

Following each ESR melt (with the exception of E15) the

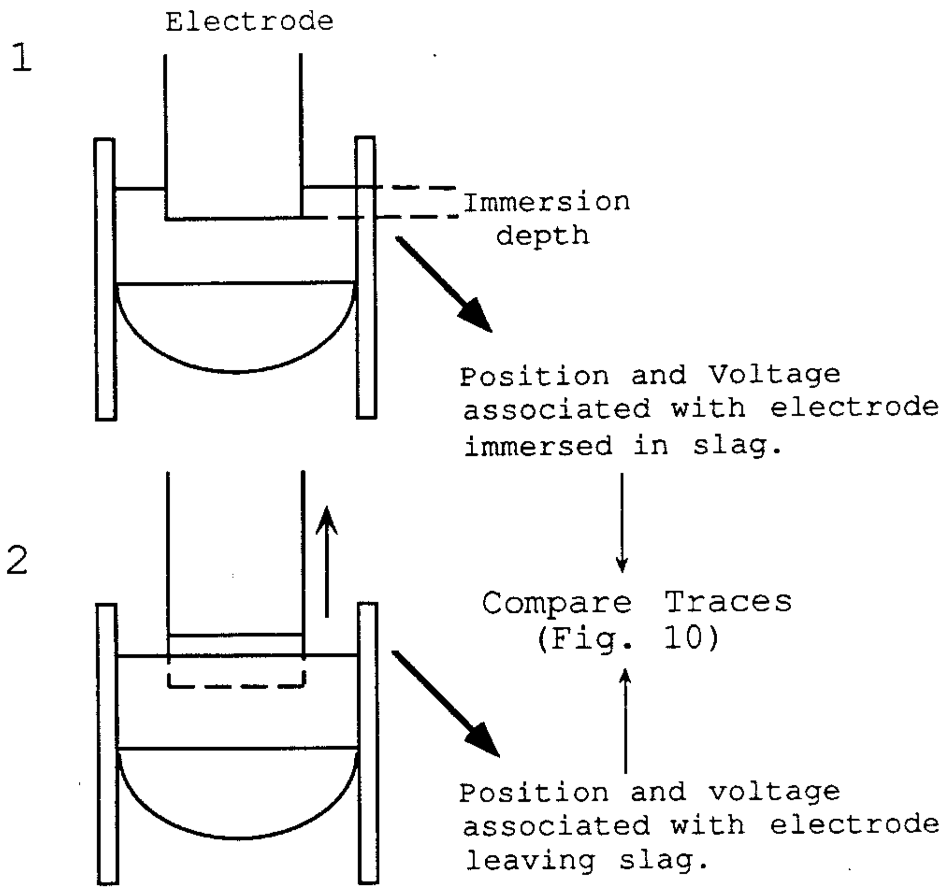

Figure 9. Schematic of the process to determine immersion depth during melting.

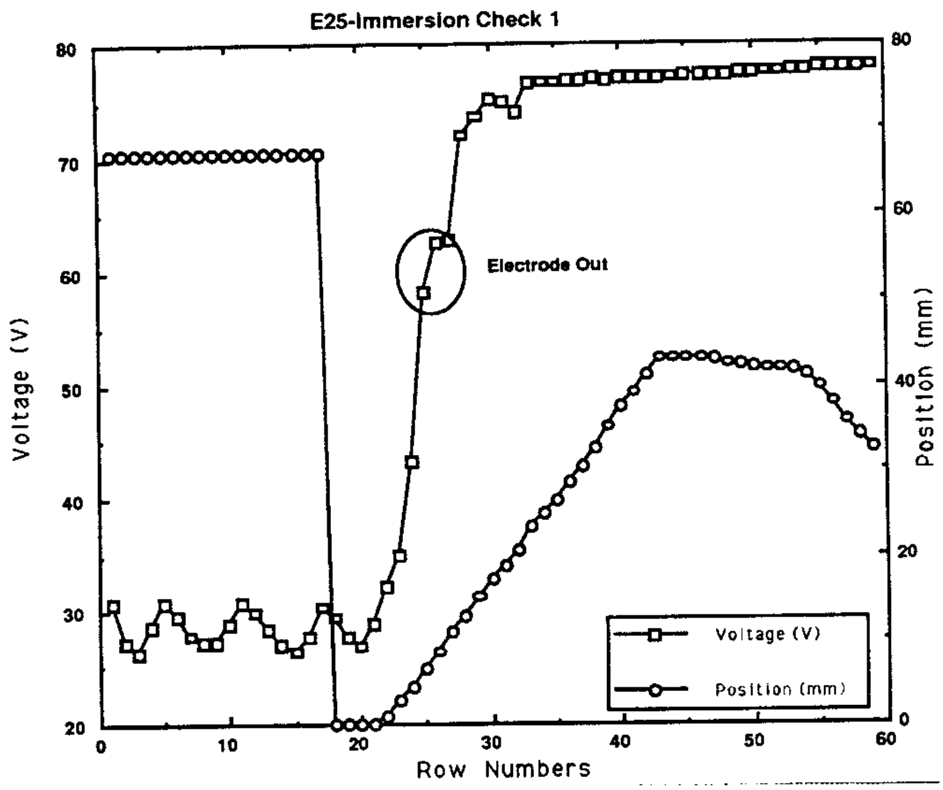

Figure 10. A comparison was made between the voltage trace and the electrode position trace, to determine immersion depth.

Table III

The batch compositions (in wt pct.) of the slag.

Order	CaF_2	CaO	MgO	Al_2O_3	SiO_2	C	S	MnO_2	Fe	TiO_2
#1	59.1	19.63	0.244	20.9	0.64	0.011	0.011	0.019	0.078	0.100
#2	59.34	19.50	0.262	20.93	0.62	0.011	0.011	0.018	0.077	0.100

ingot was marked to document its orientation with respect to the furnace. The location, within the ingot, of particular events and melt perturbations was determined through examination of the melt log and calculations of ingot growth rate based on measured melt rate.

Ingots, each of which represented a point in the factor space, were sectioned according to the schematic diagram in Figure 11. Each individual ingot was divided into four or five sections, numbered 1-5, depending on the ingot length; with one representing the top section and five representing the bottom section of the ingot. A 25-mm to 50-mm thick longitudinal slice was extracted from each melt for the macroanalyses. The goal of the sectioning was to isolate and examine steady state portions of each melt.

3.4 MACROSCOPIC ANALYSIS

3.4.1 Pool Profile Analysis

The steady state pool profiles were marked by physically adding tungsten powder (approximately 20 mesh) to the molten metal during melting. The tungsten was added from a position above the molten slag. The tungsten passed through the slag, through the molten metal, and settled at the tips of the dendrites. It was speculated that tungsten does not pass through the mushy zone of the solidifying

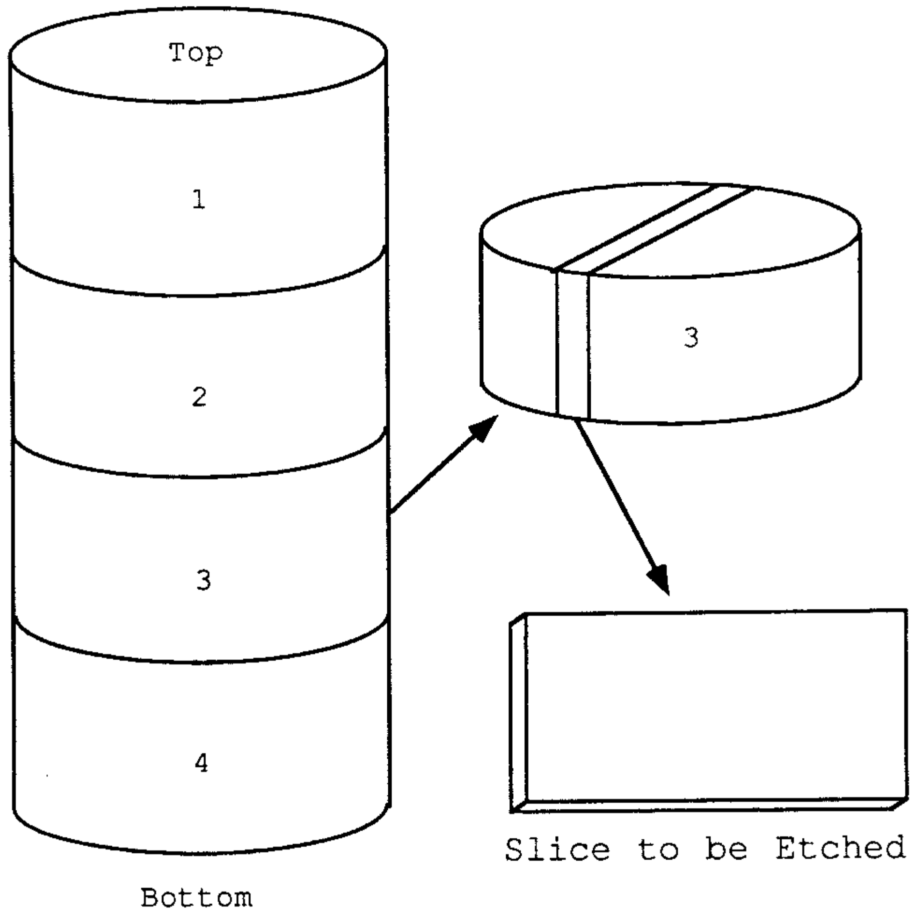

Figure 11. Ingot sectioning to obtain longitudinal slice - schematic.

ingot. Each slice was macroetched (25 parts hydrochloric acid and 2 parts nitric acid heated to 160°F) to highlight the melt pool shapes. The pools were characterized in terms of pool volume, depth, and symmetry. The pool depths were measured along the centerline of the pool profile. The pool volumes were determined using a MacIntosh based image analysis system to calculate the areas of each half pool and the associated centroids in order to calculate a volume. The two volumes were then averaged for an estimation of the entire pool volume. The ratio of the volume associated with the smaller half to the volume associated with the larger half was used as a measure of pool symmetry.

3.4.2 Dendrite Analysis, LST Calculation

For each slice, low magnification (20-30x) micrographs were taken from below the edge, mid-radius, and center of a designated pool (as illustrated in Figure 12) for the purpose of characterizing secondary dendrite arm spacing (DAS). The dendrite spacing was measured using a linear intercept technique[36]. A secondary dendrite arm spacing/LST equation was predicted using measured secondary dendrite arm spacing and local solidification time values that were calculated/predicted from the model developed by Ballantyne[11]. The local solidification times for the

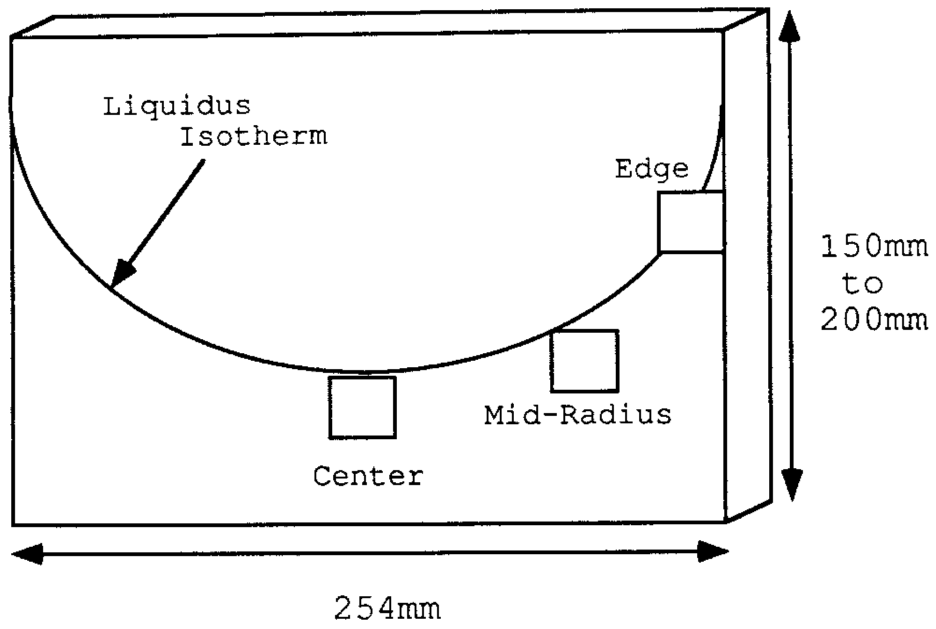

Figure 12. Position, relative to steady state pool, that samples were extracted in order to measure secondary DAS.

steady state sections of the experimental melts, were determined using the formulated dendrite arm spacing/local solidification time relation for alloy 625.

3.4.3 Macro-Segregation Analysis

Macro-slices were analyzed for niobium, iron, molybdenum, chromium and nickel segregation. For each of the elements, concentration maps were produced using a Kevex Omnichrone X-Ray Fluorescence Mapping System at Sandia National Laboratory. Slices from melt numbers E27 and E28 were partitioned, as shown in Figure 13, and analyzed.

3.5 SLAG SKIN ANALYSIS

Slag skin samples were removed from areas on the solidified ingot that represented steady state sections. For each sample, slag skin thickness was measured and tabulated.

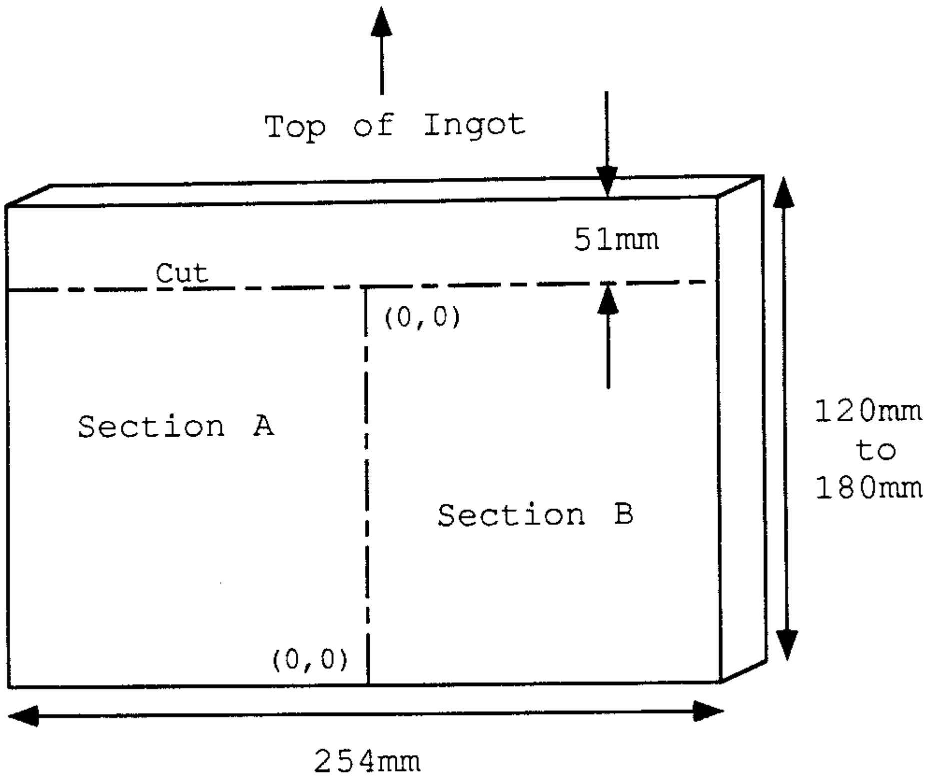

Figure 13. Schematic of how slices from E27 and E28 were partitioned for macrosegregation analysis. The point (0,0) orients the compositional map.

4.0 RESULTS AND DISCUSSION

The experimentation included the measurement and correlation of a wide variety of data. Table IV lists the experimental melt parameters evaluated in this work. Table V lists the measured aspects of solidification structure. During each melt, specific perturbations occurred during the course of experimentation which could be considered external to what normally takes place during industrial electroslag remelting. Those external perturbations included: immersion checks and the addition of tungsten. Experimental perturbations that may be experienced during normal industrial ESR operation include: power interruptions, the physical addition of slag, and voltage fluctuations.

The etched steady state slices which emphasized macrostructure were analyzed to determine the effects of the previously mentioned process perturbations. Figures 14-22 present ingot maps, one map for each melt, showing the positions of observable pool profiles and indicating the specific perturbations that corresponded with those pool positions. Macrographs of the etched steady state slices are included with the respective ingot map.

The tungsten was added to mark a specific pool profile.

Table IV

Measured experimental parameters.

Melt Number	Power (kW)	Immersion Depth (mm)	Gap Distance (mm)	Slag Cap (mm)	Mold to Stool Ratio	Melt Rate (kg/ks)	Voltage (V)	Current (kA)
E15	120.8	33.5	103.8	137.3	2.53	43.3	28.8	4.5
E22	223.6	12.5	73.3	85.8	0.40	90	32.3	6.91
E23 T1	92.6	15.3	85.0	100.3	0.15	30.0	28.8	3.22
E23 T2	95.9	13.7	85.6	99.3	0.15	26.7	29.8	3.22
E24	213.5	47	111.7	158.7	4.63	51.7	30.4	7.0
E25 T1	77.6	41.5	94.7	136.2	0.11	16.7	21.7	3.58
E25 T2	78.0	40.5	95.0	135.5	0.11	18.3	21.8	3.60
E26 T1	241	10.5	155.0	165.5	4.07	56.7	39.1	6.17
E26 T2	241.4	12.5	154.3	166.8	4.33	61.7	39.2	6.18
E27 T1	139.3	14.1	154.9	169	2.1	58.7	36.6	3.81
E27 T2	142.66	11.6	154.4	166	3.37	58.7	36.9	3.87
E28	132.1	64	4.7	69	0.45	42.7	19.3	6.92
E29 T1	138.0	49	73	122	1.64	39.2	24.3	5.0

Table V

The measured aspects of solidification structure.

Melt Number	Slag Skin (mm)	Pool Depth (mm)	Pool Volume ($x10^{-3}mm^3$)	Pool Asymmetry Factor	LST Center (sec)	LST Mid-Radius (sec)	LST Edge (sec)
E15	0.0	128	2574	0.64	513	312	218
E22	0.8	250	6004	0.95	178	167	64
E23 T1	1.2	35	1063	0.93			
E23 T2	1.3	35	1157	0.98	623	316	157
E24	1.5	151	3994	0.90	485	277	81
E25 T1	6.5	18	483	0.89	523	485	167
E25 T2	6.5	20	618	0.92			
E26 T1	0.0	117	2597	0.77	449	263	127
E26 T2	0.0	125	2841	0.95			
E27 T1	0.0	45	1000	0.99	350	225	93
E27 T2	0.0	50	920	0.92			
E28	11.0	198	7002	0.89	467.3	290.7	(1)
E29 T1	0.0	100	2551	0.93	449.5	263.2	64

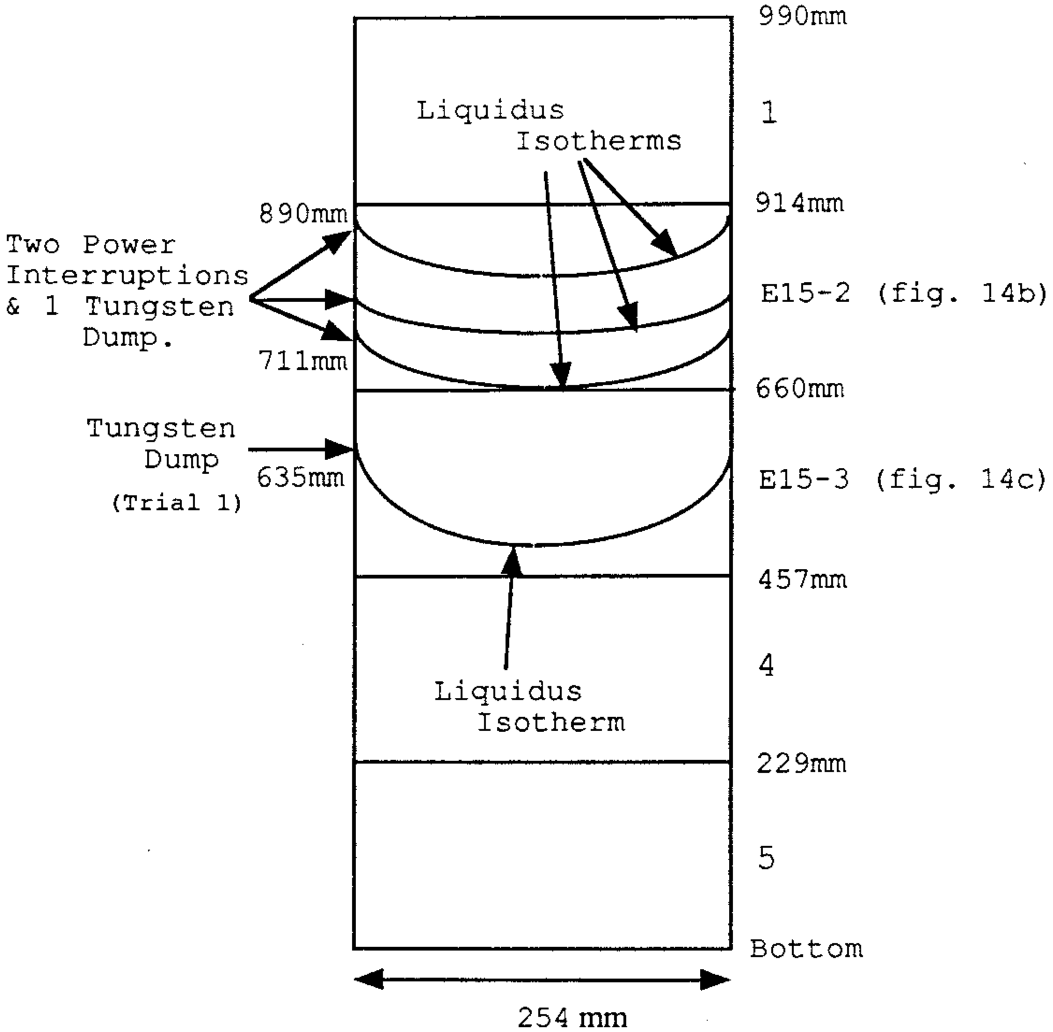

Figure 14a. The ingot map representing a longitudinal section of melt E15, showing the position of observable pool profiles. Etched sections 2 and 3 shown in Fig 14b. and 14c. respectively.

Figure 14b. The steady state section E15-2. Both the addition of tungsten and the interruptions of power were responsible for marked pool profiles.

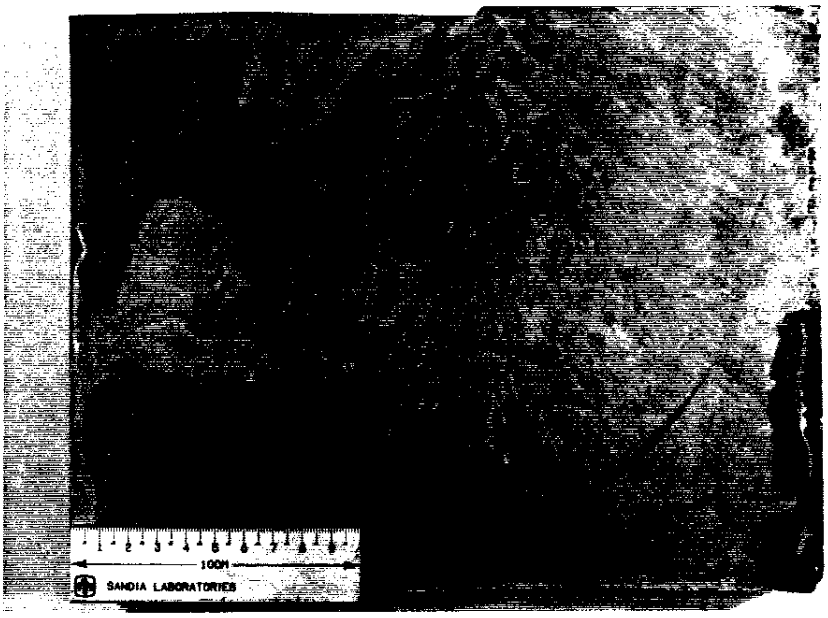

Figure 14c. Slice E15-3 showing the steady state pool profile associated with melting under the following conditions: Current= 4.5 kA, Slag Cap Thickness= 137 mm, and Immersion= 34 mm.

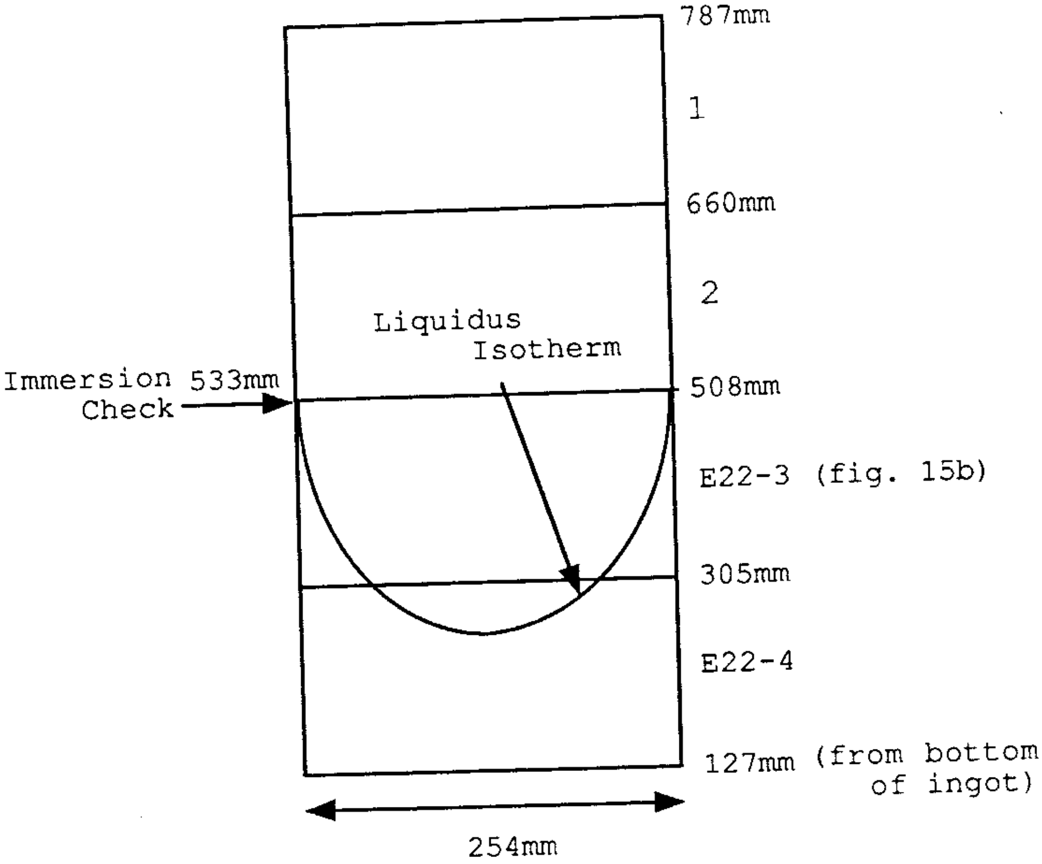

Figure 15a. Ingot map for melt E22 showing the pool present and the position of the immersion check that marked the pool.

E22-3

E22-4

Figure 15b. Etched longitudinal slices E22-3 and E22-4 representing the steady state portion of melt E22. E22 was melted with Current= 6.9 kA, Cap thickness= 86 mm, and Immersion= 13 mm.

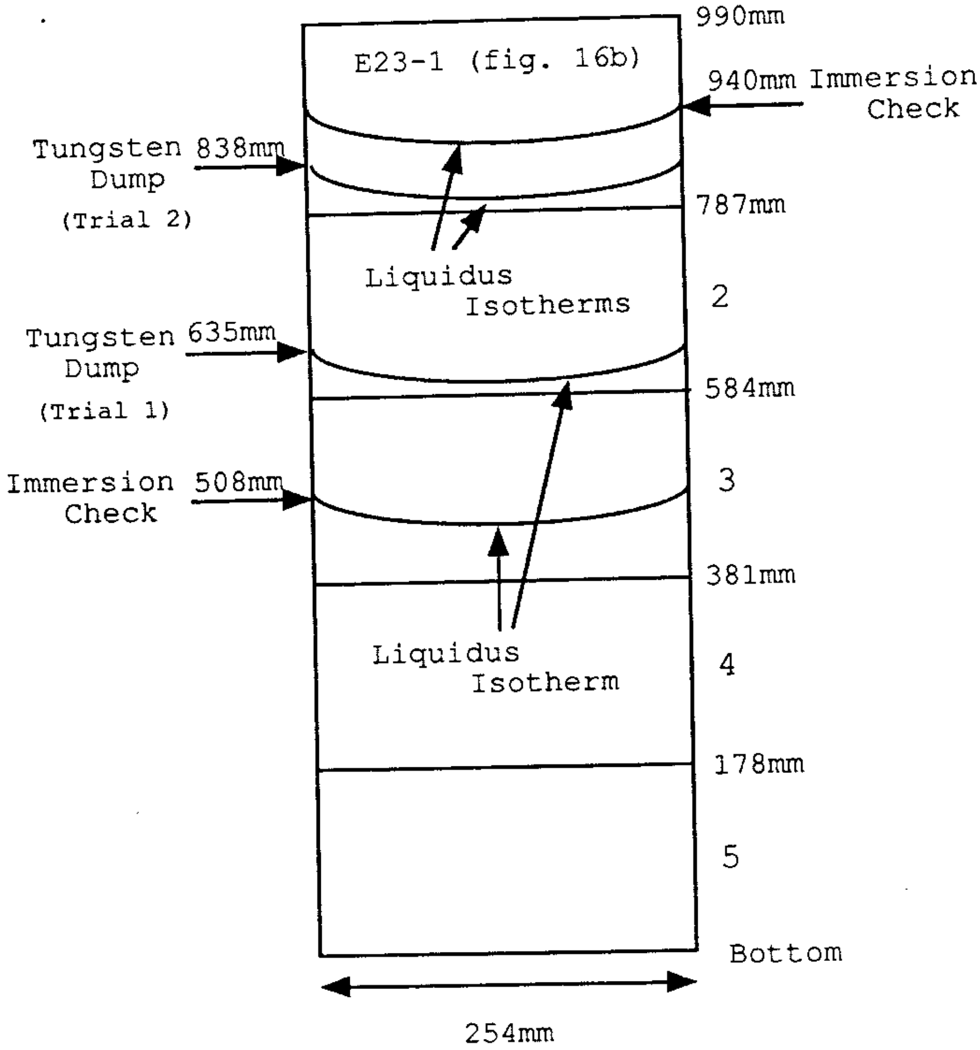

Figure 16a. Ingot map for melt E23 showing the pool profiles present and the corresponding perturbations that marked them.

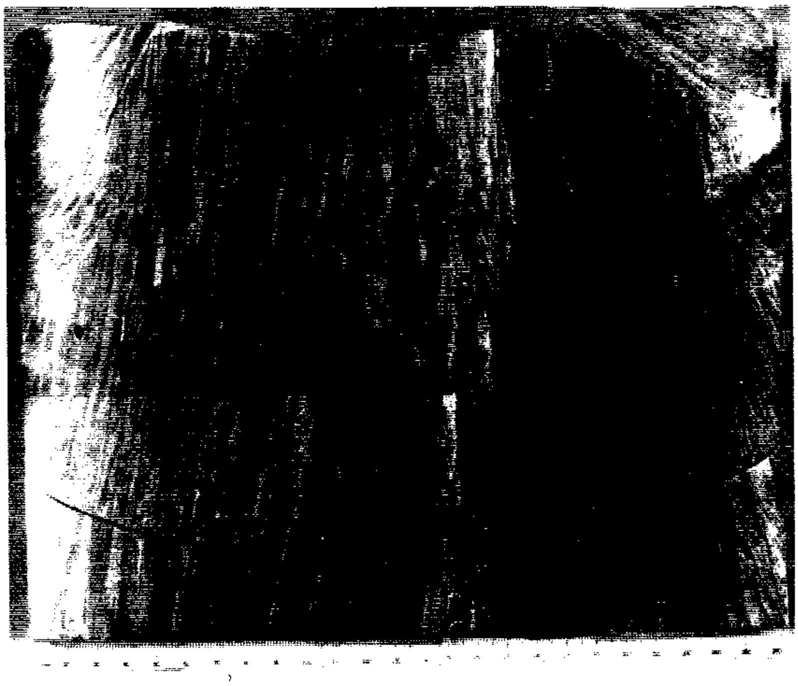

Figure 16b. Steady state section E23-1 showing the pool profile marked with tungsten. E23 melting parameters: Current= 3.2 kA, Slag Cap Thickness= 100 mm, Immersion= 15 mm.

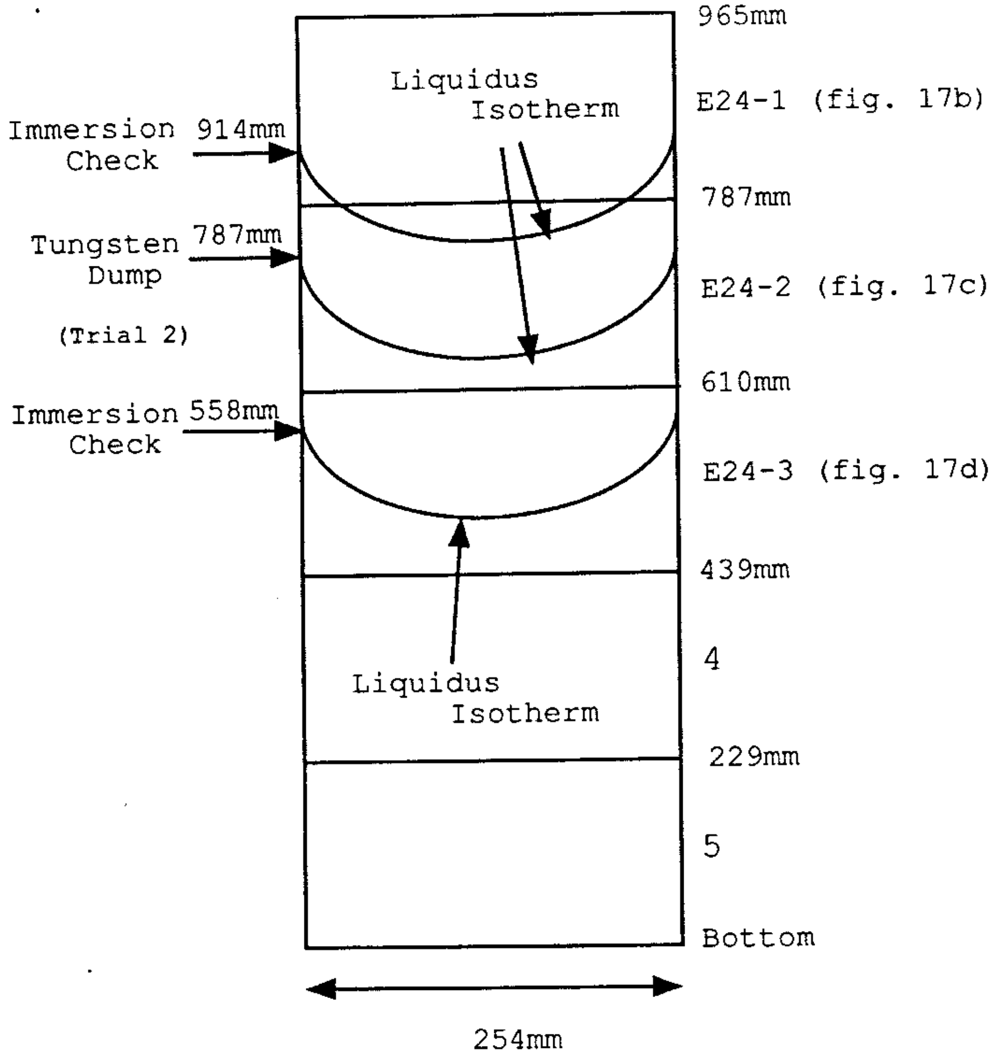

Figure 17a. Ingot map showing the positions of pool profiles and the perturbations that marked them. Etched slices: Fig.17b. E24-1, Fig. 17c. E24-2, Fig.17d. E24-3.

b.

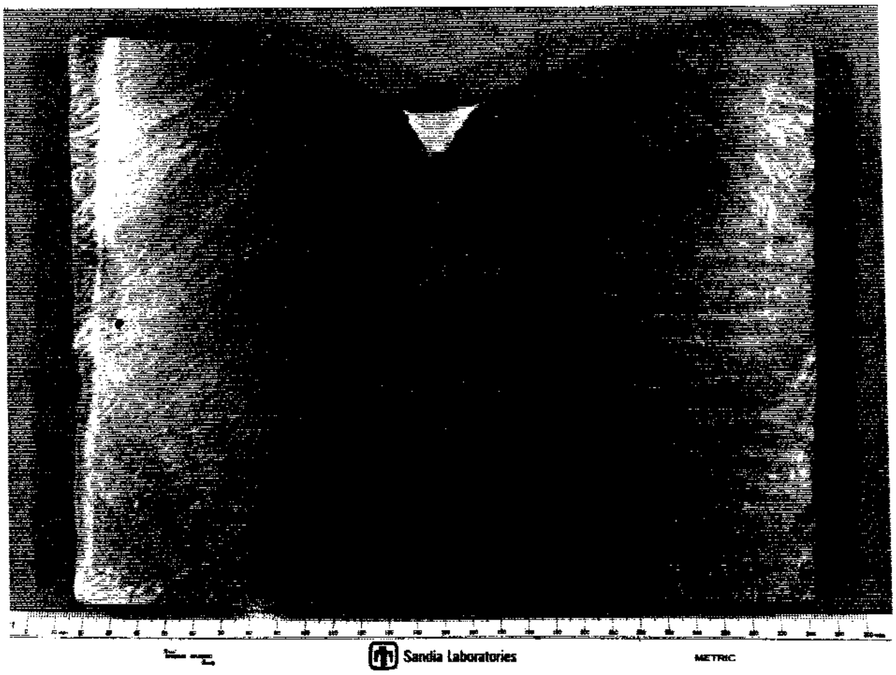

c.

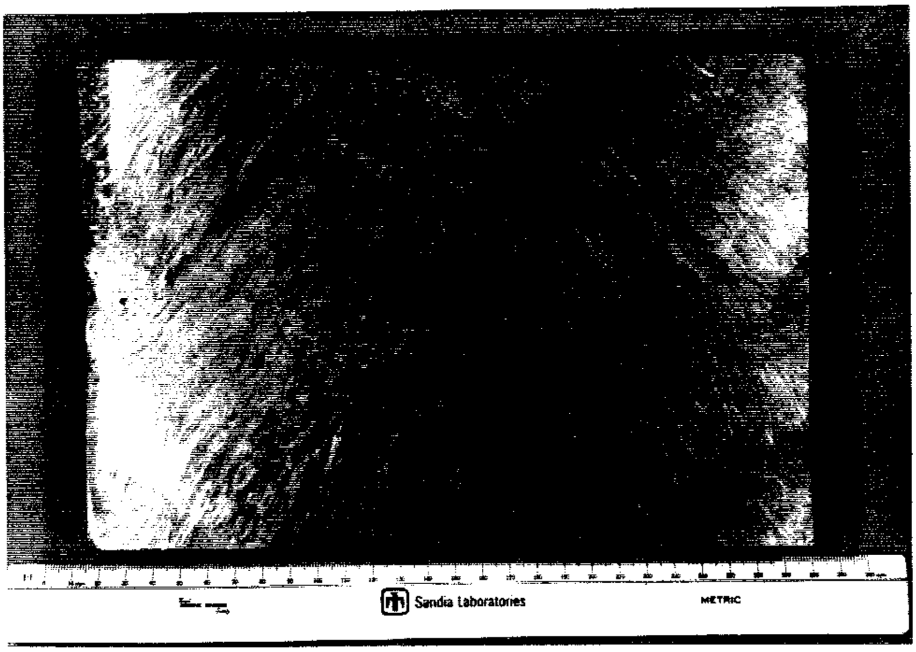

Figure 17b. Steady state section E24-1.
17c. Steady state section E24-2. Parameters: Current= 7.0 kA, Slag Cap= 159 mm, and Immersion= 47 mm.

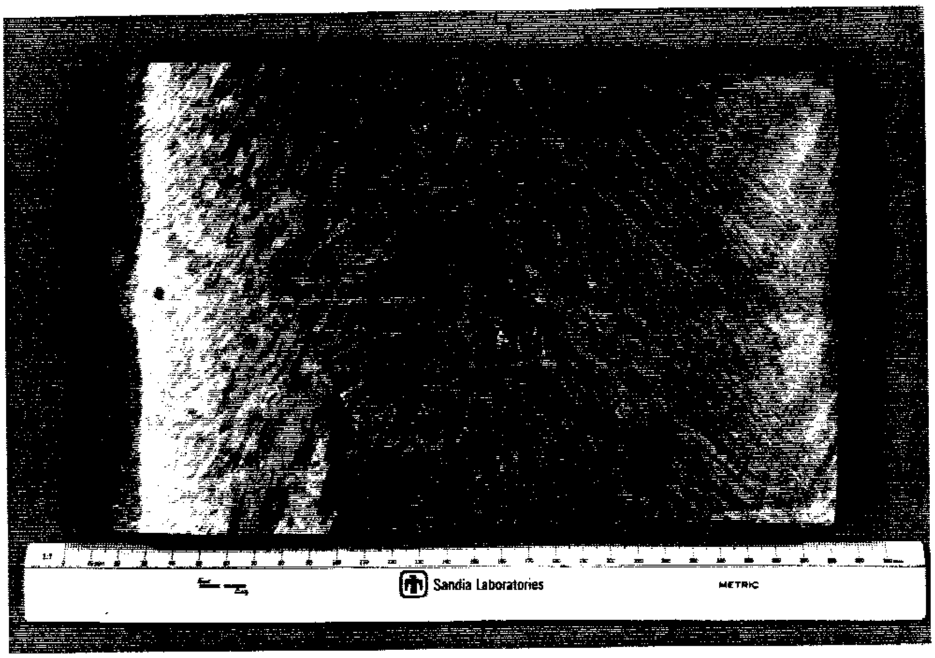

Figure 17d. Etched slice representing section E24-3. The marked pool profile represents the effect of an immersion check.

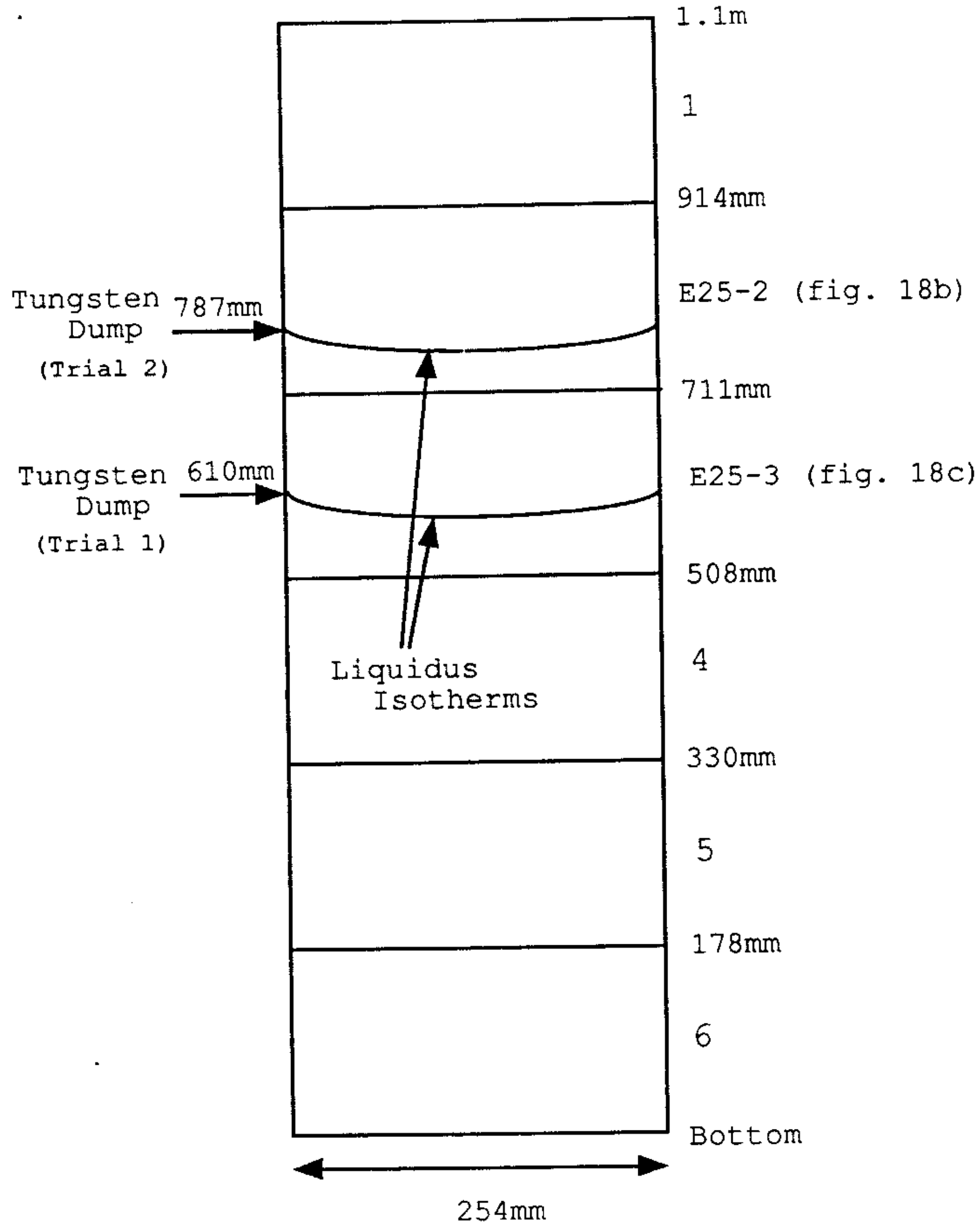

Figure 18a. The ingot map for E25 indicating the positions of pool profiles and the perturbations that marked them. Etched Slices: Fig.18b. E25-2, Fig.18c. E25-3.

b.

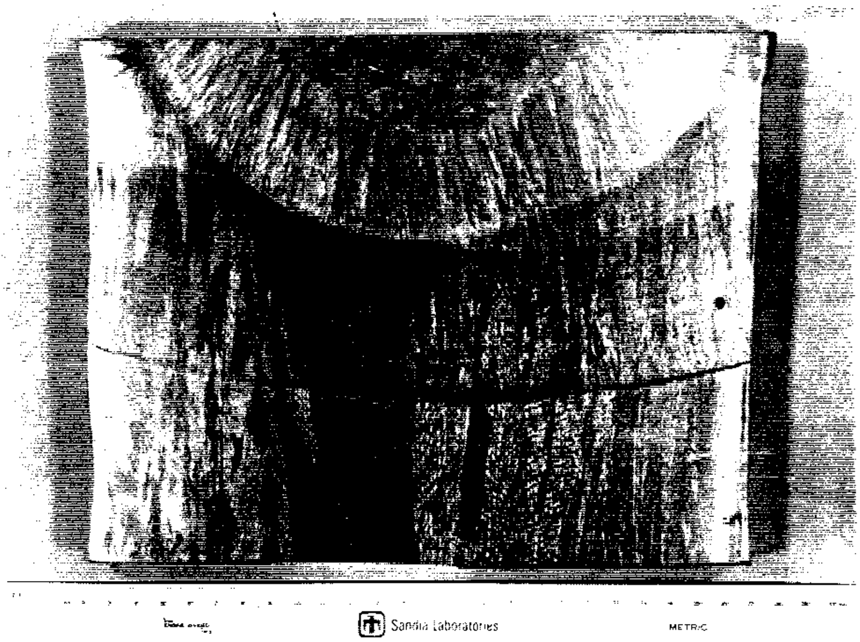

c.

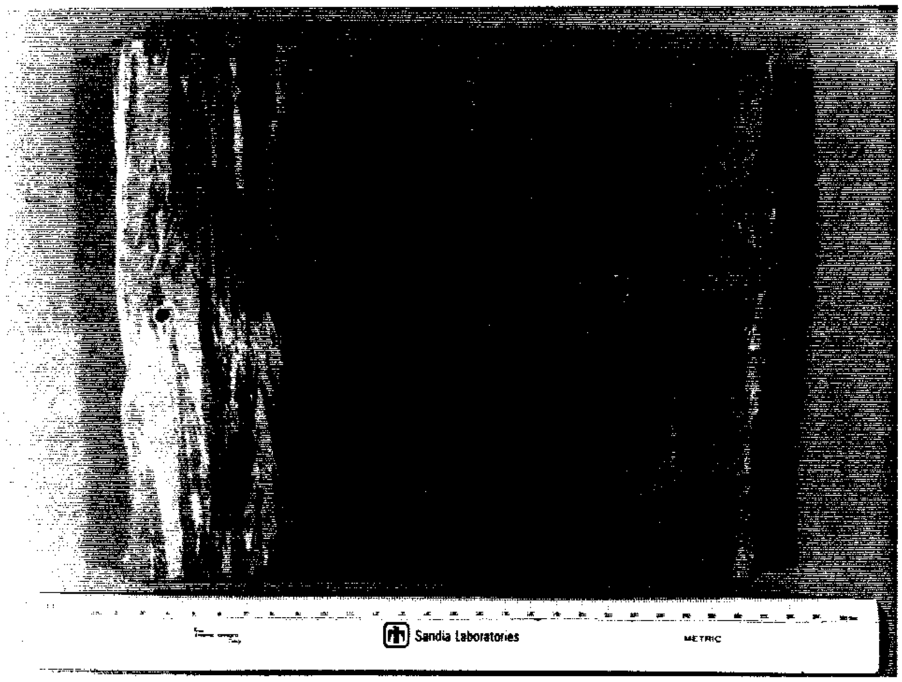

Figure 18b. Steady state section E25-2.
18c. Steady state section E25-3. Parameters: Current= 3.6 kA, Slag Cap= 136 mm, and Immersion= 42 mm.

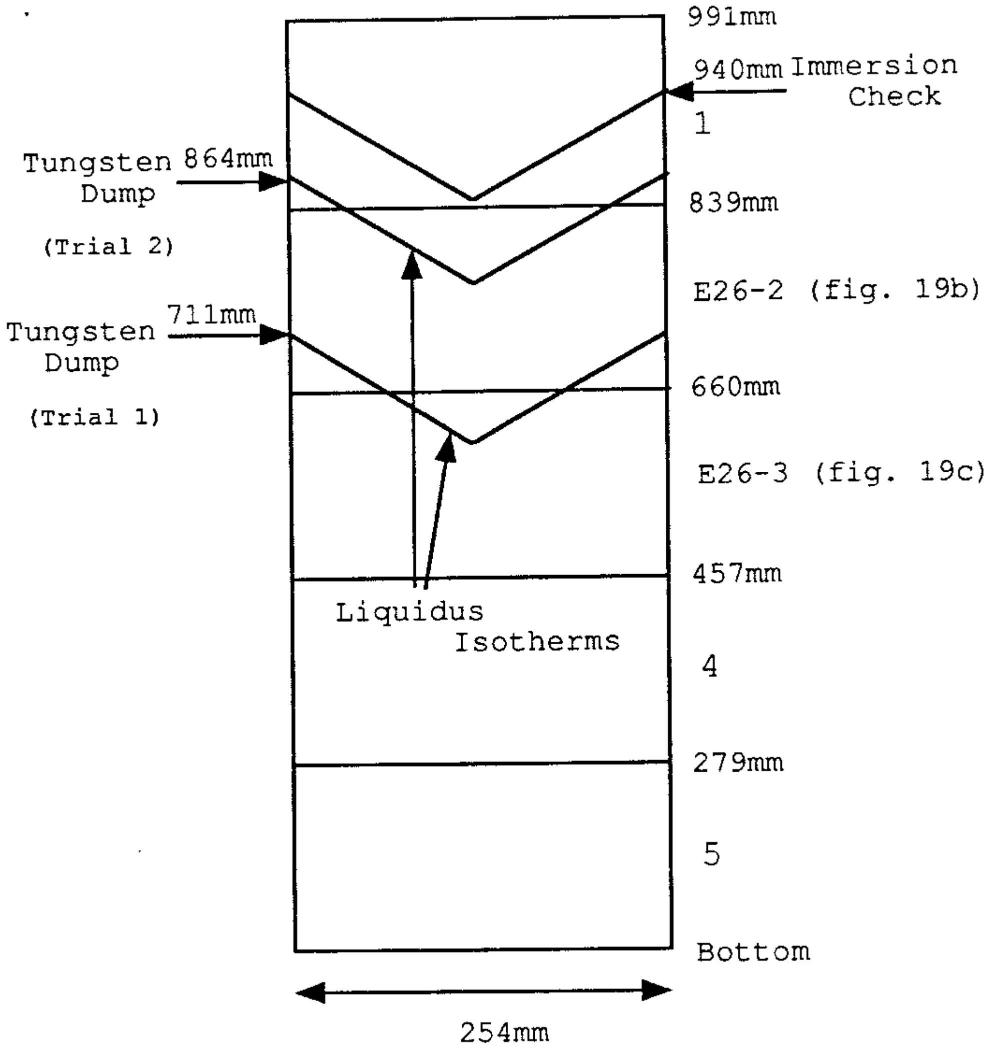

Figure 19a. Longitudinal ingot map for E26, showing the positions of marked pool profiles and the associated perturbations. Etched slices Fig. 19b. E26-2, and Fig. 19c. E26-3.

b.

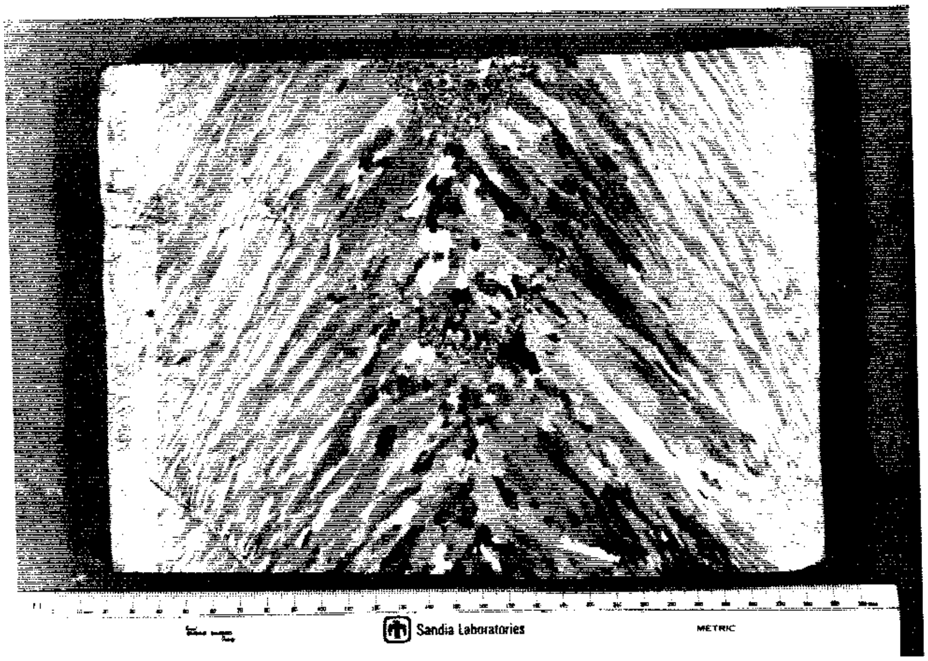

c.

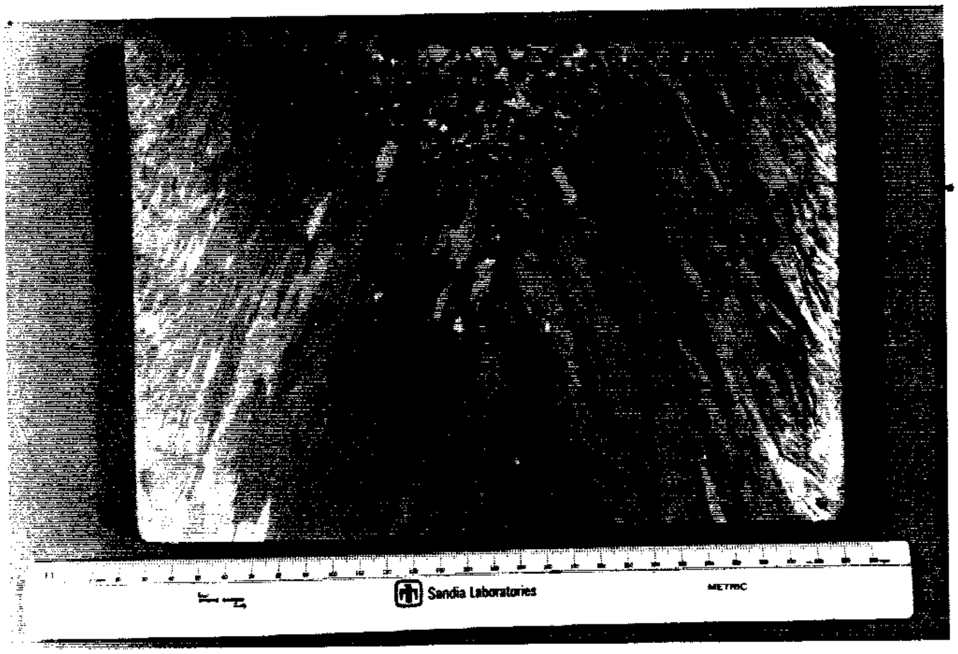

Figure 19b. Steady state section E26-2
19c. Steady state section E26-3 Parameters: Current= 6.2 kA, Slag Cap= 166 mm, and Immersion = 11 mm.

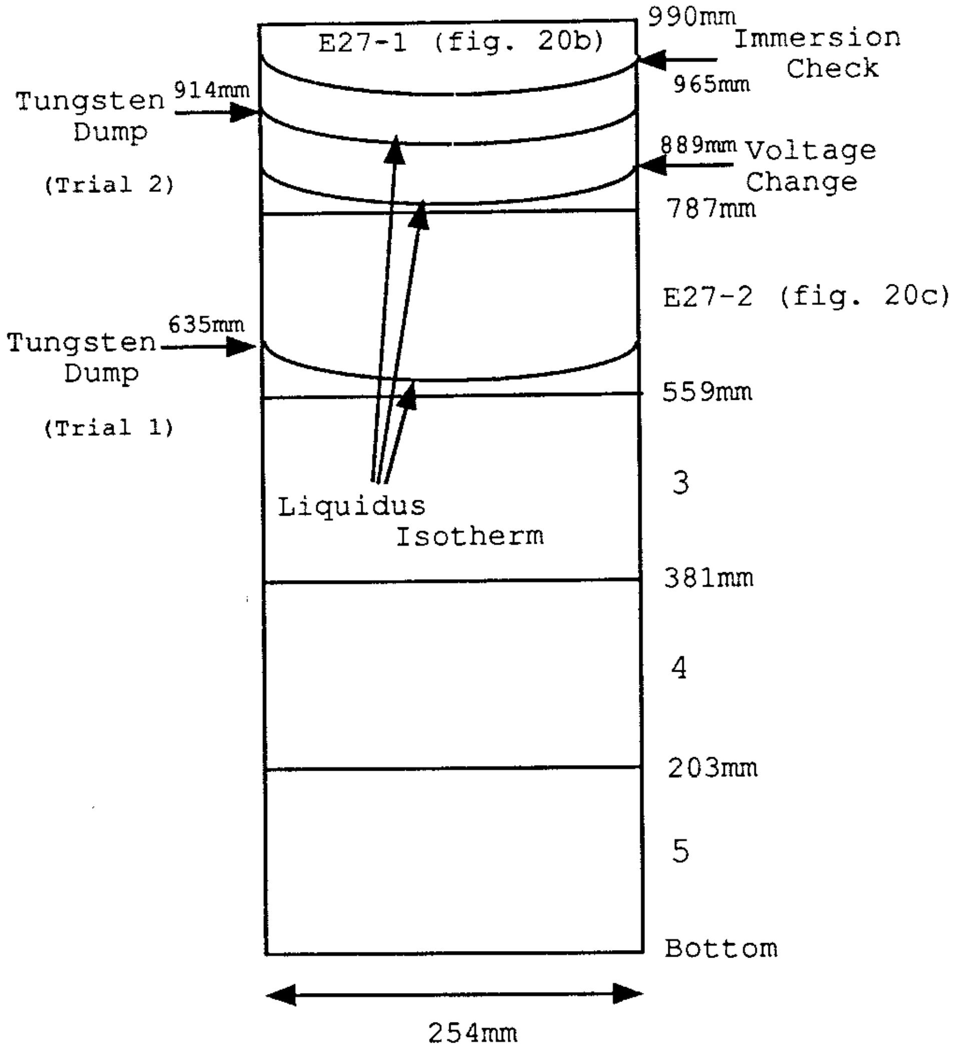

Figure 20a. Ingot map for melt E27 showing the position of the marked pool profiles and the associated perturbations. Steady state sections in Fig. 20b and 20c.

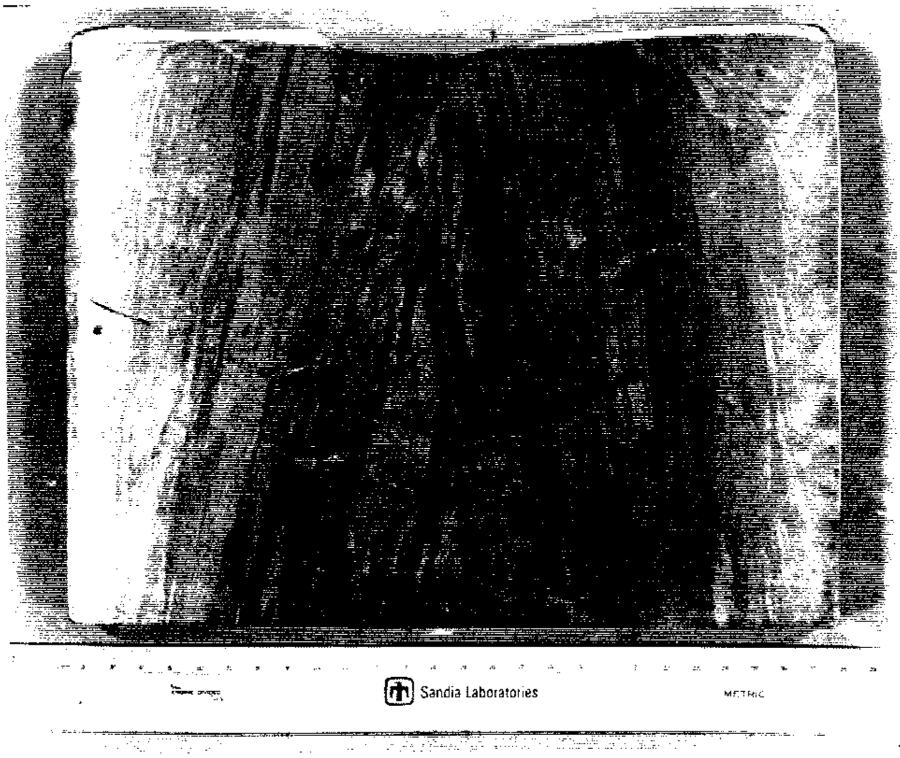

Figure 20b. Slice E27-1 representing a steady state portion of E27. The melting parameters responsible for the pool: Current= 3.9 kA, Slag Cap= 166 mm, and Immersion= 12 mm.

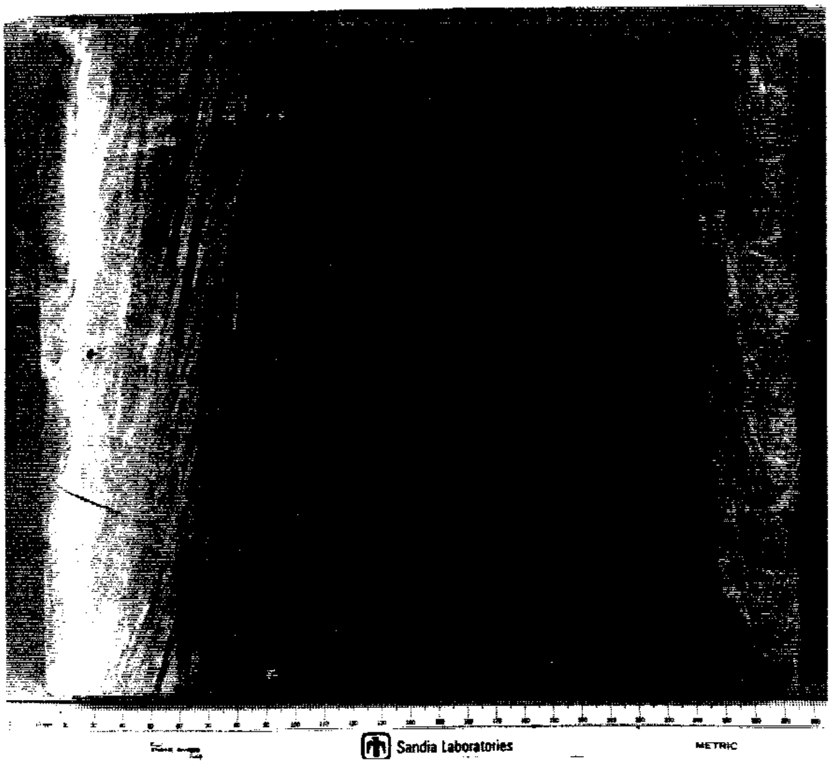

Figure 20c. Slice E27-2 representing another steady state portion of melt E27.

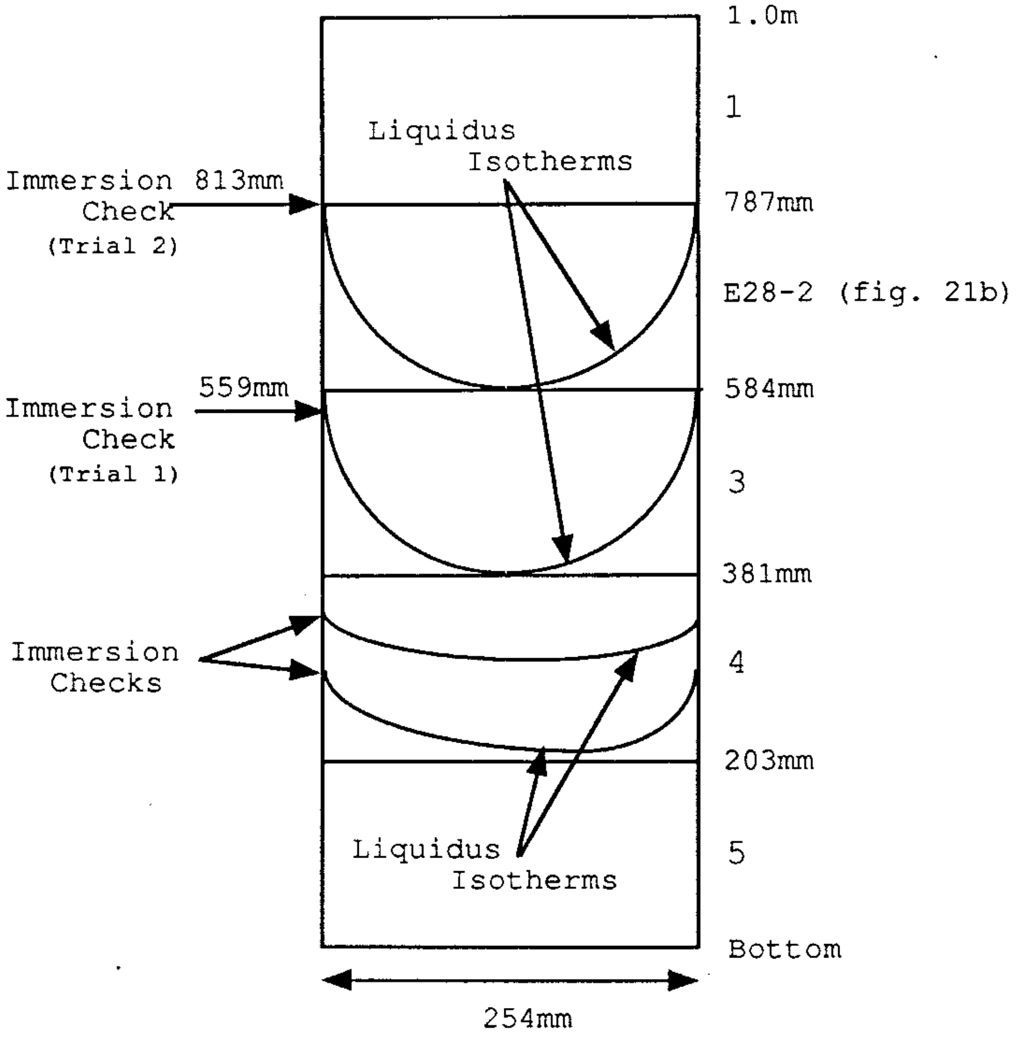

Figure 21a. The ingot map for melt E28 showing positions of marked pool profiles. During the melt, E28-2 represents the only steady state region (Refer to Fig. 21b.).

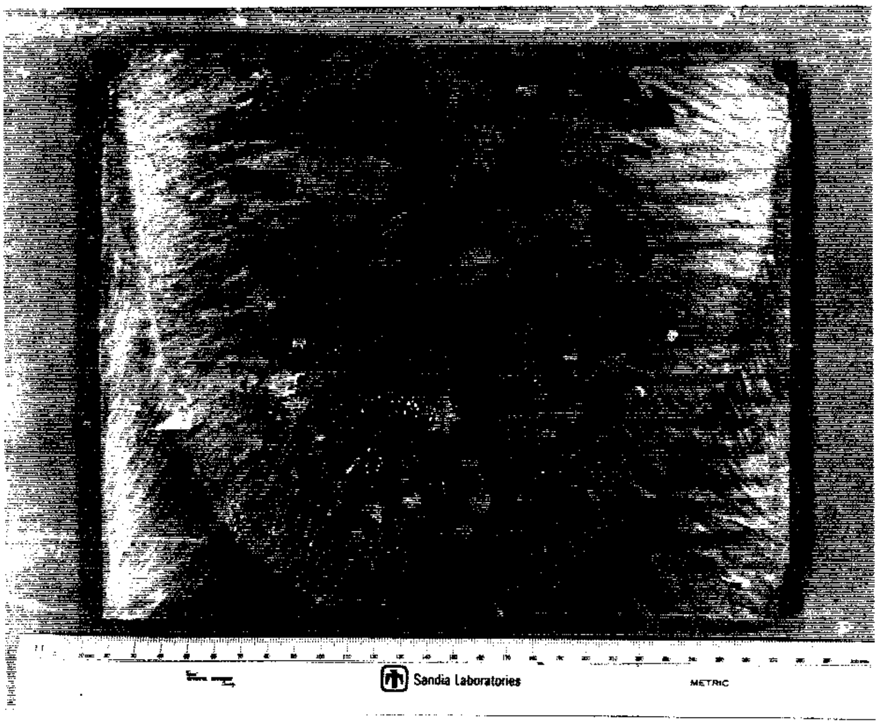

Figure 21b. This pool was marked by an immersion check. E28 had an 11-mm slag skin and was melted under the following conditions: Current= 6.9 kA, Slag Cap = 69 mm, and Immersion = 64 mm.

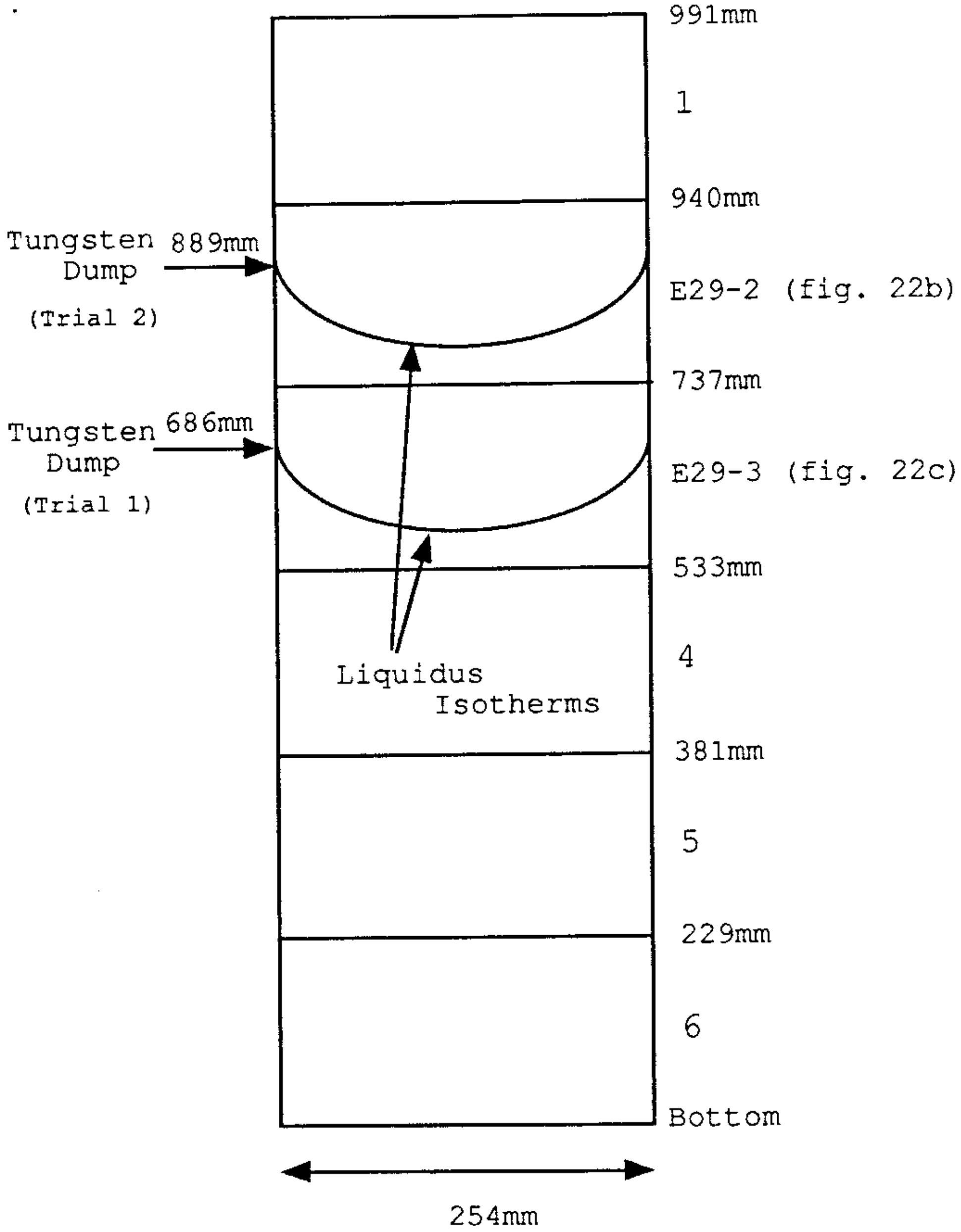

Figure 22a. The ingot map for melt E29 showing the positions of observable pool profiles and the associated perturbations.

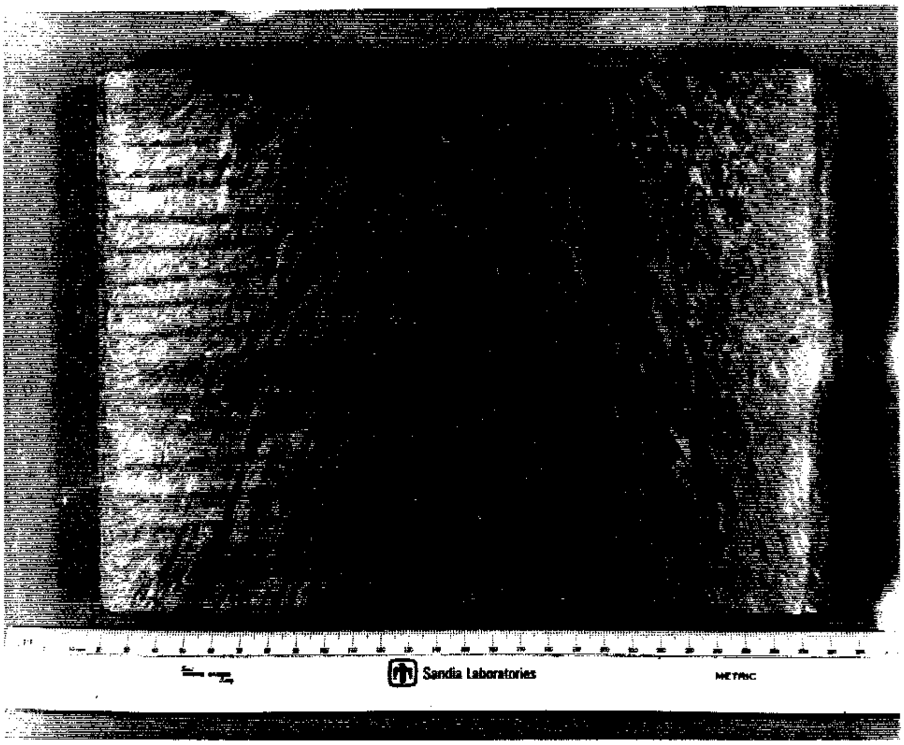

Figure 22b. The pool profile in slice E29-2 marked by the additions of tungsten under the following melt conditions: Current = 5.0 kA, Slag Cap = 122 mm, and Immersion = 49 mm.

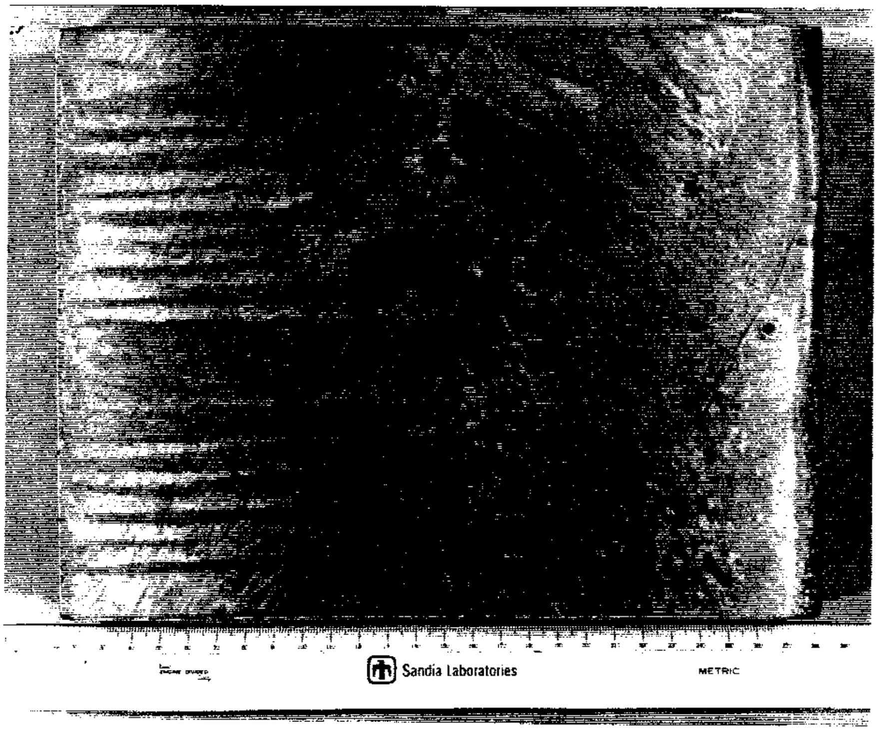

Figure 22c. Slice E29-3 representing another steady state portion of E29. This pool was also marked by the addition of tungsten.

In the case of melt E15, the intentional interruption of power for thirty seconds was another method for marking pool profiles. Figure 14b shows how two power interruptions and one tungsten addition affected the solidification structure. Even though the power interruption marked the pool profile, it also represented a physical interruption in steady state melting. Tungsten also marked the pool but did not effect the steady state melting conditions. Therefore tungsten was used throughout the rest of the experimental melts.

The degree at which tungsten marked the pool profile varied from melt to melt. The addition of tungsten not only left a dark band tracing the profile, but in some cases altered the ingot steady state solidification structure. The addition of tungsten caused enough of a perturbation to develop a new solidification front as evidenced by the fine grained structure along the pool profile which indicated an alteration had taken place in the cooling rate, as seen in Figures 17b, 17c, 19b, 19c, 22b, and 22c. In addition to a new solidification front, the steady state sections of melt E26 (Figures 20b and 20c) are distinguishable by the pronounced nucleation of fine equiaxed grains. The melt E26 slices showed clearly a progression from very fine equiaxed structure near the pool profile to a large equiaxed structure as solidification proceeded. It was observed, particularly in melt E26, that the fine equiaxed structure was concentrated at the very bottom center of the pool. Although the variations in density between the liquid and solid during solidification of Alloy 625 was not determined, the concentration of fine grained equiaxed structure at the center and bottom of the pool indicated that the solid was more dense than the liquid. Segregation to the bottom of the pool resulted from settling of the fine equiaxed structure.

During the shallow profile melts shown in Figures 18b, 18c, 20b, and 20c; tungsten marked the pool profile well. The shallow profile melts E23, E25, and E27 exhibited a less pronounced transition from fine grained to coarse grained structure as solidification proceeded.

During the deep pool profile melts E28 and E22, with 198-mm and 250-mm depths respectively, there was no evidence the addition of tungsten marked the pool profile. For these particular melts, immersion checks were responsible for marking the pool profiles. The immersion checks also marked pools by altering the solidification locally at the time and position the immersion check was performed. During an immersion check, extraction of the electrode from the slag caused an interruption in power input, and the molten metal cooled at a faster rate than if the electrode had continued to stay in the slag and continuous power flow had not been interrupted. This change in the cooling rate and the eventual reestablishment of steady state resulted in the formation of a fine columnar structure along the liquidus isotherm as depicted in Figures 21b (melt E28) and 17b (melt E24).

The data indicated that both tungsten additions and immersion checks were able to mark steady state pool profiles. The degree at which either method altered the solidification structure was dependent upon pool depth. For pools greater than 200 millimeters in depth, the tungsten becomes too dispersed in the large volume of molten metal to be able to distinctly mark the pool.

Throughout the data analysis, measured elements such as pool depth, volume, slag skin thickness, and local solidification time were related to the input power of the system. The input power was recognized as being important because it was the primary driver for the melting process. The power could be altered by any combination of process parameters whether changes were being made in the current, the immersion depth, or the slag cap thickness.

Throughout the literature, researchers have concentrated on a comparison of melt rate with such solidification aspects as cooling rate, local solidification time, and pool depth. In most cases it was assumed that melt rate was proportional to input power. Figure 23, which plotted melt rate versus power for the experimental melts, confirmed the proportional relation between melt rate and power. The plot also indicated, since a best fit line would not go through the origin, that all input power did not directly affect the melt rate.

Evaluations of heat transfer in the literature[37] has indicated that during electroslag remelting, numerous paths exist through which heat can be distributed. Part of the heat goes into melting of the electrode, which affects melt rate. Heat can be transferred to the cooling water across the ingot/slag skin/mold interface. Heat can also be transferred to the cooling water across the slag/mold interface. Finally, heat can be transferred to the cooling water in the base plate. These alternate heat paths each consume a fraction of the total input power to the system.

4.1 POOL PROFILE

4.1.1 Efficiency

The process efficiency is an important concern to industry because it describes the electrical cost of melting, measured in kilowatts hours per kilogram. An efficiency study was accomplished by evaluating the ratio of

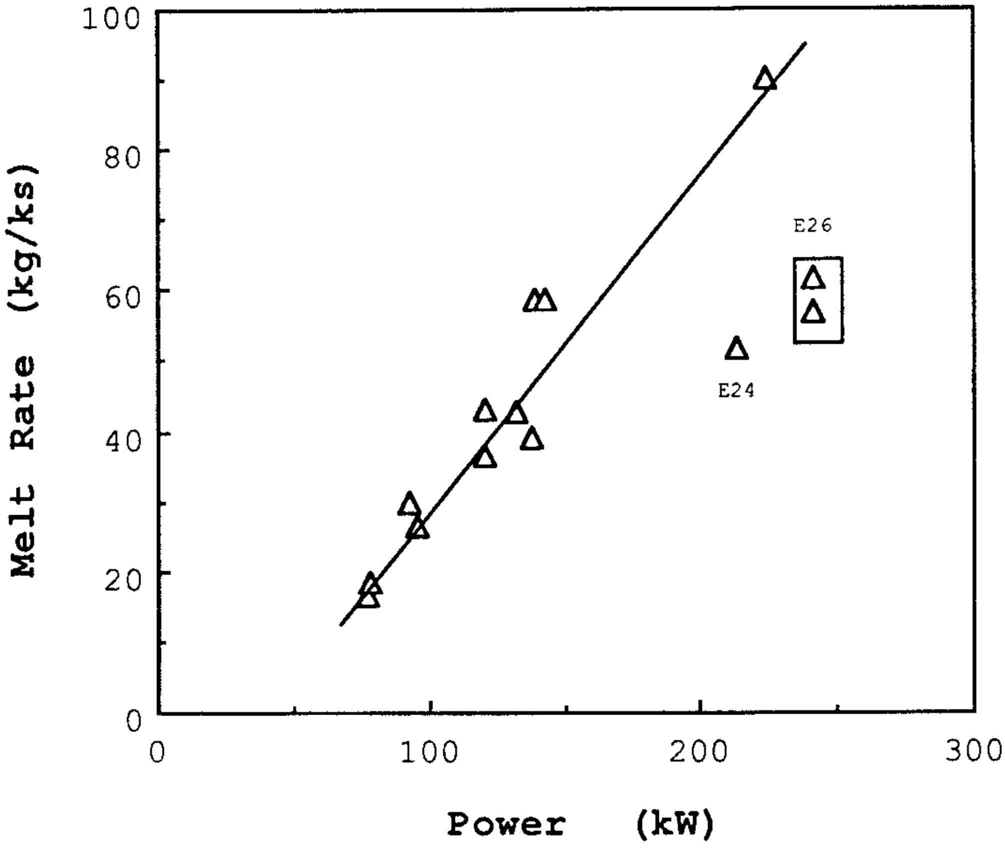

Figure 23. Melt rate versus power for the experimental melts.

power to melt rate in kilowatts kiloseconds per kilogram. Kilowatt hour per kilogram varies with kilowatt kilosecond per kilogram by a factor of approximately 0.3. This ratio is inversely proportional to a measure of process efficiency. A high power to melt rate ratio describes an inefficient process, while a low ratio describes an efficient process. Primarily, this ratio was compared with the power input to the system. The input power was used because, 1) it was a direct function of current and voltage, both of which can be controlled within tight tolerances, and 2) it represented the actual input of the system. It is difficult to correlate the process efficiency with individual parameters such as current and voltage. After establishing the relation between power and efficiency, the interactive effects of immersion depth, slag cap thickness, and the electrode to pool gap distance, were determined. These comparisons provided insight into how melt variables affected process efficiency during electroslag remelting.

Figures 24, 25, and 26 show the power to melt rate ratio as a function of current. Fig. 24 highlights variations in slag cap thickness, Fig. 25, variations in electrode to pool gap distance, and Fig. 26, variations in immersion depth. These data show that the efficiency of the system increased with increasing power, with the exception

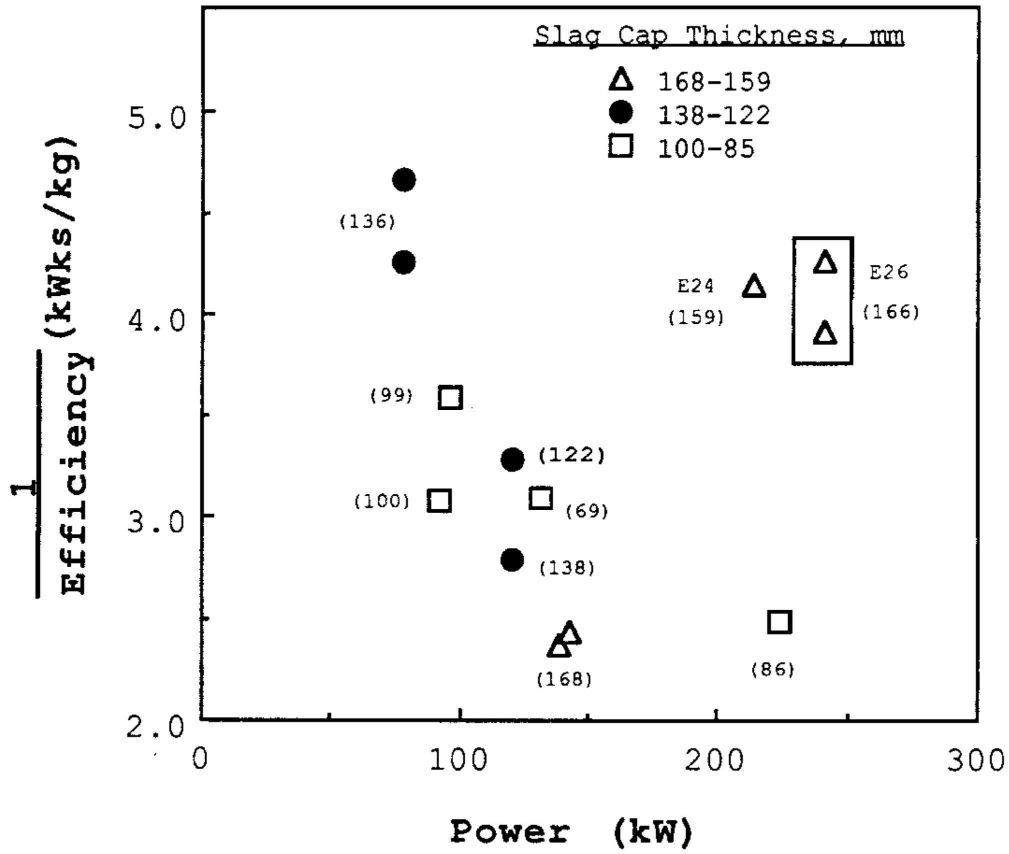

Figure 24. Relation between a power to melt rate ratio and power, emphasizing changes in running slag cap thickness.

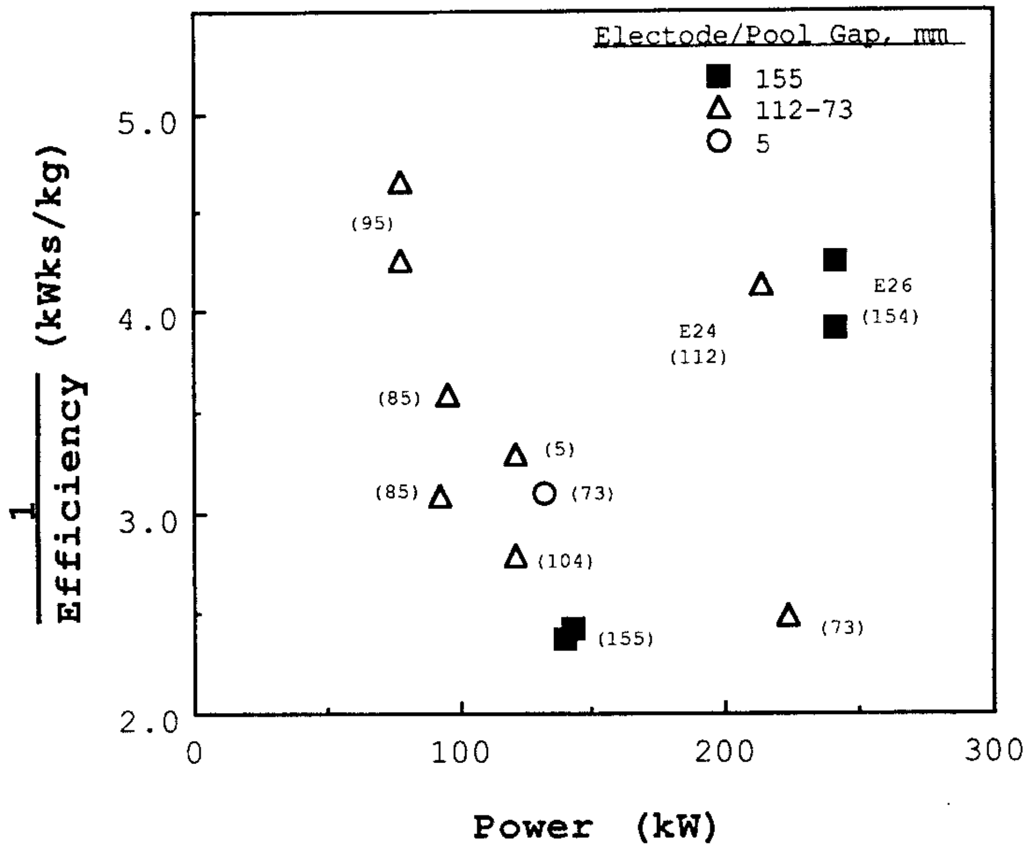

Figure 25. Relation between a power to melt rate ratio and power emphasizing changes in electrode to pool gap distance.

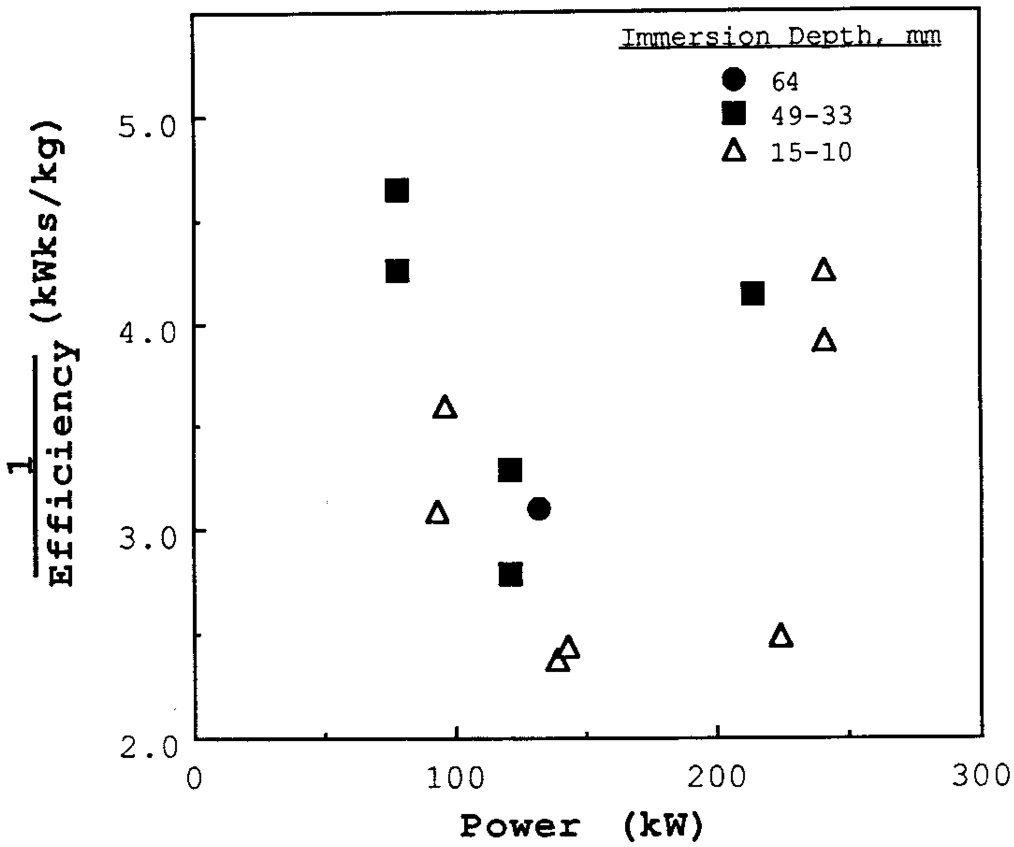

Figure 26. Relation between a power to melt rate ratio and power emphasizing changes in immersion depths.

of melts E24 and E26. The curve asymptotically approaching one suggests that increases in power resulted in the transference of a higher percentage of heat to melting of the electrode. Analysis of the three plots indicated that first, the power to melt rate ratio maintained a steady decrease, therefore melt efficiency increased as power increased. Second, none of the factors: immersion depth, slag cap thickness, or gap distance between the electrode and pool significantly affected the relation to efficiency. The efficiency of the system is a measure of the heat responsible for melting.

The distinct increase in melt rate with power shown in Figure 23 suggests that relatively more heat was consumed in heating the slag and melting the electrode as power increased. The efficiency data indicates that at higher power levels, the systems heat loss became less effective at reducing the amount of heat directed towards electrode melting, except in melts E24 and E26. This analysis assumed that an increased power was associated with an increase in the amount of heat generated by the slag.

The apparent deviation of melts E24 and E26 from the larger body of data presented in Figures 23-26 was investigated. Given the relatively high power input associated with melts E24 and E26, both had low melt rates resulting in a high power to melt rate ratio (indicating inefficient melting). Clearly, melts E24 and E26 experienced significant heat loss which caused a low electrode melt rate at a high value of power.

Table IV (on page 51) presented the average data for each melt, including the ratio of current travelling through the mold to the current travelling through the stool and base plate. During melting, current had two paths by which it traveled: 1) longitudinally from the electrode to the base plate, and 2) radially to the mold. The current ratio data in Table IV showed that melts E24 and E26 had over four times as much current traveling through the mold as through the stool. These data led to the observation that process parameters which increased the portion of current that travelled radially and returned through the mold, had a negative effect on the melt rate. This may simplistically be thought of as a change in the amount of power dissipated out the mold, but a more likely explanation was that the current partitioning changes reflected changes in thickness and tenacity of the slag skin. The slag skin data showed that no slag skin formed on melt E26, indicating metal to mold contact while melt E24 had 1.5 millimeters of slag skin present. Figure 6 presented a schematic drawing of the slag skin/pool interface. Because the slag skin acts as an electrical and thermal insulator, decreases in slag skin thickness or in skin tenacity, would result in increased current travelling to the mold. Similarly decreases in slag skin thickness and tenacity would result in increased heat transfer to the wall, leading to reduced power available for heating the slag and melting metal. Therefore the mold to stool current partitioning ratio can be characterized as an indicator of heat transfer variations.

4.1.2 Effect of Melt Rate and Power on Pool Profiles

Most investigators in the literature evaluated either pool volume or pool depth. This experiment characterized both parameters of pool volume and pool depth, under the assumption that changes in pool depth would not necessarily result in changes in pool volume. A number of factors can affect the levels of heat input and heat extraction during electroslag remelting. Alteration in heat flow characteristics was the underlying feature that determined pool profile (i.e. pool depth and volume). For a direct comparison with published data, pool depth was measured and related to melt rate as shown in Figure 27. Second, pool volume was measured from the experimental ingots and related to power as shown in Figure 28. As expected, the plots showed increased pool depth with melt rate and increased

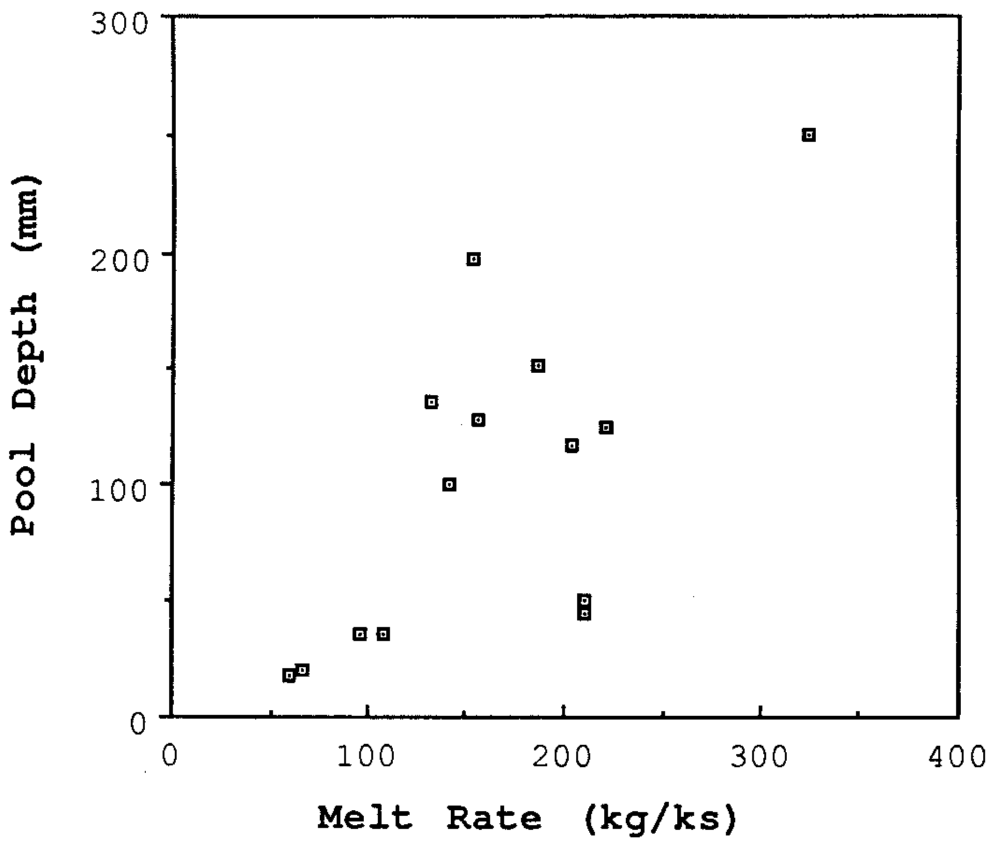

Figure 27. Relation between pool depth and melt rate for the experimental melts.

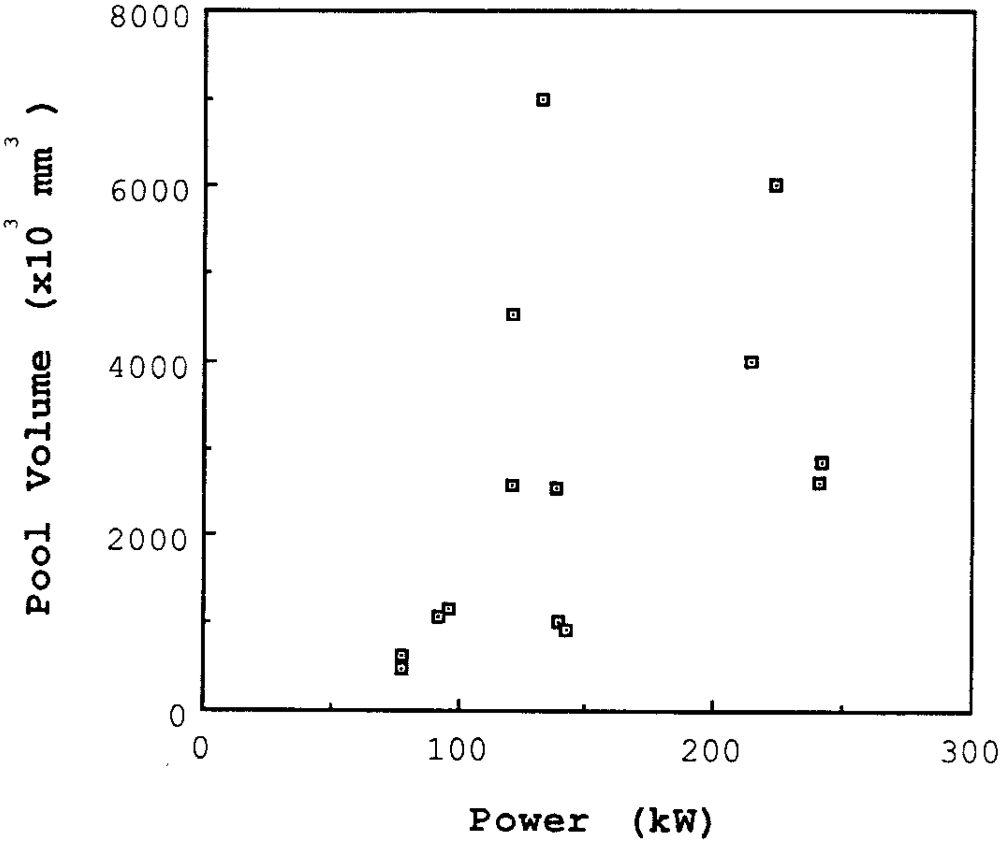

Figure 28. The relation between pool volume and power for the experimental melts.

pool volume with power. Neither plot shows the tightly correlated trends shown in the literature since large variations occurred in immersion depth, current, and slag cap thickness. Pool volume and depth were compared with power and characterized with respect to slag cap thickness, electrode to pool gap, immersion depth, and current.

Several investigators have evaluated or predicted the relationships between process parameters and melt pool geometry, usually focusing on pool depth as the melt pool descriptor. The model set forth by Mitchell and Ballantyne predicts a linear relation between melt rate and pool depth assuming constant slag cap thickness, immersion depth, and voltage. The experimental ingot data from this work agreed with the predicted pool depth and melt rate relationship. However, a well defined linear trend was not found because the other melt parameters were not held constant.

4.1.3 Pool Volume

4.1.3.1 Slag Cap Thickness Effects

Figure 29 shows pool volume plotted against power, with the slag cap thickness associated with each point indicated. Analysis of Figure 29 showed that the data points associated with a slag cap thickness between 86 millimeters and 137 millimeters were grouped apart from data associated with

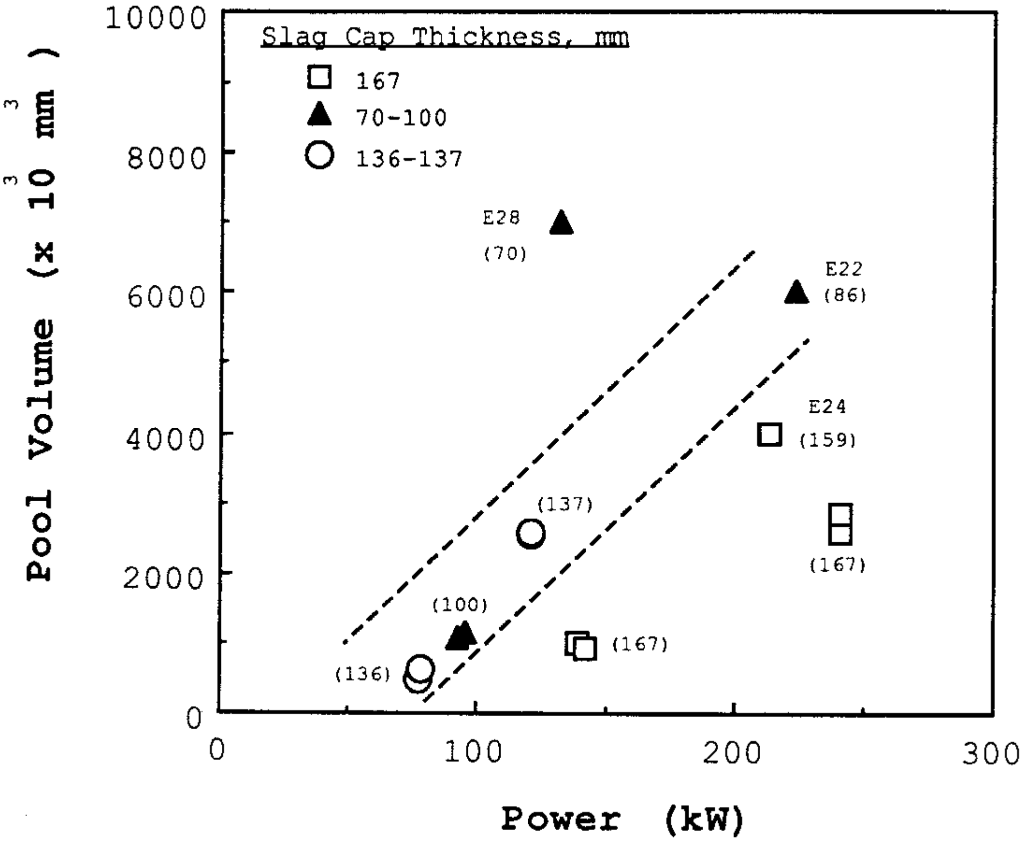

Figure 29. The relation between pool volume and power emphasizing variations in slag cap thickness.

thicknesses between 160 millimeters and 167 millimeters. The plot displayed two trends: 1) increased slag cap thickness during melting resulted in smaller pool volumes when comparing melts that had similar values of input power, and 2) pool volume increased as power increased when comparing melts with similar slag cap thickness. Since pool volume was directly related to melt rate, these results indicate that a larger slag cap will decrease the heat available for melting of the electrode. Melt E28, with a slag cap thickness of 70 millimeters, was set apart from the rest of the data but its small variation in cap thickness was not significant enough to justify the dramatic increase in pool volume.

4.1.3.2 Electrode to Pool Gap Effects

Figure 30 plots pool volume verses power with the electrode to pool gap values highlighted. The plot shows that variations in electrode to pool gap were able to differentiate the volume and power relationship. Comparison of melts that had similar amounts of power input, showed that pool volume decreased as the gap distance increased. For gap distances between 73 millimeters and 103 millimeters, the data indicated pool volume increased with increases in power. A separate volume versus power trend

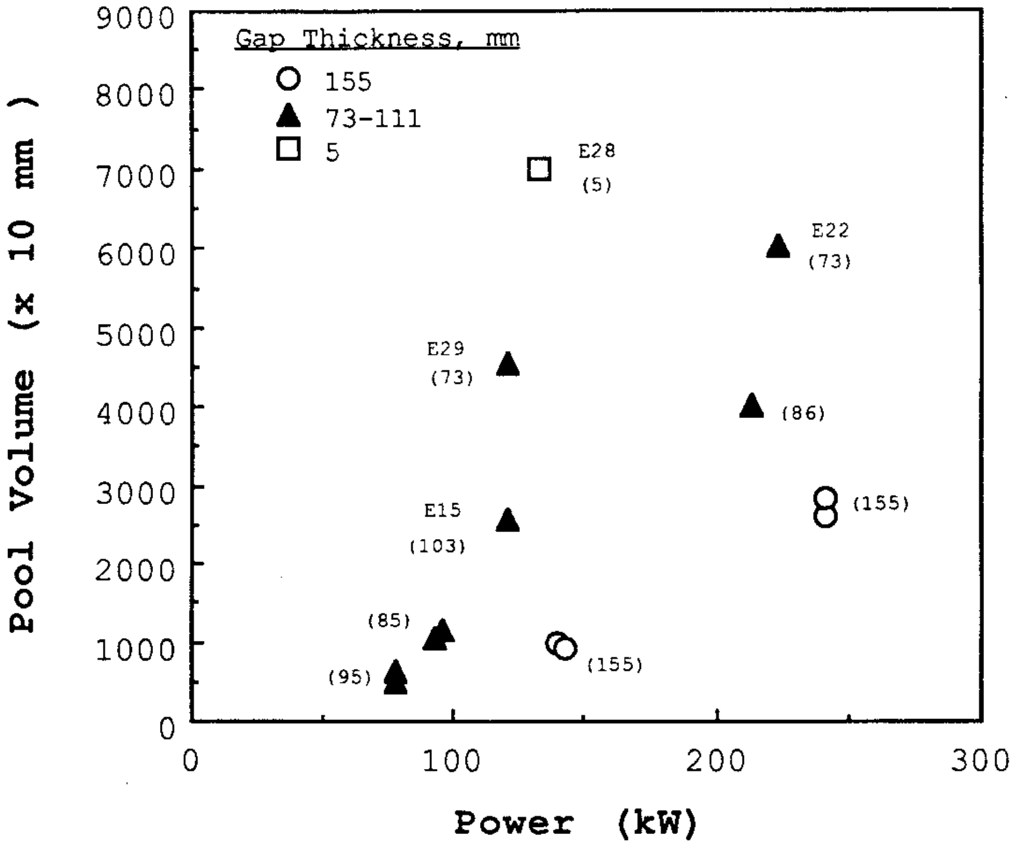

Figure 30. Relation between pool volume and power highlighting changes in electrode to pool gap distance.

was established for the gap distances of 155 millimeters.

Melts E26 and E27 both had relatively small pool volumes when compared with other melts close to them in power input. Both melts had gap distances of 155 millimeters and both had thick slag caps (168 to 170mm) and shallow immersion depths (11 to 14mm). On the other hand, melt E26 represented a high current melt (6.2kA) while melt E27 represented a low current melt (3.8kA). The fact that both melts had relatively small pool volumes for a given power value indicated that heat was lost more rapidly at large gap distances and thick slag caps.

The literature[37] indicated that the highest slag temperature results and the largest generation of heat occurs in the region of slag directly under the electrode tip. In addition, the highest loss of heat or extraction of heat by the cooling water occurs across the slag/mold interface. For the melt with the thick slag cap and shallow immersion depth, the electrode tip and the region of high heat generation were taken as far away from the pool as possible. This fact, combined with the fact that neither melt E26 or melt E27 had any slag skin formation, resulted in a significant transfer of heat across the slag/mold interface and the molten metal/mold interface. Note that the slag/mold interface between the electrode and pool was maximized by the shallow immersion and thick slag cap parameters. The combination of these factors decreased the electrode melt rate and subsequently decreased the pool depth of melts E26 and E27 with respect to melts of similar input power.

On the other end of the plot is melt E28. Melt E28 had a thin slag cap (69 millimeters) and a deep immersion depth (64 millimeters) resulting in a gap distance much smaller than that of the other melts (refer to Table IV). Melt E28 also formed a very thick slag skin (11 millimeters); hence, the insulating properties of the slag significantly decreased the extraction of heat across the slag/mold interface. This combination of deep immersion and thin slag cap placed the electrode tip close to the pool, which minimized the slag/mold interface between the electrode and pool. The close proximity of the electrode tip with the pool allowed for a high input of heat with greatly reduced heat loss; hence, a large molten pool volume resulted.

4.1.3.3 Effect of Current and Immersion Depth

The effect of current and immersion depth on the pool volume/power relationship are shown in Figures 31 and 32 respectively. Figure 31 shows, as could be expected, that the high current melts were concentrated in the high power

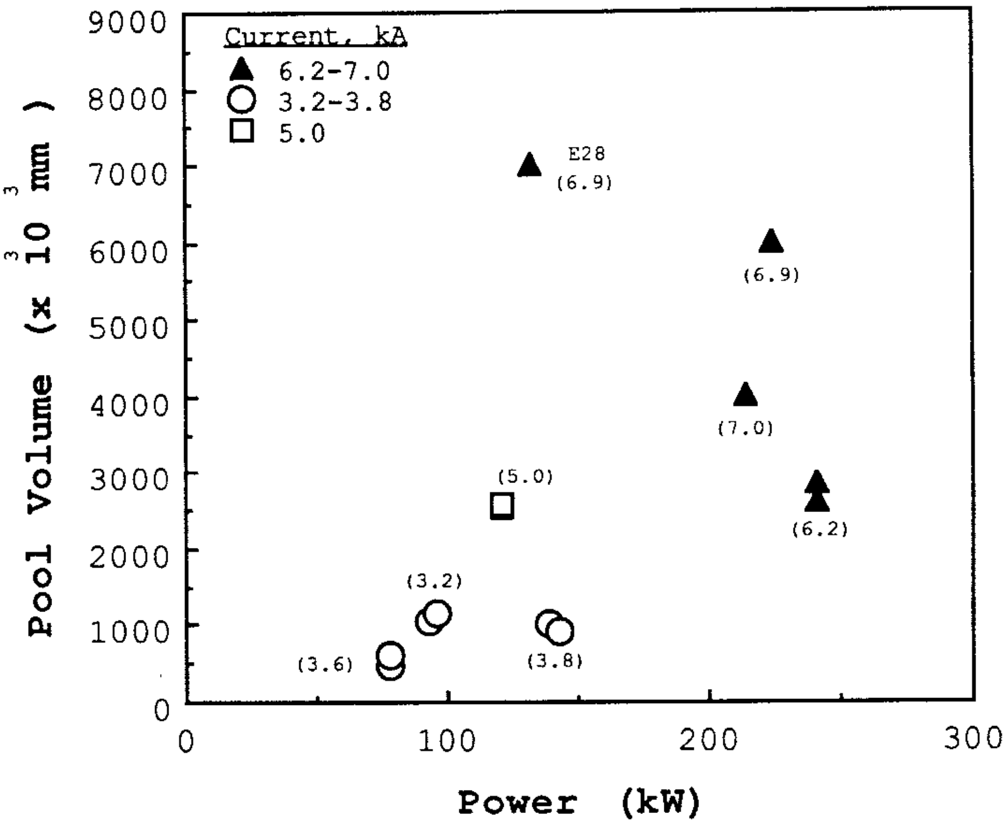

Figure 31. Relation between pool volume and power highlighting changes in melting current.

and high pool volume region of the graph. Although the data is well differentiated, decreased pool volume with increasing power at high current was not a very believable trend, especially since all other factors were not constant. This suggests that factors other than current were more instrumental in characterizing variations in pool volume. In the high power and high volume region of the plot, it was the slag cap thickness and the electrode to pool gap distance (more importantly, the gap distance) that deciphered where on the graph a particular high current melt fell.

Figure 32 illustrates the results of evaluating the volume to power relation data with respect to immersion depth. The immersion depth did not differentiate the data as distinctly as the gap distance (shown in Figure 30), but similar trends were obvious. For melts at similar power, increases in immersion depth (i.e. decreases in gap distance) increased the molten pool volume during melting.

In Figure 32, melts E22 and E24 make an interesting comparison. Even though melt E22 had a shallow immersion depth (13mm) compared with the deep immersion depth of melt E24 (48mm), melt E22 had a larger pool volume than E24. However, comparison of gap distances showed melt E22 to have a shallower gap distance (73mm) than melt E24 (112mm). In

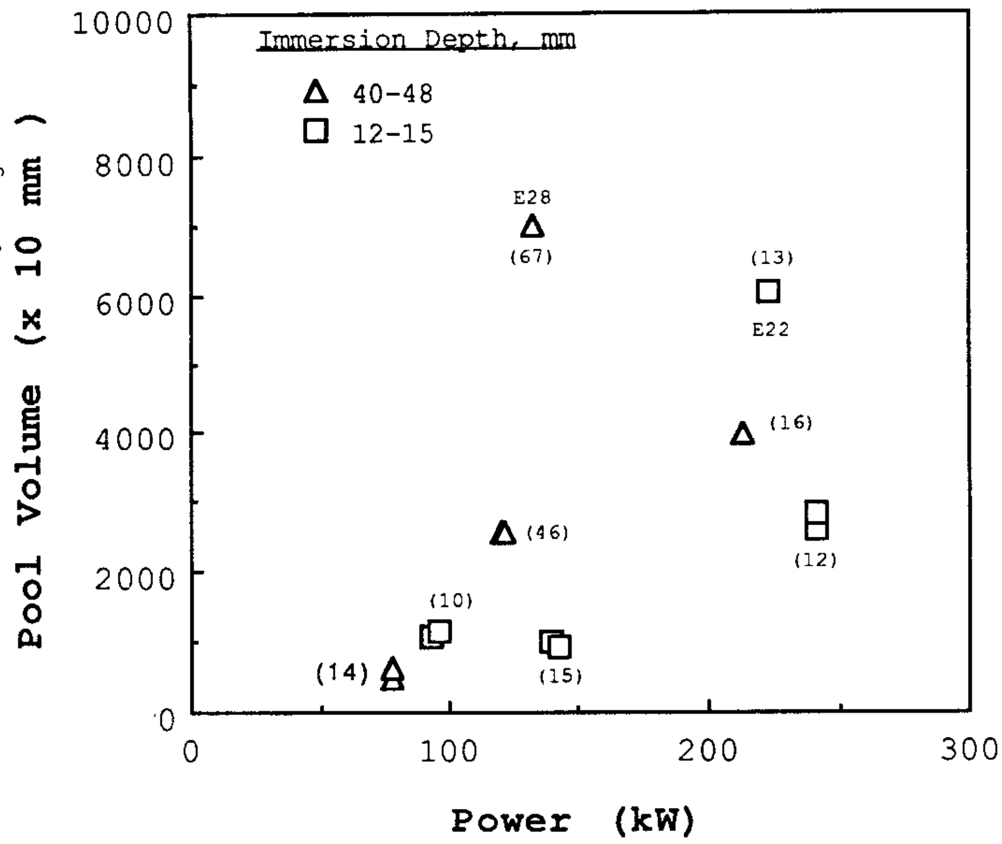

Figure 32. Relation between pool volume and power emphasizing the changes in immersion depth.

this case the slag skin thicknesses were close; 0.8 millimeters for E22 and 1.5 millimeters for melt E24. Both were high current melts close to 7.0 kiloamps. Melt E22 had a thinner slag cap (86 mm) than melt E24 (160 mm). The combination of an increased amount of slag to heat and a large heat generation region farther away from the pool resulted in a smaller pool volume in melt E24 than melt E22.

4.1.4 Pool Depth

4.1.4.1 Slag Cap Thickness Effects

Pool depth is plotted versus input power in Figure 33. A trend was observed which was similar to that seen with pool volume, Figure 29. An increase in pool depth was associated with an increase in power within ranges of slag cap thickness that were similar.

Figure 33 also illustrates that for melts with similar power input, the thicker slag cap melts produced shallower pools than those with moderate or thin slag caps. With respect to pool depth, melt E28 was grouped with the electrode to pool gap data between 73 millimeters and 112 millimeters.

4.1.4.2 Electrode/Ingot Gap Effects

The pool depth data was discriminated based on

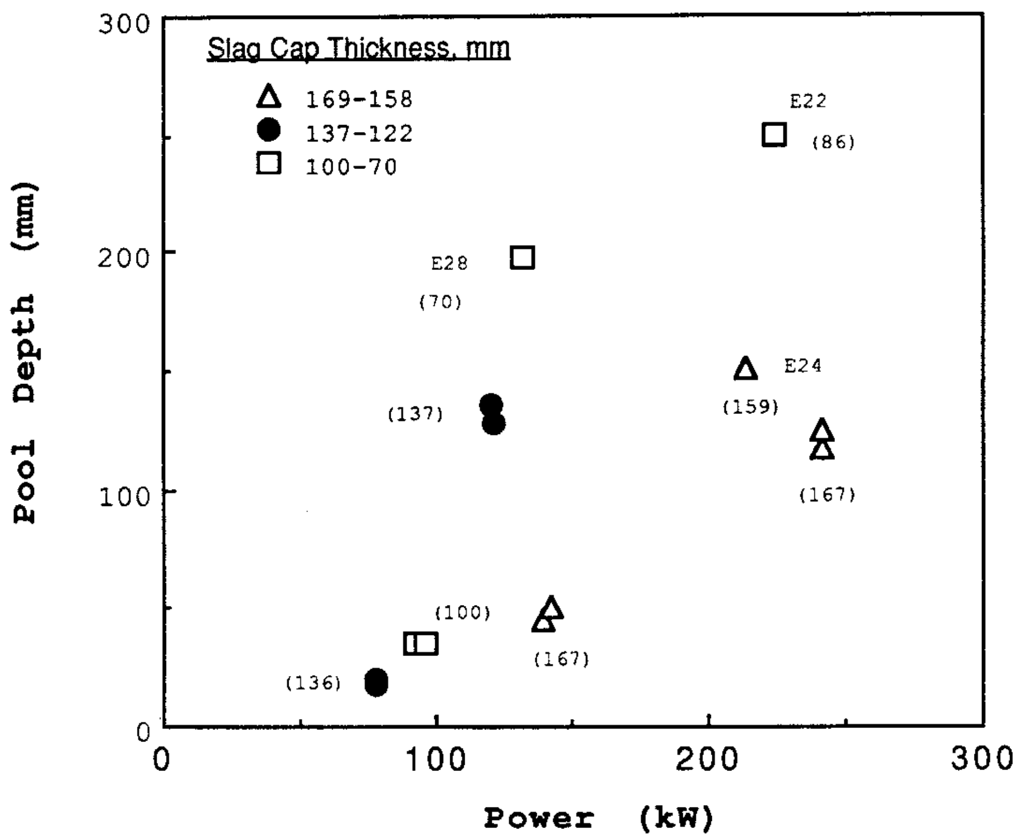

Figure 33. Relation between pool depth and power with emphasis on changes in slag cap thickness.

electrode to pool gap in Figure 34. Figure 34 shows the same trend of decreasing pool depth with increasing electrode to gap distance, as did pool volume data in Figure 30, for melts with similar values of input power. As in Figure 33, melt E28 was not set as distinctly apart from the rest of the data as it was when pool volume was evaluated. This suggests that the actual pool depth may not be as strong a function of the radial heat transfer (i.e. heat loss at the slag/mold interface) as is the pool volume. In other words, variations in radial heat loss affected pool shape or pool volume to a greater extent than depth of the pool.

4.1.4.3 Effect of Current

The effect of current on the pool depth and power relation was depicted in Figure 35. Again, the high current melts were concentrated in the high power and high depth region, while the low current melts were concentrated in the low power and low depth region. The high current melts were much more scattered than the low current melts because the gap distance for the high current melts varied between 5 millimeters and 155 millimeters while the gap varies between 85 millimeters and 154 millimeters for the low current melts.

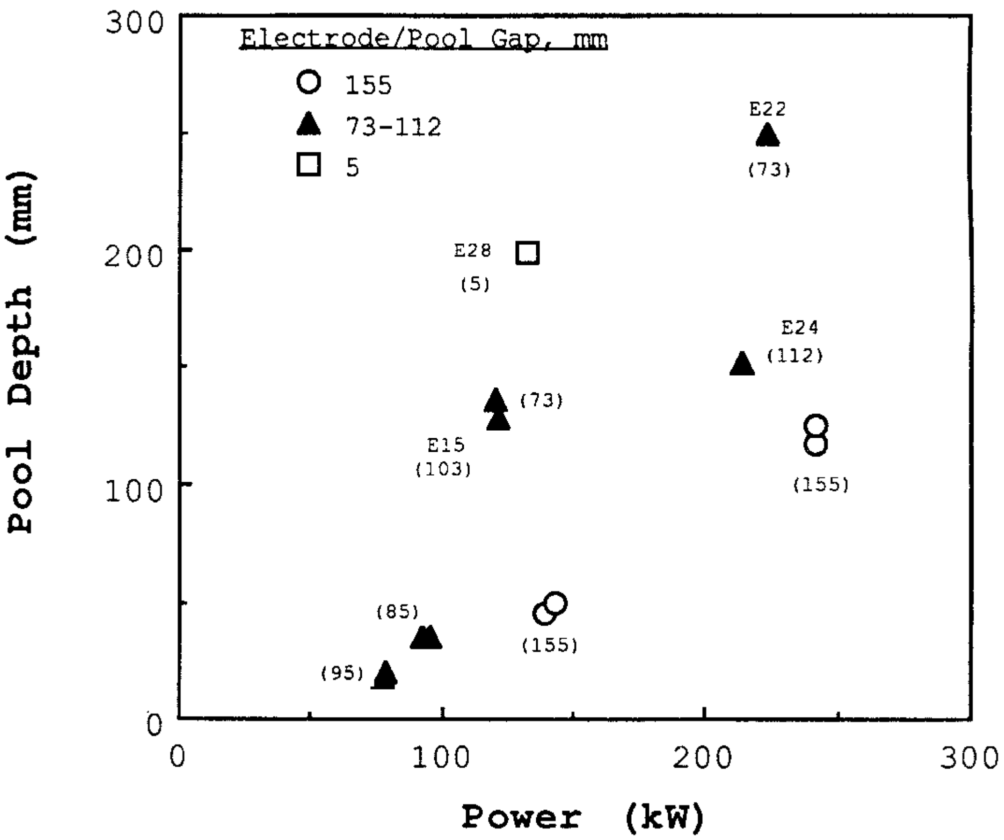

Figure 34. Relation between pool depth and power emphasizing variations in electrode to pool gap distance.

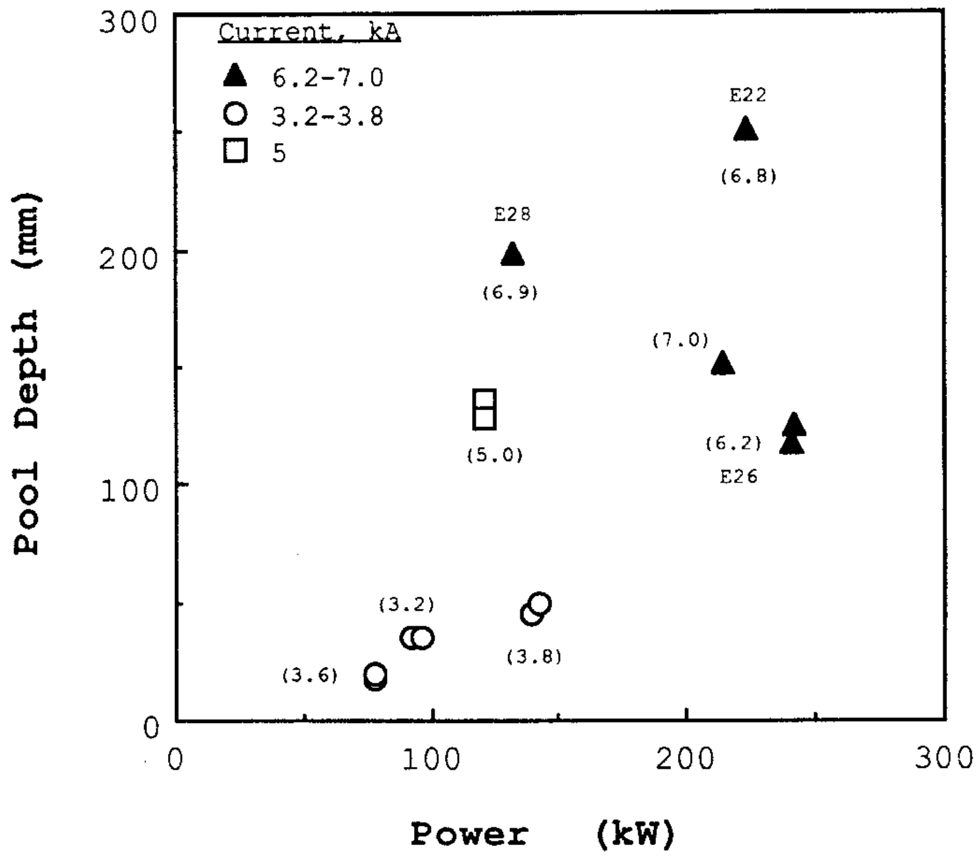

Figure 35. Relation between pool depth and power emphasizing variations in current.

4.1.5 Pool Shape

Characterization of both pool volume and pool depth allowed for the characterization of pool shape. As working end points for the sake of reference and comparison, two extremes of pool shape were assumed. The first extreme assumes that the entire liquidus isotherm is perpendicular to the direction of solidification (rectangular in shape). This is the case of perfectly longitudinal or plane front solidification. On the other end of the scale, deep pools may achieve a triangular profile or conical volume. This condition will result from a high current density in conjunction with an high percentage of heat loss across the ingot/mold interface[38].

The experimentally determined pool shape was compared with the theoretical end points. The shape parameter was represented by a depth to volume ratio. By plotting pool depth against pool volume for the experimental ingots, and comparing the data to the rectangle or triangle model, the geometry which most nearly approximates the pool shape can be determined. Further more, significant changes in pool shape will appear as a change in slope, easily detected by comparison to the model lines. Figure 36 shows the calculated pool volume for a range of pool depths, assuming a 254-mm-diam. ingot and given the reference end points of a

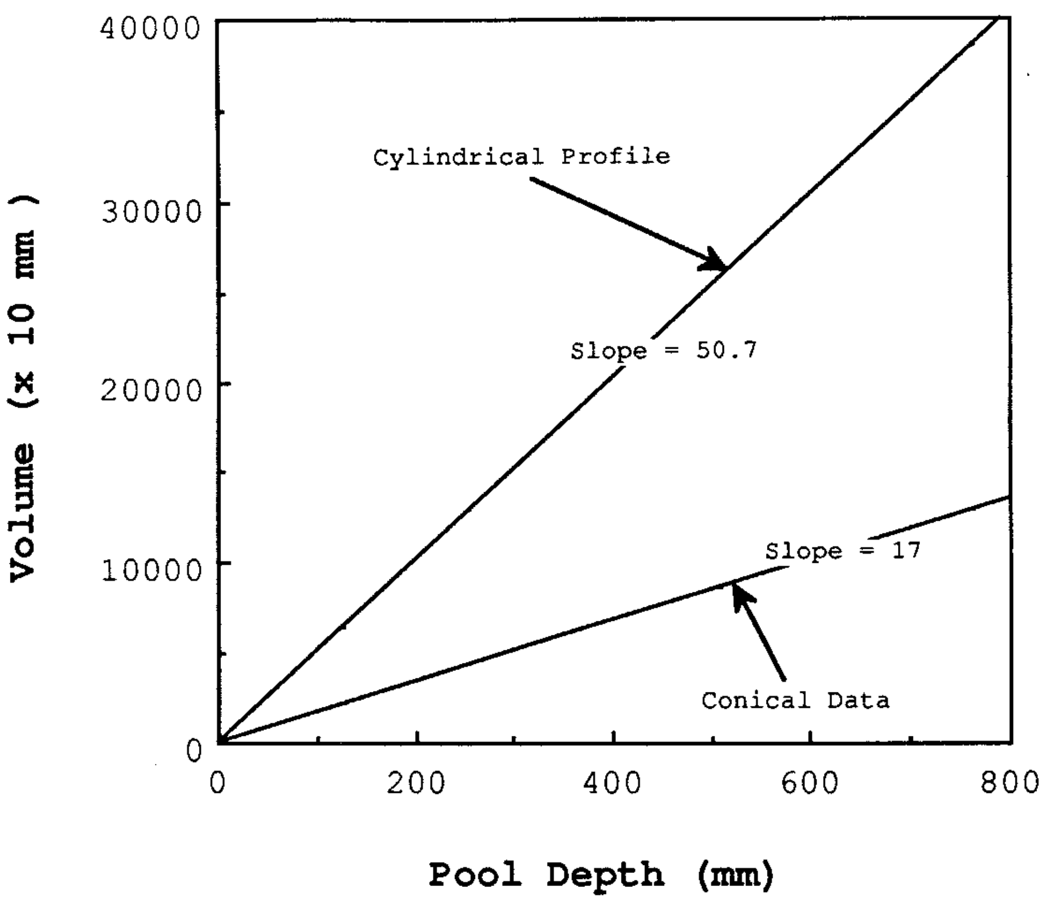

Figure 36. End point relations characterizing the extent to which pool shape can vary.

rectangular shaped (cylindrical volume), and a triangular shaped pool (conical volume).

The experimental melting resulted with ingots having a broad range of pool depths, between 35 millimeter and 250 millimeter. Figure 37 exhibits the experimental data compared with the model lines. The experimental points all fell between the two hypothetical end points. Excluding melt E28, the data can be approximated with a line whose slope is closer to the slope predicted by the conical data. Referring to the macrographs (shown in Figures 18, 19, and 20), the pool profiles are more triangular in nature. Figure 21b showed the macrograph of melt E28, which was the exception. The reduction in heat loss out the slag/mold interface due to the thick slag skin and the narrow gap distance, resulted in a more box-like pool.

4.1.6 Effect of Mold to Stool Current Ratio

The ratio of current traveling through the mold to that traveling through the stool varied widely for the experimental melts, shown in Table IV on page 51. The mold to stool ratio data was compared with several melt parameters. An increase in slag cap thickness was found to increase the amount of current travelling through the mold as indicated in Figure 38. The plot also shows that the

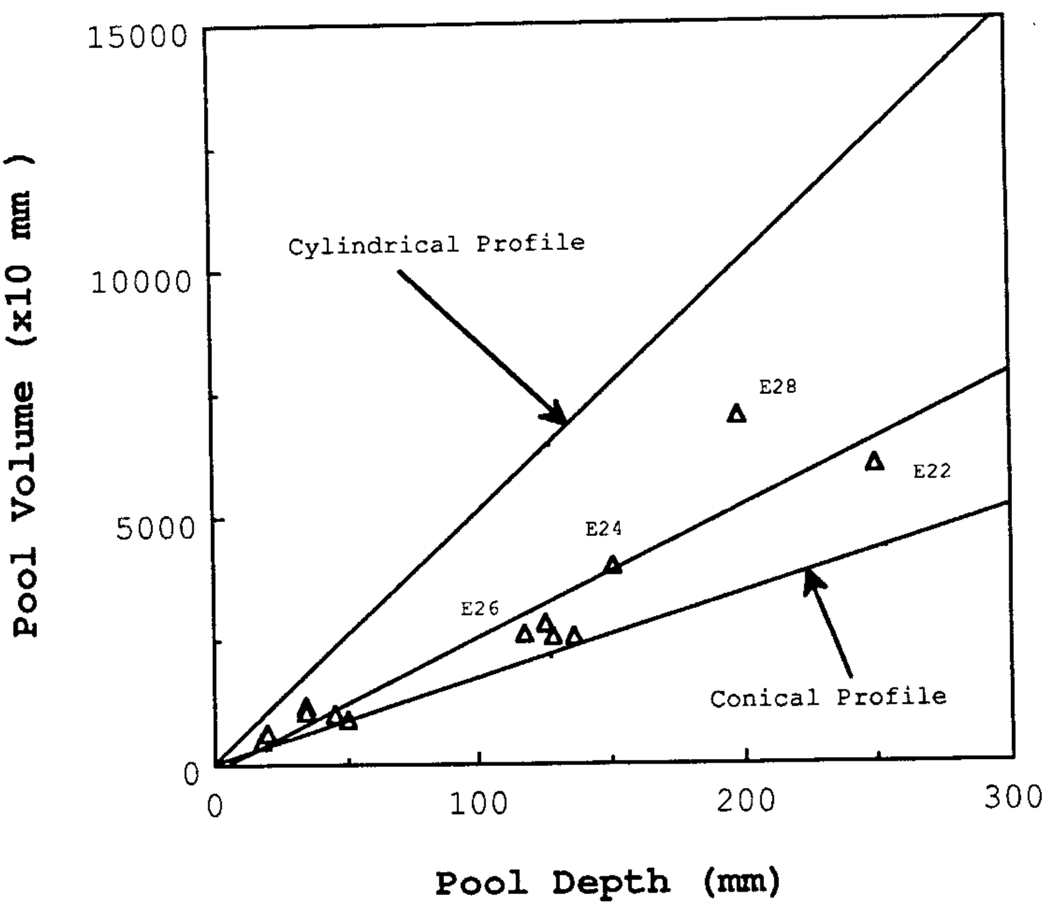

Figure 37. Comparison of pool depth to volume data from experimental melts, with end point relations.

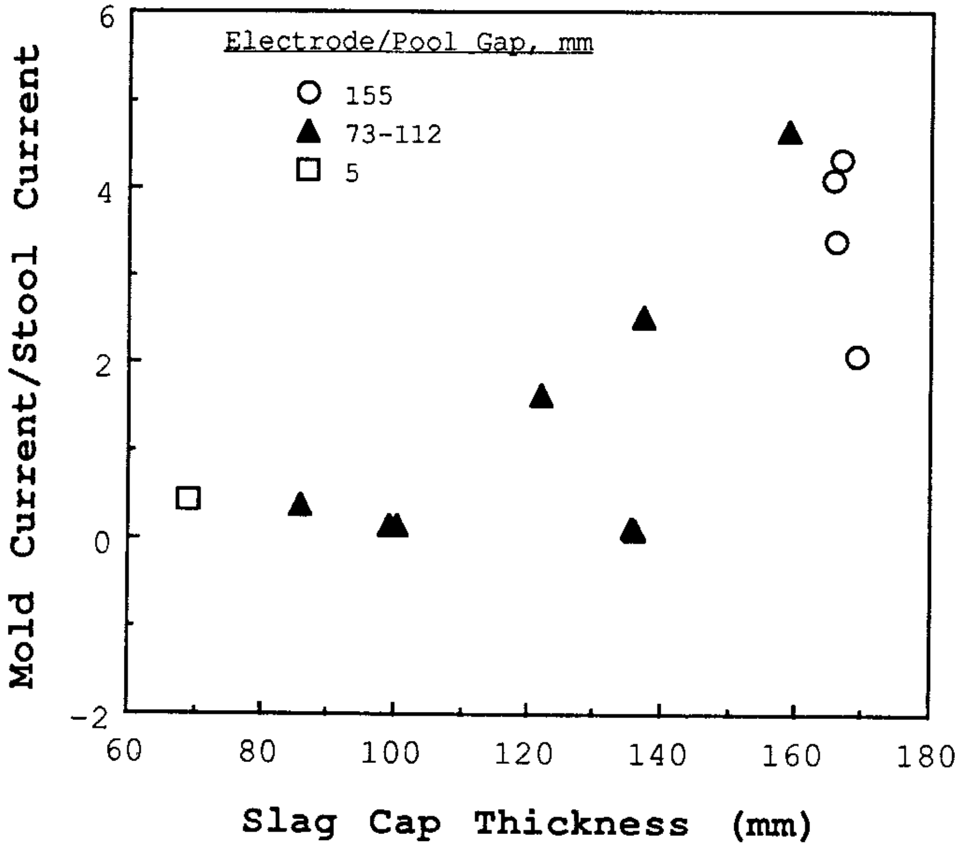

Figure 38. Relation between mold to stool ratio and slag cap thickness highlighting the electrode to ingot gap distance.

amount of current traveling through the mold was related to the electrode to pool gap distance, with larger gaps associated with a higher mold to stool ratio. It was observed in Figure 23 that the melt rate in melts E24 and E26, was inordinately low given the high power input. It was proposed that the high mold to stool ratio for melts E24 and E26, was responsible for the low efficiency. Figure 39 shows that this is not a general trend, but that in fact the data followed a trend where mold to stool ratio decreased with increasing power to melt rate ratio (i.e. decreasing efficiency), except for melts E24 and E26. This indicates that other factors were responsible for the inordinately low melt rate associated with melts E24 and E26.

4.1.7 Symmetry

Finally the degree of asymmetry of the molten pools was evaluated. This was performed by calculating pool volume based on both the right and left half pool areas, and defining the symmetry factor as the small volume divided by the large volume. The factor 1.0 represents a perfectly symmetric pool, while the extent of deviation from 1.0 indicates the relative degree of asymmetry.

The symmetry parameter was evaluated with respect to power with each of the following parameters highlighted:

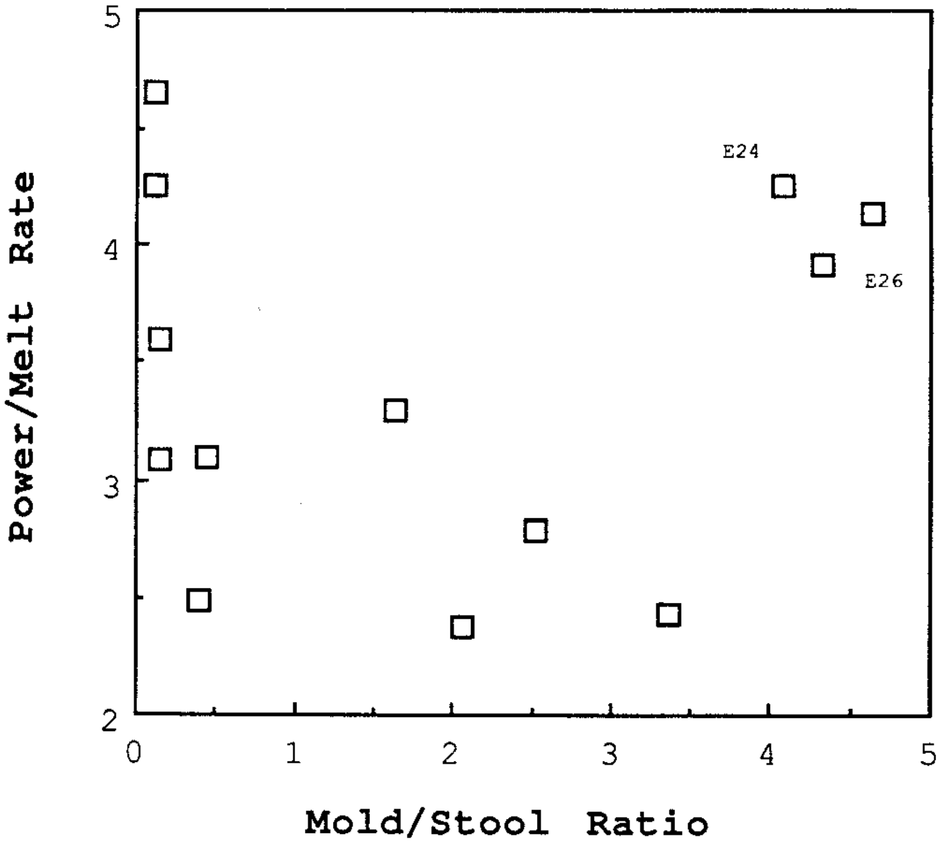

Figure 39. The relation between the power to melt rate ratio and the mold to stool current ratio.

current, immersion depth, running slag cap thickness, and electrode to ingot gap distance as depicted in Figures 40, 41, 42, and 43 respectively. In general, the pool asymmetry varied between 0.9 and 1.0 for the experimental melts with the exception of melts E15 and E26. Figure 40 shows that pool symmetry was relatively insensitive to input power. Melt E15 was processed prior to retrofitting of the crucible with a high velocity water guide. Consequently, melt E15 experienced nonuniform cooling (indicated by steam hammering) which occurred at various points in the crucible. Melt E26 also exhibited significant pool asymmetry. Melt E26 was the only high current/high melt rate ingot that failed to form an insulating slag skin on the ingot. The unimpeded flow of heat to the cooling water at the high melt rate (222-kg/ks) may have resulted in boiling in portions of the cooling tract; hence, the nonuniform cooling.

Figure 41 suggests that melts with deep immersion depths may have produced pools slightly more asymmetrical than the pools of the shallow immersion melts. This observed relation may have been an artifact since evaluation of Figure 43, which emphasized variations in the electrode to ingot gap distance, showed no similar relation to Figure 41. It would be expected that any trends predicted through varying the immersion depth would inevitably be supported by

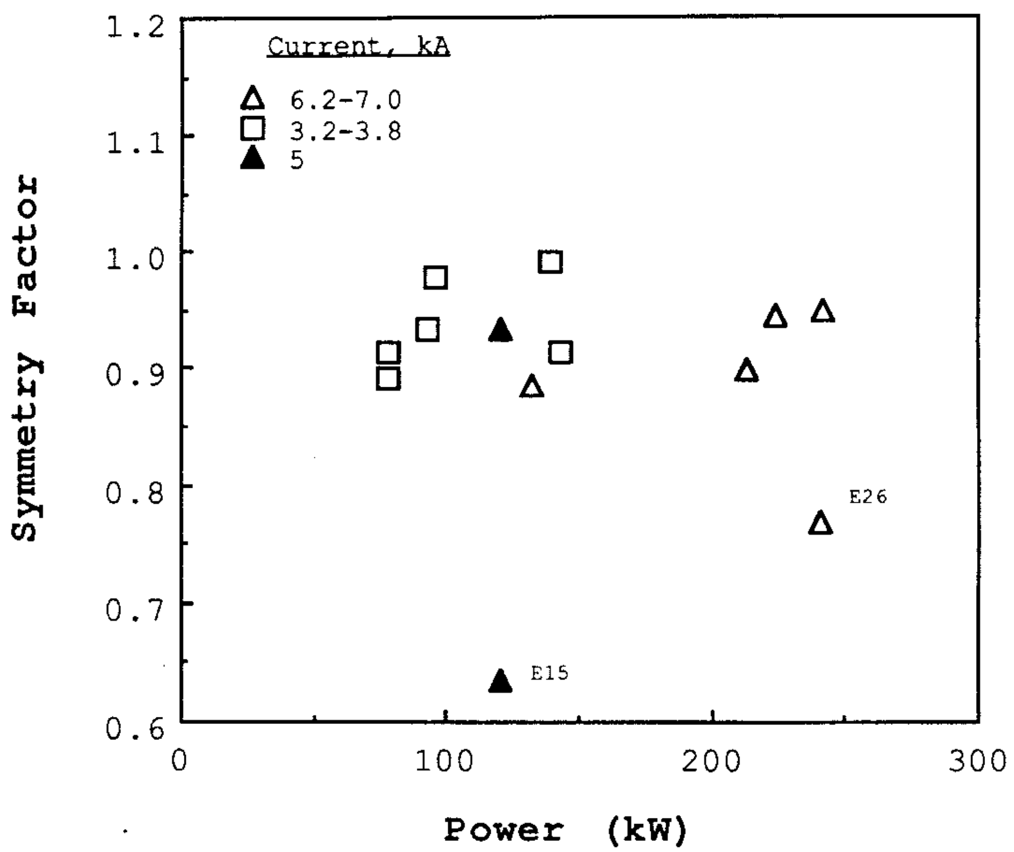

Figure 40. Relation between pool symmetry and power with emphasis on changes in current.

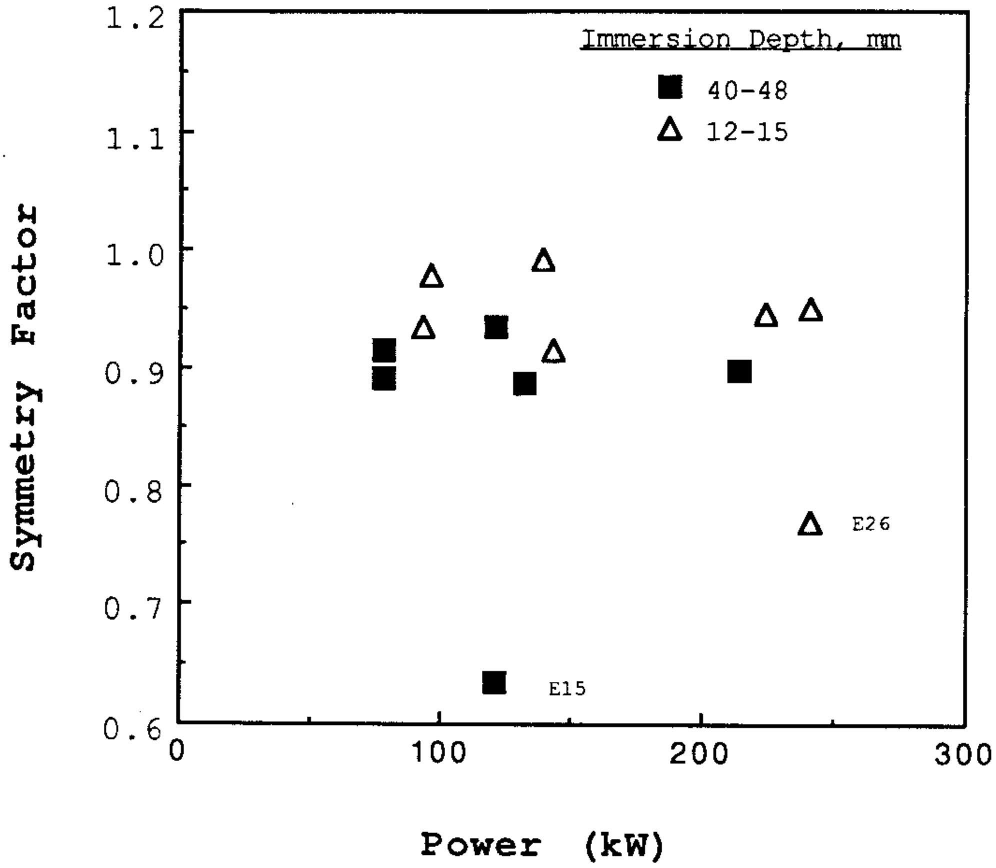

Figure 41. Relation between pool symmetry and the power with emphasis on changes in immersion depth.

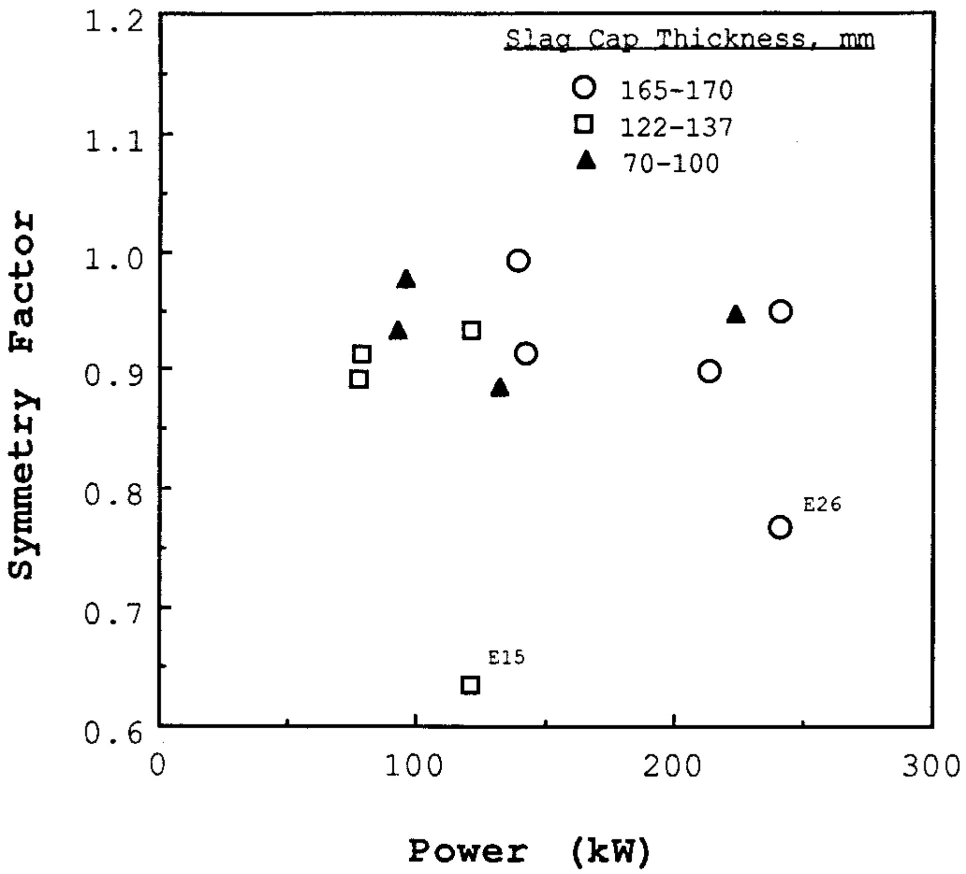

Figure 42. Relation between pool symmetry and power with emphasis on changes in slag cap thickness.

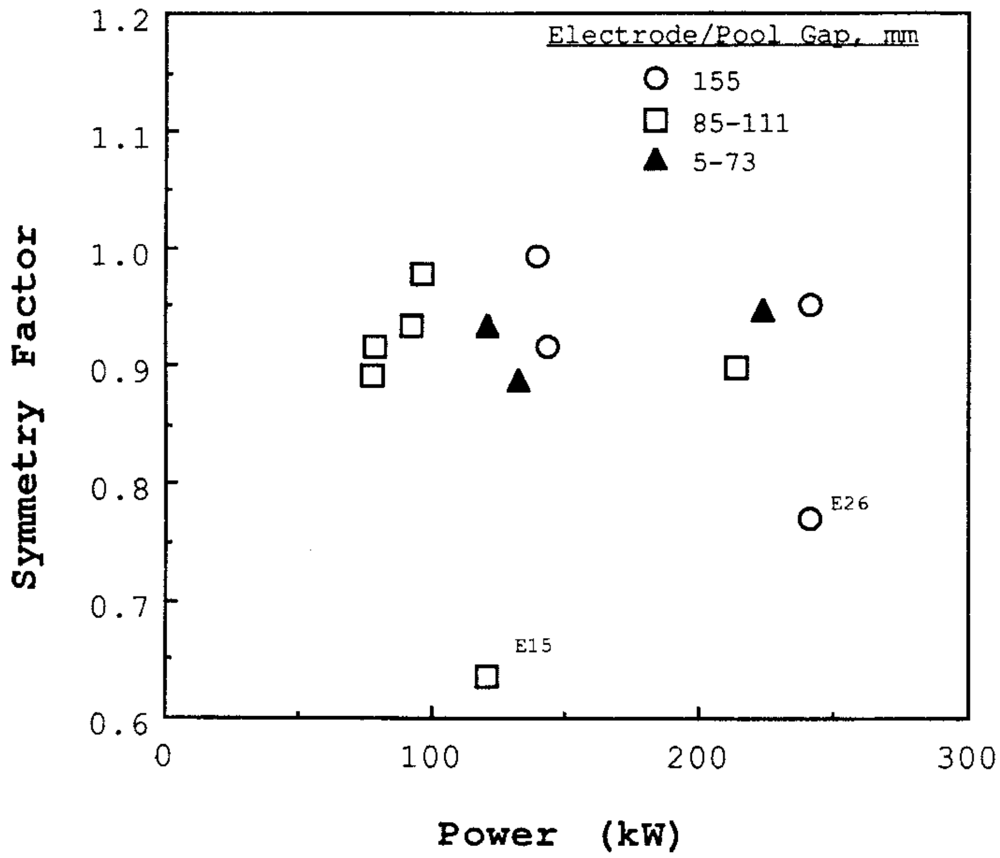

Figure 43. Relation between pool symmetry and power with emphasis on the changes in electrode to pool gap distance.

trends established by evaluating gap distance data.

4.2 LOCAL SOLIDIFICATION TIME ANALYSIS

The determination and characterization of the local solidification time (i.e. time for the metal to travel from the liquidus isotherm to the solidus isotherm) is important when considering solidification. It has been shown that variations in local solidification time bring about variations in both the structure of carbide precipitation[19] and the degree of elemental partitioning that may occur. Although a number of publications have analyzed variations in local solidification time, the effect of melting parameters has not been well documented.

Lack of Alloy 625 directional solidification data, required that a method be developed to predict or calculate local solidification times. The literature has indicated that local solidification time can be predicted through the evaluation of primary or secondary dendrite arm spacing. Researchers have performed numerous studies over a wide range of alloys, in which local solidification time was related to dendrite arm spacing. In most cases, an exponential relationship exists between local solidification time and dendrite arm spacing:

$$d = (A\theta)^n \tag{1}$$

where d represents the secondary dendrite arm spacing in micrometers (μm) and θ represents the local solidification time in seconds. The variables A and n are both empirical constants which depend on the material. Local solidification time and dendrite arm spacing are both functions of the solute diffusion rate. Howarth and Mondolfo[23] theorized, assuming an exponential decay of the concentration gradient in the liquid immediately adjacent to the dendrite, that changes in cooling rate causes changes in the composition gradient and the rate of diffusion, resulting in changes in the dendrite arm spacing. As cooling rates decrease, the spacing increases but the difference in spacing at varying compositions becomes more pronounced hence, the straight lines in a logarithmic plot.

The local solidification times presented in Table V (on page 52) were calculated from the following relation.

$$d = (5.21\ \theta)^{0.49} \tag{2}$$

This equation resulted from comparing measured ingot secondary dendrite arm spacings with the local solidification times calculated from the model developed by Ballantyne[11]. The measured and calculated data were plotted on a log-log plot shown in Figure 44; equation (2) represented the linear approximation of Alloy 625 data. The equation determined for Alloy 625 compared favorably with

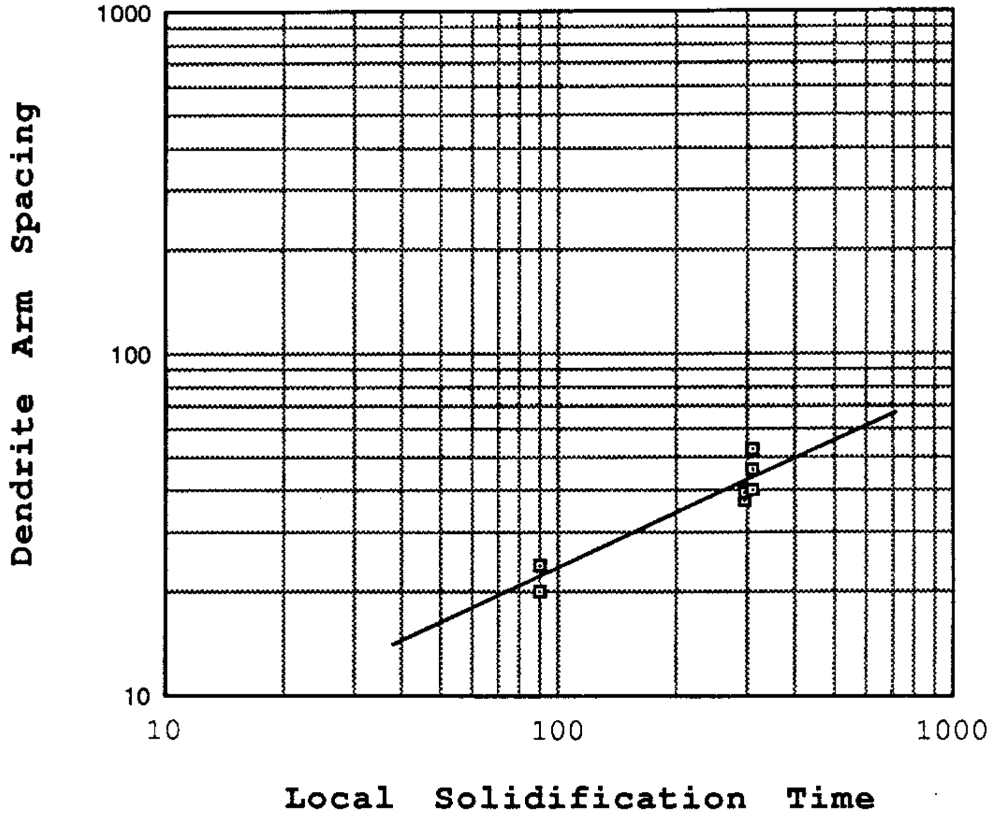

Figure 44. Plot of the calculated local solidification times with measured secondary dendrite arm spacings.

other equations used for different materials to correlate local solidification time and dendrite arm spacing.

Use of the model, to calculate local solidification times, was confined to actual ingot pool profiles that compared favorably with the pool profiles predicted by the model[11] (agreement within 20 to 30 mm). Agreement between actual and predicted pools occurred in only three ingots; melts E15, E27, and E29. This method for determining the dendrite arm spacing and local solidification time relation does not have the accuracy associated with performing directional solidification experiments, but for this work the relative values were beneficial.

4.2.1 Effect of Parameters on LST

The local solidification time was shown to be a function of the radial distance from the centerline, as shown in Figure 45. Figure 45, as was expected, showed a dramatic increase in cooling rate (decrease in local solidification time) as one moved from the center of the ingot to the edge. The high cooling rate at the edge resulted from thermal gradients associated with the relative closeness of the mold cooling water.

Figure 45 also highlights variations in power input, and shows that melts, E25 and E23, with the lowest power

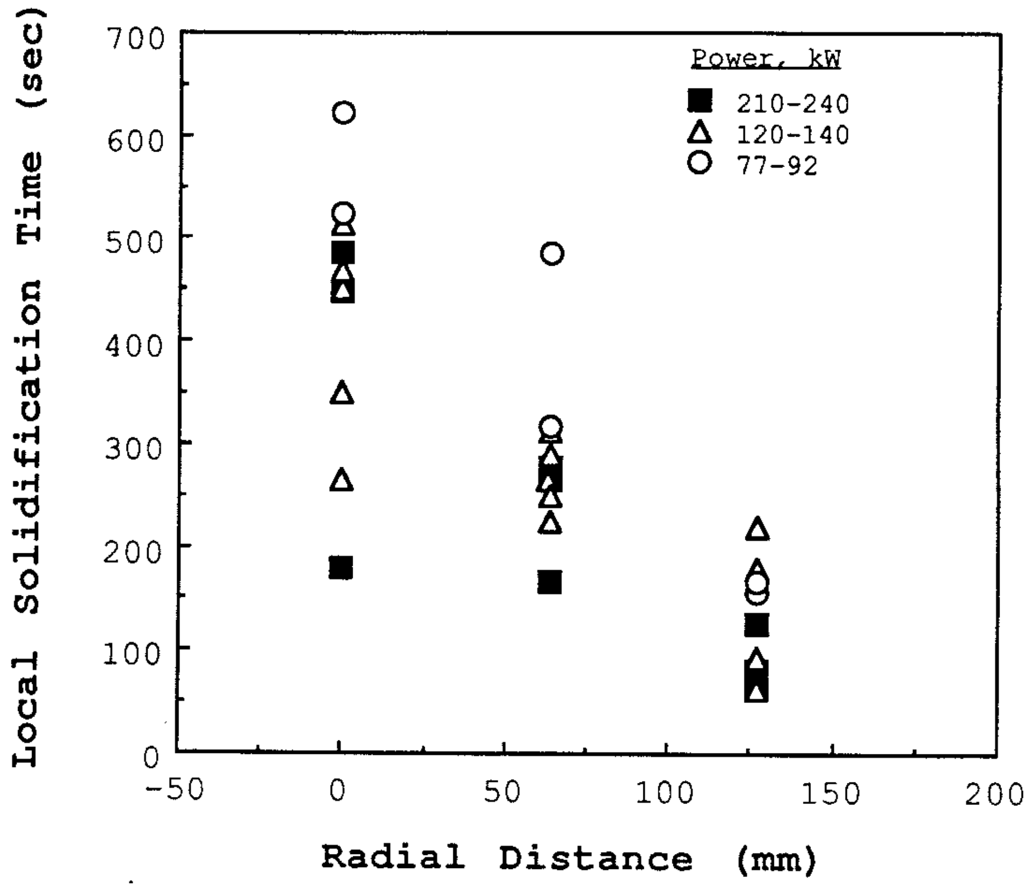

Figure 45. Variation in local solidification time with radial distance from the ingot centerline. Changes in power input was emphasized.

input (77 to 92 kW respectively) have the highest centerline local solidification time values. This corresponded with a coarse dendrite structure, which indicated a slow cooling rate. Other than for melts E25 and E23, no clear relationship was seen between local solidification time and input power.

Local solidification time is plotted against radial distance from the center of the ingot in Figure 46. This particular figure also indicates the pool depth values for each data point. The plot shows no significant correlation between local solidification time and pool depth. Note that melts E25 and E23, in addition to having the highest local solidification time, had the shallowest pool depth.

Another parameter associated with local solidification time is the rate of advance of the solidification front. Alexander and Rhines[26] correlated dendrite arm spacing directly to the solidification front advance rate in static castings. Given the relation between local solidification time and dendrite arm spacing, in theory, a correlation should exist between the local solidification time and the advance rate of the solidification front.

For this experiment, the growth rate was calculated based on the melt rate and used to approximate the solidification front advance rate. Figure 46 shows

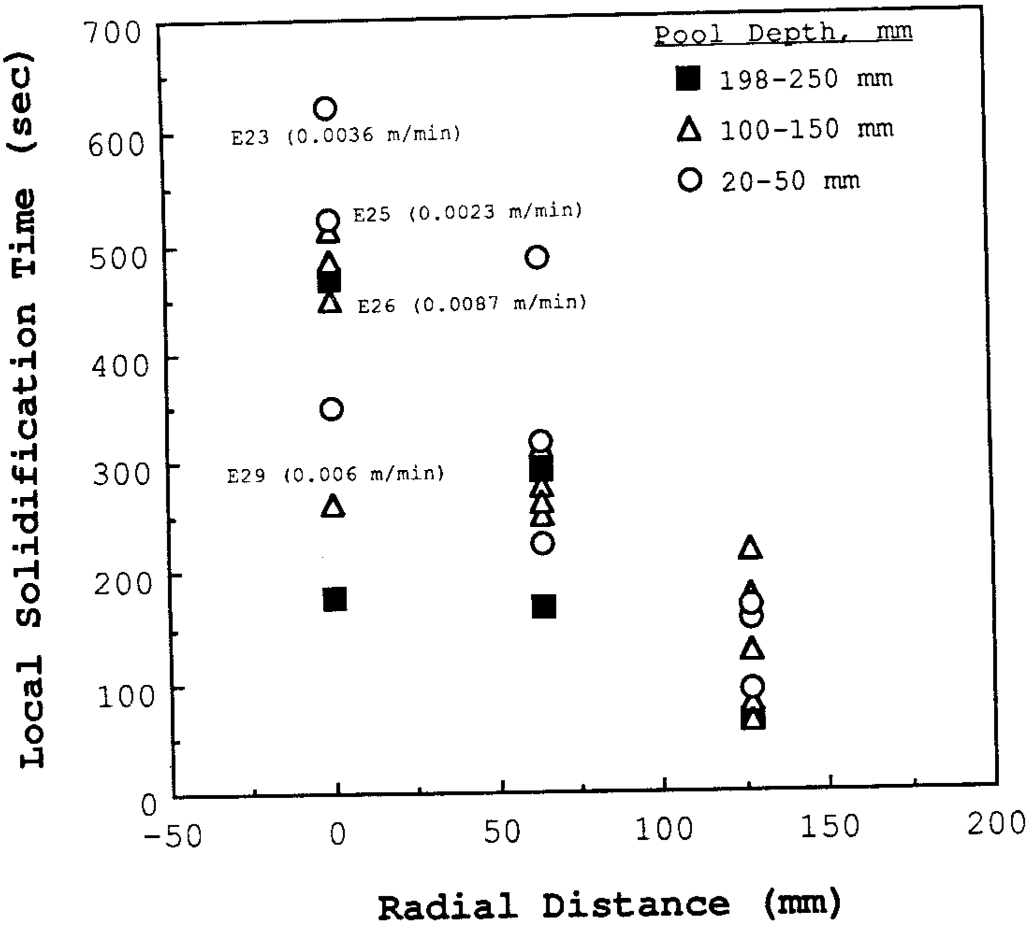

Figure 46. Relation between local solidification time and radial distance from the centerline, emphasizing changes in pool depth.

calculated ingot growth rates for melts E23 and E25, both of which had high centerline local solidification times (~600-sec). An ingot growth rate was also calculated for melt E29, which represented a melt with a low centerline local solidification time (~300-sec), and for melt E26 which exhibited the highest melt rate. Comparison of these points indicated that no correlation could be made between LST and ingot growth rate for this ESR experiment.

Evaluation of the data shown in Figures 45 and 46 indicated that the local solidification time was not a function of the power input or pool depth. The observed variation in local solidification time between the center and edge of the ingot indicated that the local solidification time was a function of the rate at which heat was extracted from the ingot.

Further analysis of the local solidification time, made with respect to slag cap thickness and electrode to pool distance, is presented in Figures 47 and 48. These figures showed that no trend existed between either of the parameters and local solidification time. It has been determined that changes in these parameters (slag cap thickness and the distance between the electrode and pool) have the ability to alter the ingot pool profile. It has been postulated that variations in these parameters affects

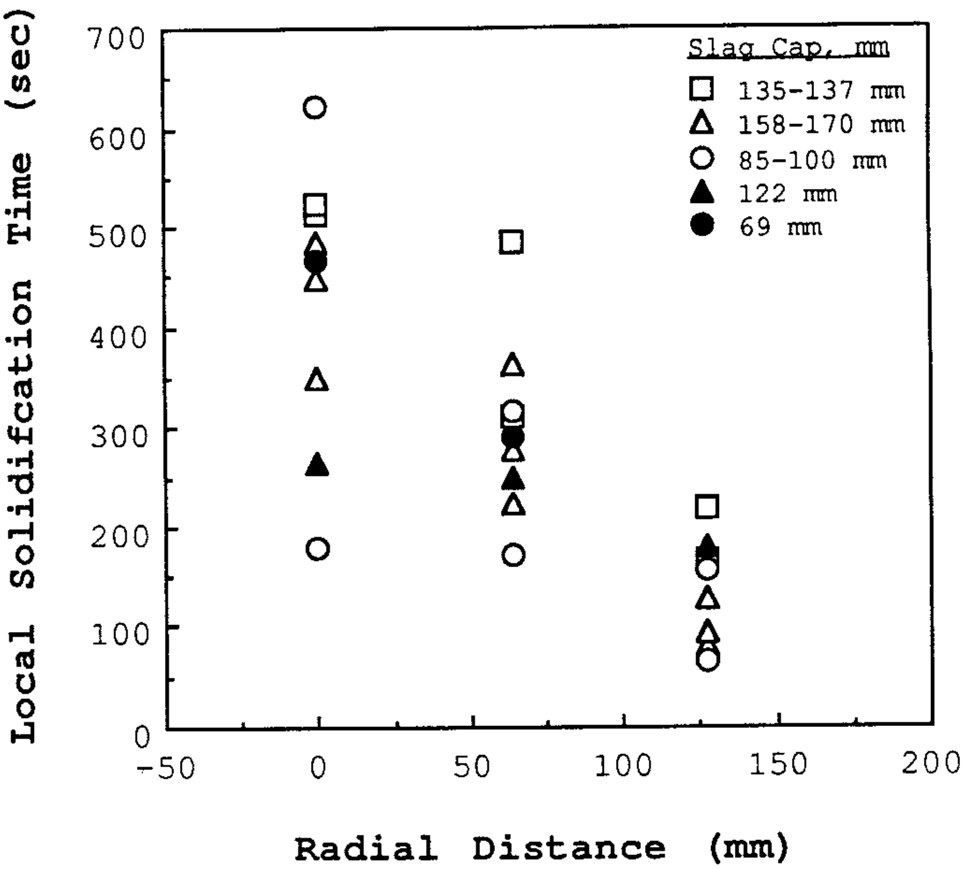

Figure 47. Variation in local solidification with changing distance from the centerline, emphasizing changes in slag cap thickness.

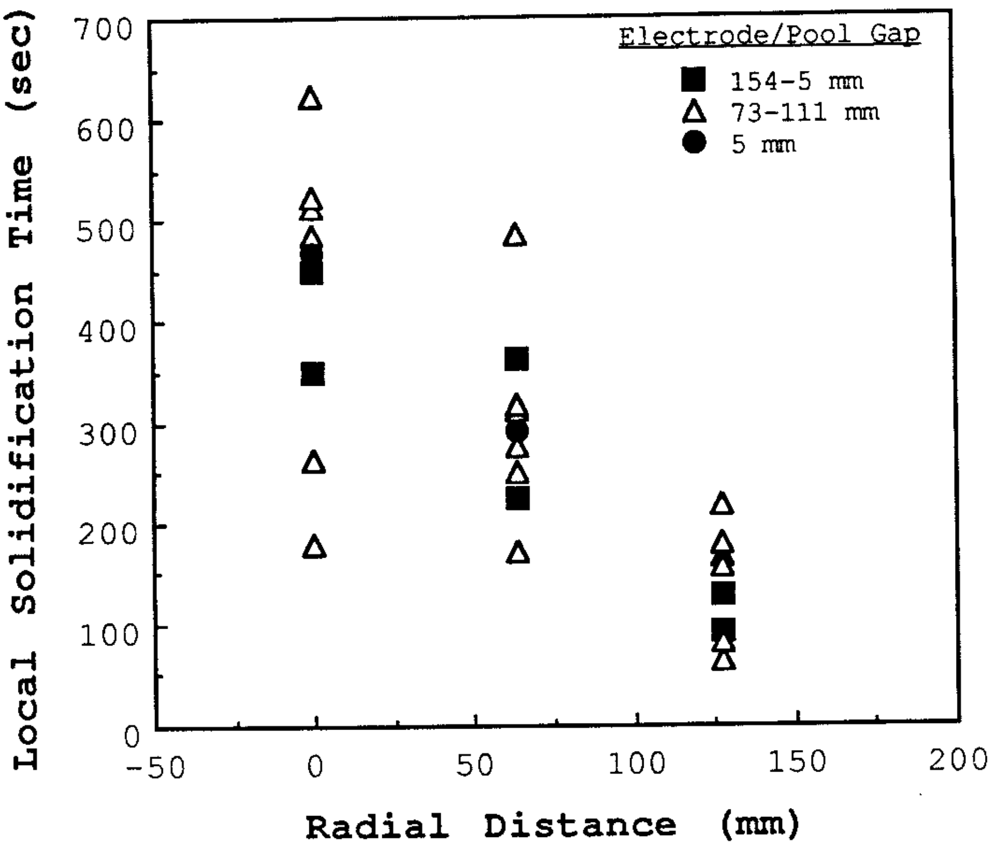

Figure 48. Relation between local solidification time and the radial distance from the center of the ingot, emphasizing changes in gap distance.

heat distribution in the slag. If changes in slag cap thickness or immersion depth primarily affected the thermal characteristics of the slag, and if local solidification time was primarily controlled by the amount of heat extracted by the cooling water at the ingot/mold interface, then changes in slag cap thickness or immersion depth would not directly affect ingot local solidification times. Shved[22] determined, for remelting processes, that the cooling rate and the rate of advance of the solidification front are independent of one another. His data on vacuum arc remelting showed that a decrease in melting current resulted in a coarsening of the ingot structure and an increase in the local solidification time.

4.3 MACROSEGREGATION ANALYSIS

The degree of chemical homogeneity resulting from a remelting process is an important consideration with respect to ingot quality and the quality of the forged product. In nickel-based superalloys, the addition of niobium causes an increase in the alloy strength by solid solution strengthening. Molybdenum is another element which solid solution strengthens Alloy 625. Therefore, significant variations in either the niobium content or the molybdenum content over the cross section of an ingot would vary the strength properties of the alloy. Flemings[28] observed that during solidification, large ingots are susceptible to positive and negative segregation at the centerline or edge.

Macrosegregation during remelting of superalloys is often thought to result from density driven flow in the liquid-solid region during solidification[28]. To qualitatively evaluate the effects of the process parameters on macrosegregation, two ingots with widely different pool shapes were chosen for composition mapping. Melts E28 and E27, with pool depths of 198 mm and 50 mm respectively.

Figures 49 and 50 represent the niobium and nickel composition maps from a section of slice E28-2. The results of melt E28 showed varying concentrations of both nickel and niobium at the centerline of the ingot. Of the elements analyzed, nickel and niobium exhibited the greatest tendency to segregate during solidification of melt E28. The results from melt E27, showed that no segregation was detected for any of the five elements studied. The nickel and niobium maps of melt E27 are presented in Figures 51 and 52 respectively.

It has been determined in the literature[8] that during dendritic solidification, niobium segregates to the interdendritic region while nickel preferentially remains in the dendrite core. The evidence of a lower nickel content

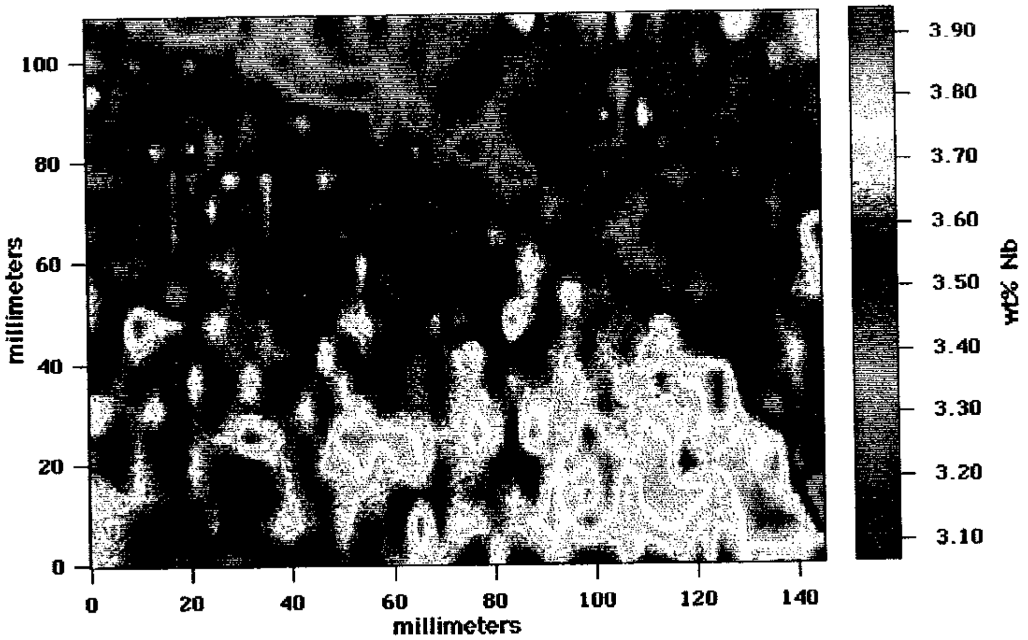

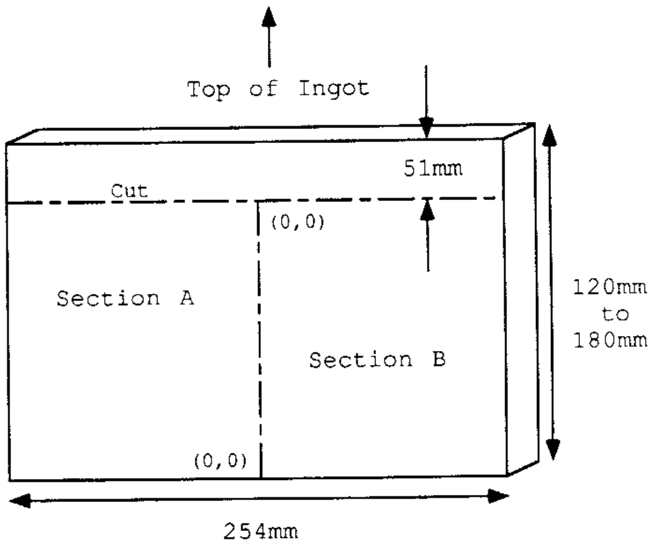

Figure 49. Niobium map of a section of slice E28-2B.

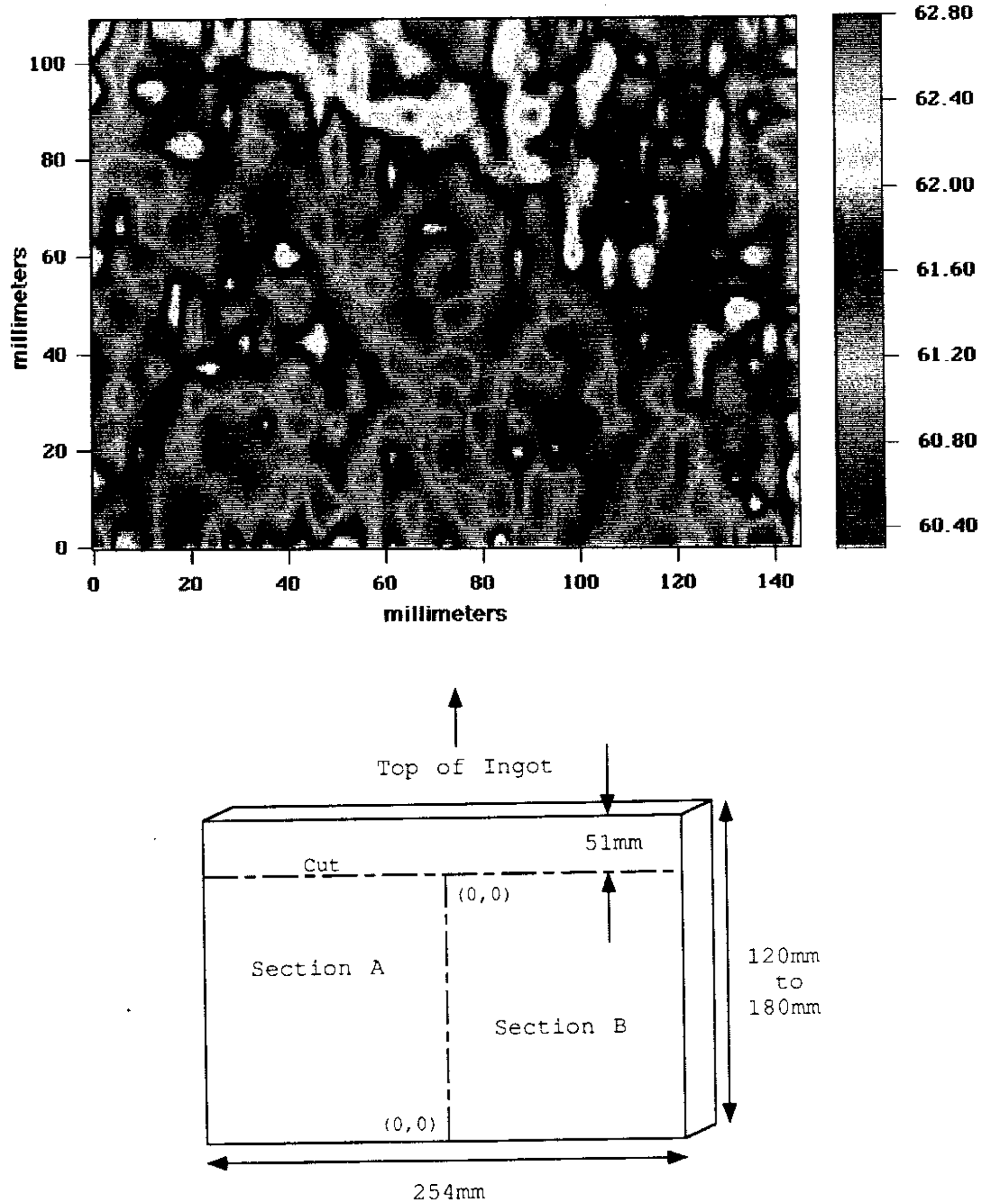

Figure 50. Nickel map from a section of slice E28-2B.

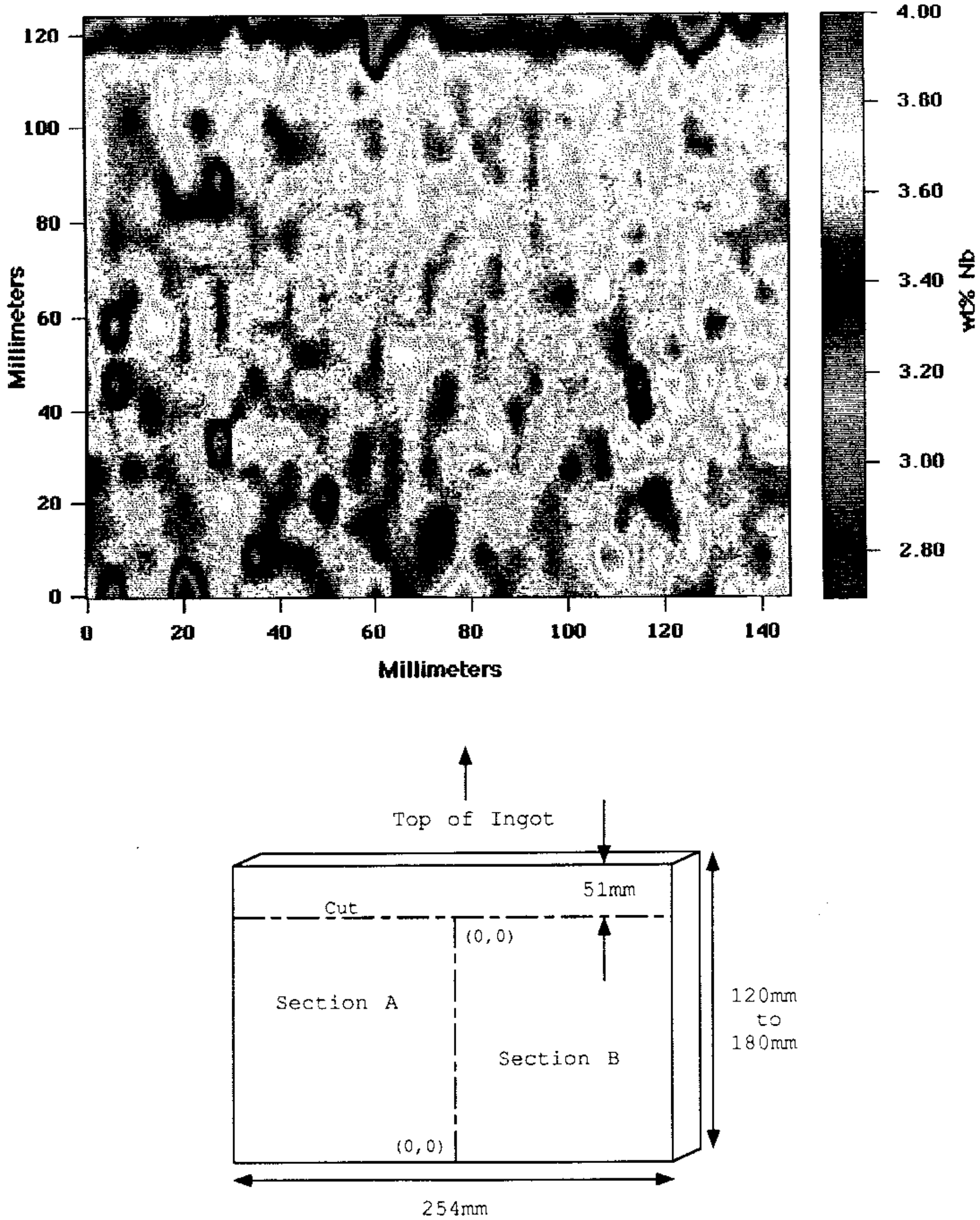

Figure 51. Niobium map from a section of slice E27-2A.

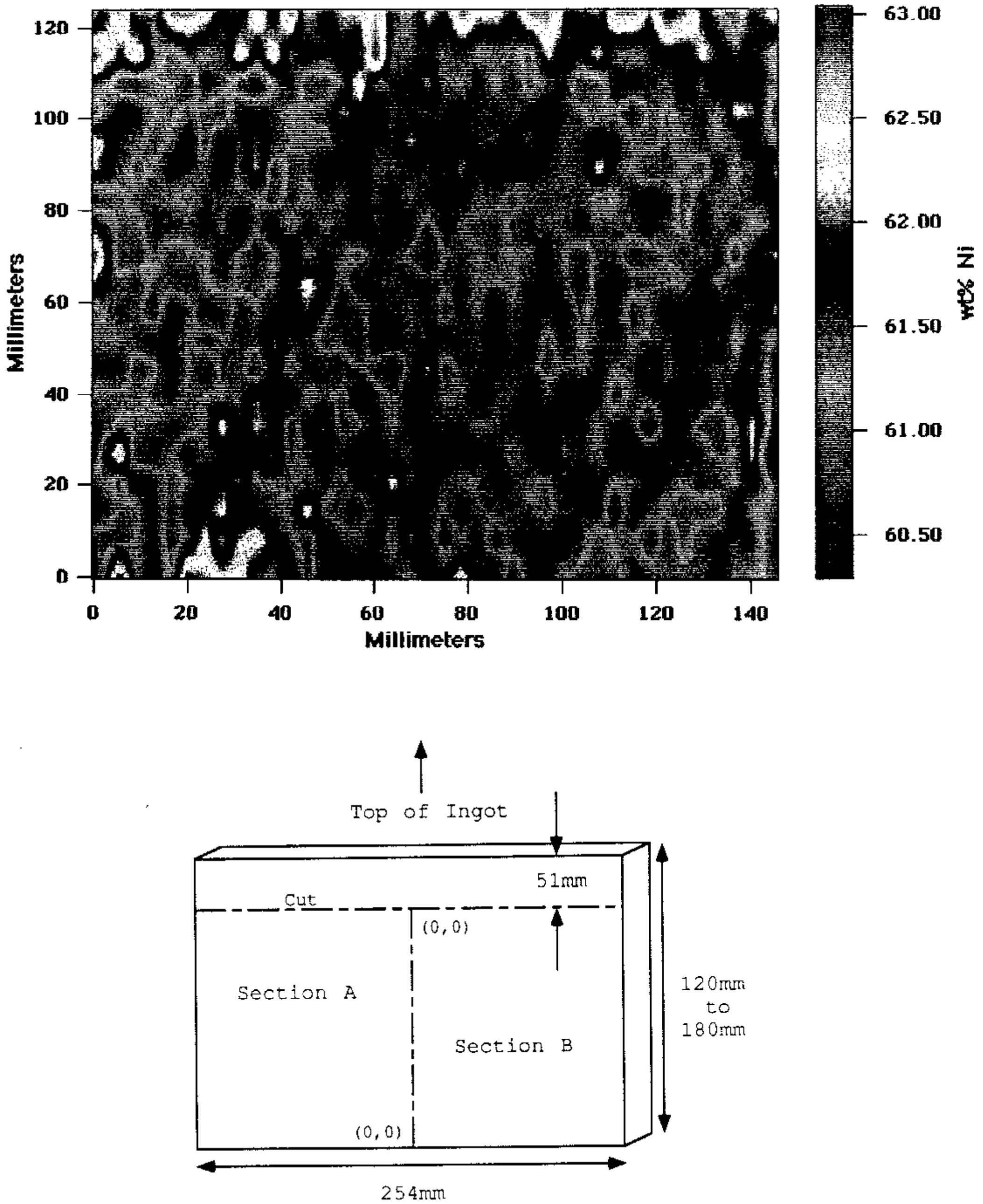

Figure 52. Nickel map from melt section E27-2A.

inside the pool profile relative to the pool profile itself indicated that a significant degree of partitioning occurred in the region of the immersion check. The region of positive niobium segregation at the center of the pool resulted from the partitioning of niobium into the interdendritic liquid and settling during solidification.

Evans and Kruzynski[27] evaluated the centerline segregation tendency of electroslag remelted Alloy 718 at varying melt rates, slag cap thicknesses (between 64 millimeters and 152 millimeters), and varying ingot to billet conversion practice. The center segregation was in the form of banding, either from grain size variation or heavy delta precipitation. They found that segregation was the worst during high melt rate runs with thick slag caps. No mechanisms were presented which explained why variations in melt rate and slag cap thickness affected the degree of segregation.

4.4 SLAG SKIN ANALYSES

The slag skin thickness evaluation produced during electroslag remelting was important for two reasons: 1) it directly affected surface quality and yield, and 2) skin altered heat transfer (i.e. the degree of heat lost to cooling water) by acting as an insulator. Table V (on page

52) lists slag skin thicknesses measured during the steady state trials. These values are plotted as a function of input power in Figures 53-55. In these figures, values are indicated for slag cap thickness, electrode to pool gap distance, and immersion depth respectively. These particular plots revealed no trends which could be used to predict slag skin thickness given a set of parameters.

Figure 56 relates slag skin thickness to power, noting the changes that were also taking place in current. The figure indicates that during both low power and high power melts, the slag skin thickness decreased as the power input was increased.

According to the characterization by Mitchell[34] of the solid slag/molten pool interface, the molten metal can melt back or dissolve the slag skin, resulting in a decrease in the slag skin thickness. Since the molten metal has the ability to melt back the slag skin, it follows that melting parameters which alter the temperature conditions at the top of the molten pool would indirectly affect the thickness of the slag skin.

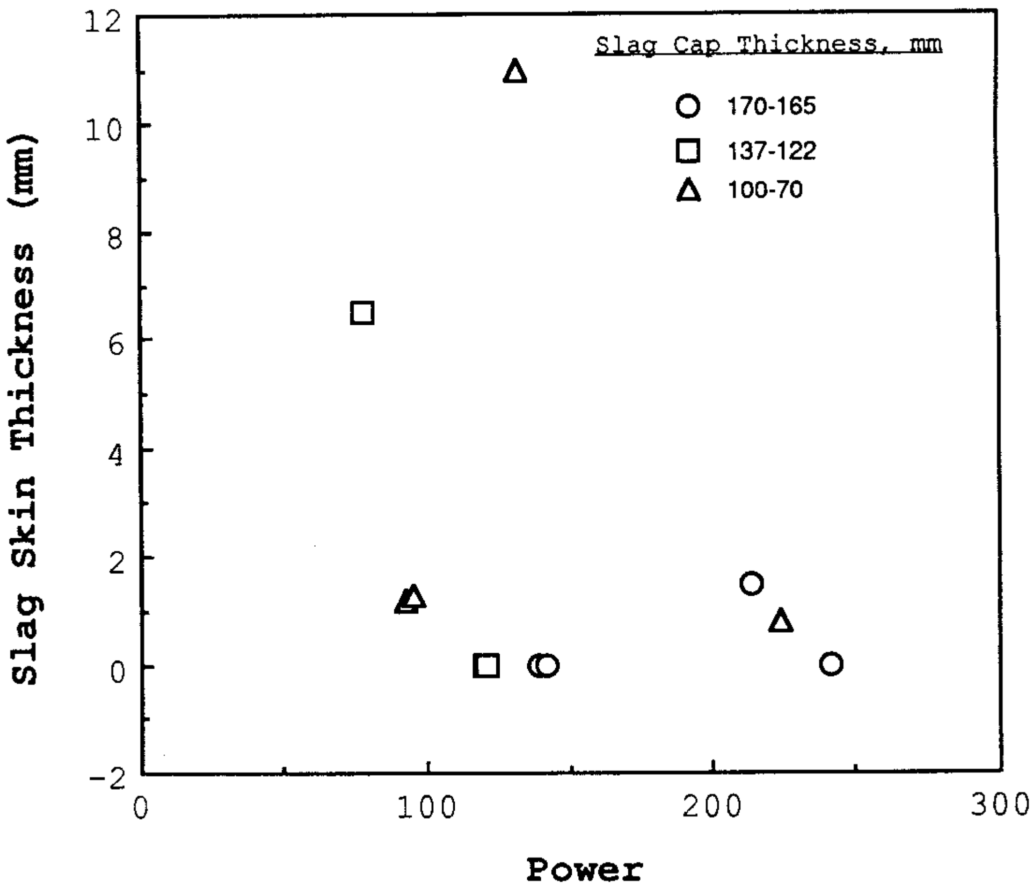

Figure 53. The relation between slag skin thickness and the power input for variations in slag cap thickness.

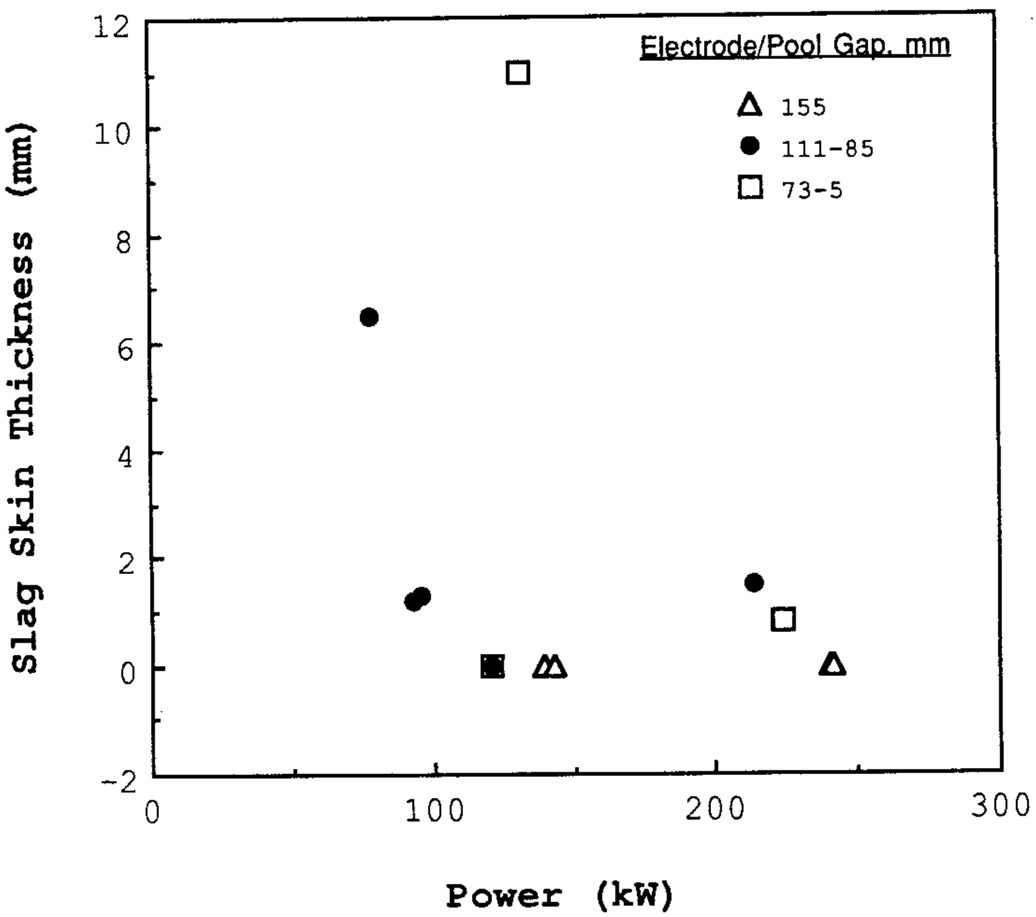

Figure 54. Relation between slag skin thickness and power input for variations in the electrode to pool gap distance.

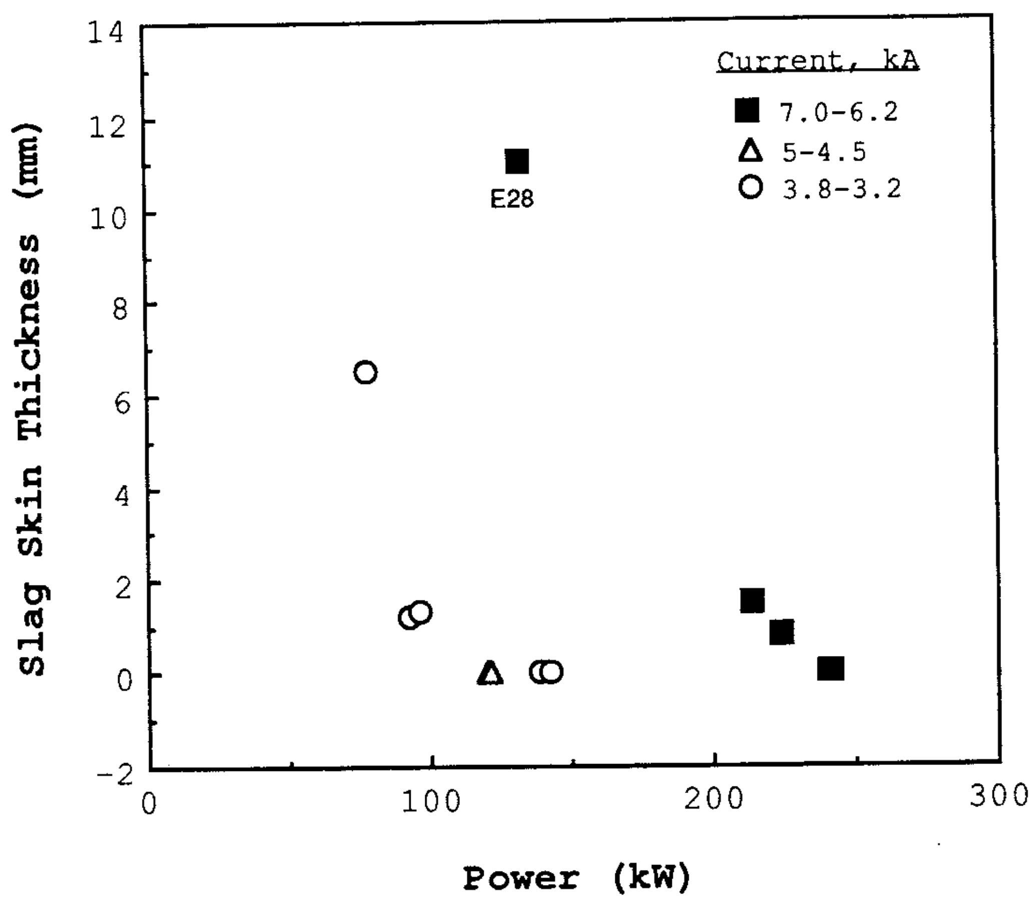

Figure 55. Relation between slag skin thickness and power input for variations in immersion depth.

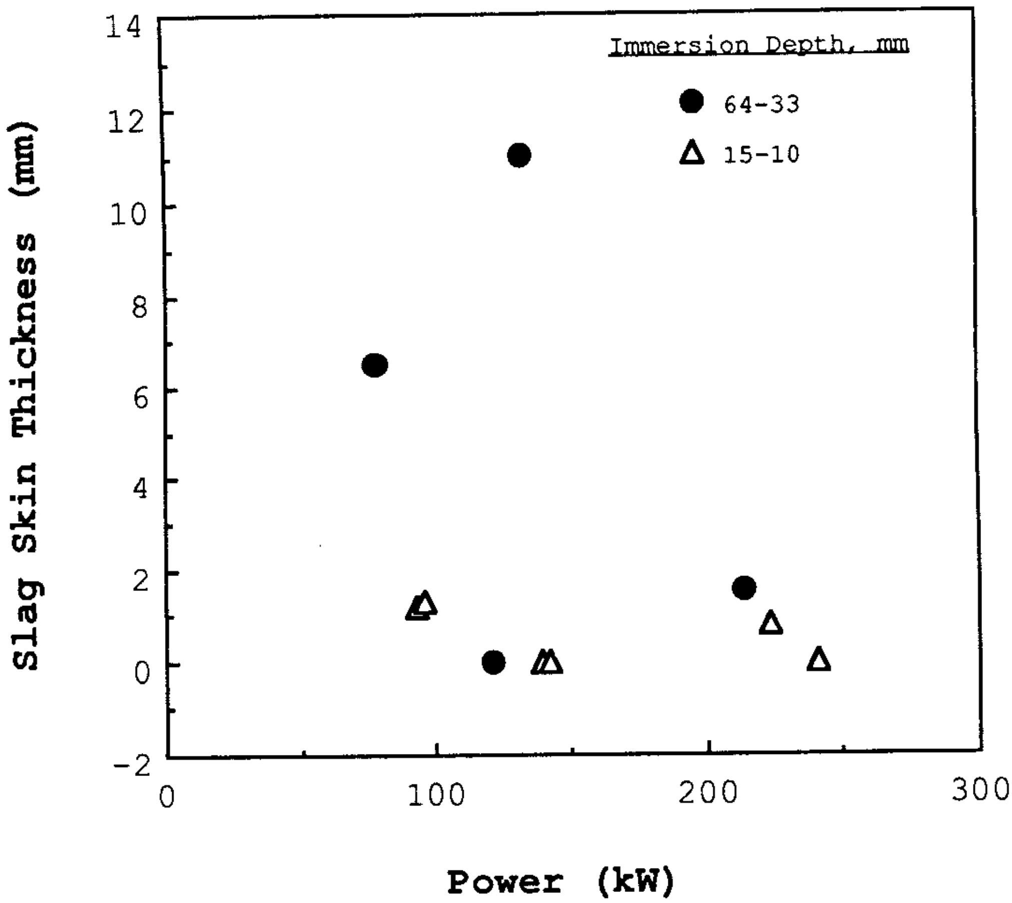

Figure 56. The relation between slag skin thickness and input power for variations in current.

5.0 SUMMARY

The goal of a remelting process such as vacuum arc remelting or electroslag remelting is to produce a compositionally and structurally homogeneous ingot. This can only be achieved through careful control of the parameters which control melting and solidification, based on a thorough understanding of the relationships between these parameters and the solidified structure. In ESR, a large number of melt variables can affect the process and the final ingot structure but the individual and interactive effects of these variables is poorly understood. In industry, the four inputs used to control ESR are: 1) slag composition, 2) melting current (or melt rate), 3) slag cap thickness, and 4) electrode immersion depth (usually controlled by specifying a voltage or voltage swing value). In this investigation, the effects of the last three of these inputs were evaluated.

The investigation was devised to determine the effects of process parameters on several aspects of solidification structure. The aspects of solidification structure included molten pool size and shape, secondary dendrite arm spacing and local solidification time, and the extent of macrosegregation. Tto supplement the solidification structure analysis, the effects of input parameters on slag skin thickness data was also investigated. The entire analysis was based on data accumulated from nine experimental scale electroslag remelted ingots.

The research determined that combinations of melting parameters can affect ingot solidification to a larger extent than any one individual parameter. For example, the largest pool profile was obtained when the electrode was immersed deeply in a thin slag bath at high current. However, the data shows that large pool volumes were not obtained uniformly or uniquely at high currents.

In terms of process efficiency, the investigation showed that as power was increased, more heat was directed toward melting of the electrode, and process efficiency increased. It was also found that at constant power, changing the melt parameters of slag cap thickness, electrode to pool gap distance, and immersion depth had very little effect on the overall process efficiency. Finally, the efficiency was determined to be affected by the mold-to-stool current partitioning ratio.

Molten pool size and shape are important considerations in a remelting process because of their effect on growth direction and macrosegregation. In this investigation, pool volume and pool depth were determined to increase as the input power to the system increased. The following secondary effects were associated with the pool depth and volume: slag cap thickness, immersion depth, and electrode to pool gap distance. Of these, the electrode to pool gap distance seemed to be most directly related to pool size. The relative position of the slag's high heat generation region with respect to the molten pool combined with the system's ability to extract heat across the slag/mold and ingot/mold interface, were the primary factors which governed heat flow and the shape and size of the pool. The thickness of the slag skin also had a significant effect on distribution of heat and the resulting pool profiles. The concluded effects of the process parameters on the pool volume can be verified quantitatively by comparing the average pool volume at each process parameter level. Which means, the average pool volume for all the high current melts would be compared with the average pool volume for all the low current melts and so on. The average pool volume for each parameter level is presented in Figure 57. The average volume data, each representing a specific parameter level, indicates that increases in current, increases immersion depth, and decreases in slag cap thickness causes pool volume to increase.

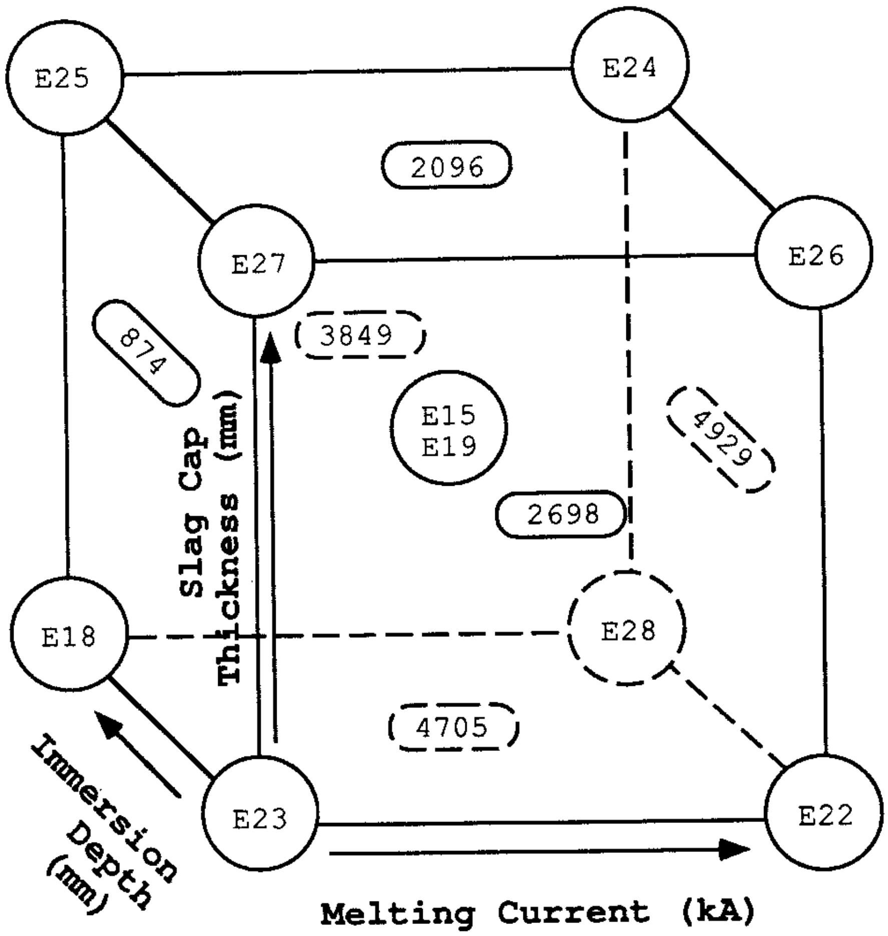

Figure 57. The schematic of the factorially designed experiment, presenting an average volume for each parameter level.

Examination of the molten pool shape, represented by a depth to volume ratio, showed that the experimental melts more closely approximated a conical pool shape rather than a cylindrical one. In addition, the analysis shows very little shape change occurred over the range of experimental melts.

The local solidification time is a function of the thermal gradient and the rate of advance of the solidification front. In this investigation, local solidification time was observed to be a complex parameter, and a clear correlation between the melt parameters studied and either local solidification time or solidification front advance rate were not found. The experimental data did agree with general trends reported in the literature, for example a decrease in local solidification time was seen when one moved from the centerline of the ingot to the edge.

Compositional mapping of the deep pool profiles showed niobium residing at the center of the pool. Nickel also exhibited a tendency to segregate, high nickel was observed along the outline of the pool profile while the area at the center of the pool was lean in nickel.

This research addressed the importance of each parameter individually and in combination. When melting segregation prone alloys, pool profile needs to be minimized to restrict the movement of solute or particles and reduce the materials ability to segregate. Minimization of pool profile means inefficient melting at low power. During ESR processing, optimum melting with respect to cost and efficiency occurs during high power melts but at a cost of decreasing the metallurgical integrity of the ingot. This research can be used a stepping stone in order to obtain a better understanding and better control of the electroslag remelting process.

6.0 CONCLUSIONS

1. Melting efficiency increased as input power increased. This relation was found to be independent of slag cap thickness, immersion depth, electrode to pool gap, or melting current.
2. Increasing slag cap thickness or electrode to pool gap were found to decrease pool depth and volume.
3. The gap distance between the electrode and pool was found to be the most closely related to pool depth and pool volume, suggesting that it can control the process.
4. No correlation was found between local solidification time and input power, pool depth, slag cap thickness, or immersion depth.
5. The observed macrosegregation tendencies in the deep pool profile lended support to density driven flow as a segregation mechanism.

REFERENCES CITED

1. Hoyle, G. and Duckworth, W.E. 1969. Electroslag Refining. London: Chapman and Hall LTD: 9-15.

2. Hoyle and Duckworth, 31-53.

3. Box, G.E. and Draper, N.R. 1987. Empirical Model-Building and Response Surfaces. New York: John Wiley and Sons: 105-109.

4. ASM. 1980. Metals Handbook 9th Edition (December) 3: 143.

5. Sim, C.T. and Hagel, W.C. 1972. The Superalloys. New York : John Wiley and Sons: 115-117.

6. Quist, W.E. and Taggert, R. 1971. Metall. Trans. 2: 825-832.

7. Cieslak, M.J.; Headley, T.J.; Kollie, T.; and Romig, A.D. 1988. Metall. Trans. A (September) 19A: 2319-2331.

8. Loria, E.A. 1991. Proceedings of the International Symposium on Metallurgy and Applications of 718 and 625. Pennsylvania: Minerals, Metals, and Materials Society: 363-374.

9. Wlodek, S.T. 1963. Trans. Amer. Soc. Met. 56: 287-303.

10. Medovar, B.I.; Latash, Y. V.; Maksimovich, B.I.; and Stupak, L.M. 1963. Electroslag Remelting. Moscow: State Scientific and Technical Publishing House of Literature: 18-25.

11. Ballantyne, A.S.; Mitchell, A. 1977. Iron and Steel Making 4: 222-239.

12. Carvajal, L.F. and Geiger, G.E. 1971. Metall. Trans (August) 2: 2087-2092.

13. Paton, B.E.; et.al. 1973. Conference on Electroslag Remelting. London: Metals Society: 16-20.

14. Mellberg, P.O. and Sandberg, H. 1973. Scandinavian Journal of Metallurgy 2: 83-86.

15. Holzgruber, W. 1974. Proceedings of the 5th International Conference on ESR. Pittsburgh: Mellon Institute

16. Kroneis, M. 1968. Berg. Hutten. Monat. 113: 416.

17. Eckstein, H.J. 1968. Berg, Hutten. Monat. 113: 424.

18. Ballantyne, A.S.; Kennedy, R.J.; and Mitchell, A. 1976. Proceedings of the 5th International Conference on Vacuum Metallurgy. Munich: (Press?): 181-186.

19. Ballantyne, A.S. and Mitchell. A. 1977. Proceedings of the International Conference on Solidification and Casting of Metals. Sheffield: Metals Society: 363-370.

20. Barkalow, R.H. 1972. Metall. Trans. 3: 919.

21. Ballantyne, A.S.; Mitchell, A.; and Wadier, J.F. 1979. Proceedings of the 6th International Vacuum Metallurgy Conference. Sna Diego: American Vacuum Society: 599-623.

22. Shved, F.I. 1964. Steel USSR 4: 636.

23. Howarth, J.A. and Mondolfo, L.F. 1962. ACTA Metallurgica (November) 10: 1037-1042.

24. Bower, F.; Brody H.D.; and Flemings, M.C. 1966. AIME Metall. Trans. (May) 236: 624-624.

25. Bhambri, A.K.; Kattamis T.Z.; and Morral, J.E. 1975. Metall. Trans. B. (December) 6B: 523-537.

26. Alexander, B.H. and Rhines, F.N. 1950. Journal of Metals (October) 188: 1267-1273.

27. Flemings, M.C. 1976. Scand. Journal of Metall. 5: 1-15.

28. Evans, M.D. and Kruzynski, G.E. unpublished research. Cytemp Specialty Steel Division.

29. Kou, S.; Pourier, D.; and Flemings, M.C. 1978. Metall. Trans. B (December) 9B: 711-719.

30. Kay, D.A.R. and Pomfret, R.J. 1971. J. Iron and Steel Inst. (December): 962-965.

31. Mitchell, A. 1974. Iron Making and Steel Making 3: 172-179.

32. Mitchell, A.; Jackson, R.O.; and Ballantyne, A.S. 1973. Proc. 4th Intl. Conf. ESR. Tokyo: ISIJ: 1-12.

33. Hoyle and Duckworth, 128-129.

34. Mitchell, A. and Etienne, M. 1968. TMS AIME (July) 242: 1462-1464.

35. Bell, M. and Mitchell, A. 1971. J. Iron Steel Inst. 209: 658-660.

36. Underwood, E.E. and Berry, J.T. 1981. AFS Transactions 89: 755-766.

37. Mitchell, A. and Joshi, S. 1973. Metallurgical Transactions (March) 4: 631-642.

38. Ballantyne, A.S. Haynes International, Private Communication, 1991.